

Photoassociation of Cold Metastable Helium Atoms

Geraldine Woestenenk

Woestenenk, Geraldine

Photoassociation of Cold Metastable Helium Atoms

G.R. Woestenenk - Utrecht

Universiteit Utrecht

Faculteit Natuur- en Sterrenkunde

Thesis Universiteit Utrecht - With a summary in Dutch

ISBN 90-393-2725-4

Subject heading: atomic physics / laser cooling / photoassociation

Ontwerp omslag: Sonia Woestenenk

Druk: FEBO druk, Enschede

Photoassociation of Cold Metastable Helium Atoms

Foto-associatie van Koude
Metastabiele Helium Atomen

(met een samenvatting in het Nederlands)

PROEFSCHRIFT

TER VERKRIJGING VAN DE GRAAD VAN DOCTOR
AAN DE UNIVERSITEIT UTRECHT OP GEZAG VAN
DE RECTOR MAGNIFICUS, PROF. DR. W.H. GISPEN,
INGEVOLGE HET BESLUIT VAN HET COLLEGE VOOR PROMOTIES
IN HET OPENBAAR TE VERDEDIGEN
OP MAANDAG 18 JUNI 2001
DES MIDDAGS TE 14.30 UUR

door

Geraldine Raluca Woestenenk

geboren op 13 juli 1973, te Amsterdam

Promotoren: Prof. Dr. A. Niehaus
Prof. Dr. P. van der Straten

Faculteit Natuur- en Sterrenkunde
Universiteit Utrecht

This work has been performed as part of the research program of the ‘Stichting voor Fundamenteel Onderzoek der Materie’ (FOM) and with the financial support from the ‘Nederlandse Organisatie voor Wetenschappelijk Onderzoek’ (NWO).

Contents

1	Introduction	5
1.1	General introduction	5
1.2	Contents of this thesis	6
2	Experimental Setup	11
2.1	Introduction	11
2.2	Laser cooling and trapping	12
2.2.1	Zeeman slowing	13
2.2.2	Magneto-optical trap	14
2.3	Experimental setup	16
2.4	Metastable helium source	18
2.4.1	Construction	18
2.4.2	Results	20
2.4.3	Loading the MOT	22
2.4.4	Hexapole magnetic lens	26
2.4.5	Conclusions	30
2.5	Characteristics of the MOT	31
2.5.1	MOT temperature	32
2.5.2	Spatial distribution	33
2.6	Conclusions	36
3	Long-Range States of He₂[*]	39
3.1	Introduction	39
3.2	Angular momenta	39
3.2.1	Hund's case (a)	40
3.2.2	Hund's case (c)	41
3.2.3	Symmetry rules	42

Contents

3.3	Molecular wavefunctions	43
3.3.1	Spin states	44
3.3.2	He $2^3S_1 - 2^3S_1$ molecular wavefunctions	44
3.3.3	He $2^3S_1 - 2^3P_{0,1,2}$ molecular wavefunctions	45
3.4	Calculation of long-range potentials	45
3.5	The behavior of the long-range potentials	49
3.5.1	Purely long-range potentials	51
3.5.2	Lifetimes of the molecular states	52
3.6	Partial waves	55
3.7	Penning Ionization	56
4	Photoassociation Spectroscopy of He*	59
4.1	Introduction	59
4.2	Experiments	61
4.3	Results	63
4.4	Analysis	67
4.4.1	Leroy-Bernstein fit	69
4.4.2	Effective C_3 coefficient	71
4.4.3	Accumulated phase analysis	72
4.4.4	Ionization Mechanism	74
4.5	Conclusions	76
5	Effects near the $2^3S_1 - 2^3P_1$ Asymptote	79
5.1	Introduction	79
5.2	Experiments	81
5.3	PAS near the $2^3S_1 - 2^3P_1$ asymptote	83
5.3.1	Results	83
5.3.2	Analysis	85
5.4	Purely long-range states	86
5.4.1	Results	87
5.4.2	Analysis	88
5.5	Shape resonances	93
5.5.1	Results	93
5.5.2	Analysis	94
5.6	Conclusions	96

6 Penning Ionization in Optical Collisions	99
6.1 Introduction	99
6.2 Experimental	101
6.3 The two state model	103
6.4 Calculation of the absolute ionization rate constant	108
6.5 Comparison of calculated and measured absolute ionization rate constants	110
6.6 Conclusion	114
Samenvatting	115
Curriculum Vitae	119
Publications	121
Dankwoord	123

Chapter 1

Introduction

1.1 General introduction

During the last decade the study of cold atoms has grown in a great measure. Research in this field has been made accessible due to the development of laser cooling and trapping techniques [1], making it possible to cool atoms to ultra-low temperatures and to trap samples of cold atoms in small volumes. Laser cooling is now widely used and in many laboratories around the world the work horse of the field, the magneto-optical trap (MOT), has been built. The alkali-metals are the elements of the periodic table that have been used most in laser cooling experiments. Furthermore, amongst others metastable rare gas atoms have proven to be suitable candidates to be cooled and trapped too. In principle all atoms can be laser cooled, but in practice the suitability depends on the wavelength of the cooling transition, on the lifetime of the excited state, and on whether spontaneous emission from the excited state is primarily to the ground state of the cooling transition.

With cold atoms phenomena can be studied that are not accessible with thermal atoms and as a consequence many interesting experiments have been done since the development of laser cooling. Due to the small kinetic energy spread of the atoms, high precision experiments can be done, such as high resolution spectroscopy of photoassociated atoms [2] and studies of cold collisions [3]. Furthermore, laser cooled atoms are the first step towards Bose-Einstein condensation (BEC) [4]. The study of cold collisions provides information that is important for BEC, such as the scattering length of a system or the elastic and inelastic cross sections.

An important method to study cold atoms is photoassociation spectroscopy (PAS), where atoms colliding in the ground state are excited to a bound state. For a detailed description of PAS the reader is referred to Sec. 4.1. Below, the principle of PAS is only roughly outlined. PAS allows us to study the excited state potential at internuclear distances large compared to traditional molecular spectroscopy. At these large distances the ground state wavefunction oscillates very slowly, since the kinetic energy of the colliding atoms is very small. Therefore the overlap between the free ground state and the bound excited state is largest at the outer turning point of the bound state. This means that the excitation is made at the outer turning point of the bound state. The resolution of the measurements is very good, due to the low kinetic energy spread of the colliding atoms. Thus we have a powerful and precise method to study interactions between cold atoms.

PAS has been very successful in the study of alkali-metals. In Ref. 3 various examples of studies of alkali-metals are given, in which for example the ground state scattering length is determined for lithium, sodium, and rubidium.

1.2 Contents of this thesis

In this thesis photoassociation of cold metastable helium atoms is discussed. Compared with the alkali-metals little is known about the metastable helium system. In this thesis we have made an exploratory study of cold colliding metastable helium atoms in the presence of light.

The metastable helium atom is in the (2^3S_1) state and will be denoted as the He* atom. The lifetime of this metastable state is very long, more than 7000 s. The part of the level diagram for the He atom that is relevant for the experiment is shown in Fig. 1.1. As can be seen in the figure the internal energy of the metastable state is very high (19.8 eV). Due to this high internal energy colliding He* atoms can ionize at small internuclear distances, of the order of a few a_0 .

The experiments described in this chapter have been performed with cold trapped He* atoms. The atoms are laser cooled and trapped in a MOT. In Chap. 2 we shortly discuss the principle of laser cooling and trapping. The He* atoms are produced in a DC-discharge source. We have constructed a novel type of source, which is cooled with liquid helium. The average velocity of the produced He* atoms is 300 m/s, which is considerably lower than the velocity of atoms produced conventional sources (800 - 2000 m/s). The construction of the source and the characteristics of the produced beam of He* atoms are discussed in Chap. 2. The experimental setup that is used to cool and trap a cloud of He* atoms, is de-

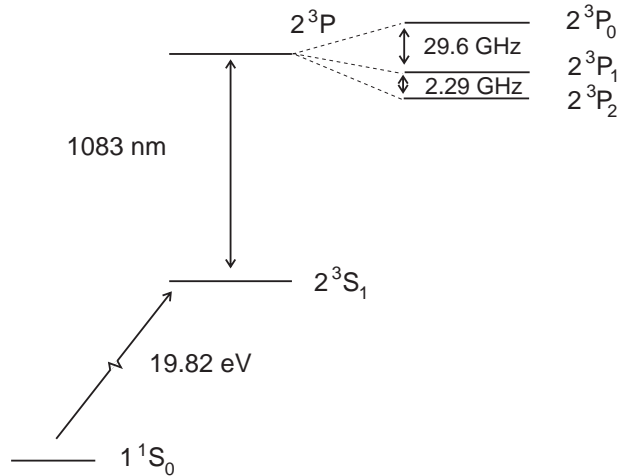


Figure 1.1 Level diagram for He.

scribed and the characteristics of the cloud of cold trapped atoms are determined. Typically we trap 10^6 He* atoms, with a temperature of about 1 mK and a density of a few times $10^9/\text{cm}^3$.

For the analysis of the measurements it is important to have a good description of the interaction potential for the colliding atoms. We have applied methods used to calculate long-range potentials for alkali-metal systems [5] to calculate the potentials for the He* - He* system. In Chap. 3 we discuss how these potentials have been calculated. They have been used in the analysis done in the rest of the thesis. The potentials have been calculated in an internuclear distance range from a few times $10 a_0$ to $1000 a_0$. At short range the electronic motion is strongly coupled to the internuclear axis, while at long range the spin-orbit coupling is stronger than the coupling to the internuclear axis. In the intermediate region connecting short range and long range the molecular states are mixed due to the fine-structure interaction. As a result of the mixing the molecular lifetime and the effective C_3 coefficient (C_3^{eff}) vary with the internuclear distance, where C_3^{eff} is defined by $C_3^{eff} = V(R)R^3$. As is the case for alkali-metals, in the He*₂ system there exist purely long-range potentials, which result from avoided crossings between potentials with identical symmetries. They are attractive at very long range and become repulsive at internuclear distances of $\sim 100a_0$. The study of purely long-range

potentials has yielded much information in PAS of alkali-metals [2, 3].

In Chap. 4 we study excitation of the molecular system close to the $2^3S_1 - 2^3P_2$ asymptote. These are the first PAS measurements for the He* system. Part of these measurements have also been presented in Ref. 6. We have observed peaks in the ionization rate, which can be attributed to the excitation of bound states in the excited state of the molecule. The peak positions are analyzed using the potentials calculated in Chap. 3 and three series of vibrational states are identified in the spectra. It is not clear why ion peaks are observed when a bound state is excited. As is discussed in Sec. 4.4.4, one would naively expect to observe a decrease in the ionization rate when a bound state is excited. We have found a mechanism that is responsible for the increase in ionization when a bound state is excited and give a qualitative description of this mechanism in Chap. 4.

In Chap. 5 we study excitation of the molecular system close to the $2^3S_1 - 2^3P_1$ asymptote. As can be seen in Fig. 1.1 this asymptote lies only 2.29 GHz above the $2^3S_1 - 2^3P_2$ asymptote. There are a number of differences in the potentials compared the potentials connected to the $2^3S_1 - 2^3P_2$ asymptote. The couplings between the potentials are stronger and there are purely long-range potentials. We have studied loosely bound vibrational states at detunings around the atomic resonance. We observe a decrease in the ionization rate at a small negative detuning and an increase in the ionization rate at small positive detunings. The dip is attributed to the excitation of a bound state in a purely long-range potential. A peak at a positive detuning cannot result from the excitation of a bound state in an attractive potential, since such a state would have to be lying in the continuum of the potential. We tentatively attribute the increase in ionization rate to the excitation of a shape resonance.

In Chap. 6 we study optical collisions, *i.e.* collisions in the presence of nearly-resonant light. With the optical collisions we study the dynamics of the collisions and the ionization rate constants. The collisions of the He* atoms in the MOT are manipulated by light and the manipulation is monitored by the ionization rate. We have constructed a semi-classical model to calculate the ionization rate constant, where we calculate both the shape of the ionization rate constant as a function of the frequency of the light and the absolute ionization rate constant. The shape of the ionization rate is compared with measurements. Furthermore, the calculated absolute rate constant is compared with values that have appeared in the literature. We find good agreement between the calculated and the experimentally determined ionization rate constant.

In conclusion, we have studied colliding cold He* atoms in the presence of

(nearly-resonant) light. We have investigated various aspects of the system, varying from the excitation of molecular states to the dynamics of colliding atoms. It is clear that many new things can be learned about the cold He* - He* system. The experiments and analysis given in this thesis are just a start . . .

References

- [1] H.J. Metcalf and P. van der Straten, *Laser Cooling and Trapping*, Springer-Verlag, New York (1999).
- [2] P. D. Lett, P.S. Julienne, and W.D. Phillips, *Ann. Rev. Phys. Chem.* **46**, 423 (1995).
- [3] J. Weiner, V.S. Bagnato, S. Zilio, and P.S. Julienne, *Rev. Mod. Phys.* **71**, 1 (1999).
- [4] M.H. Anderson, J.R. Ensher, M.R. Matthews, C.E. Wieman, and E.A. Cornell, *Science* **269**, 198 (1995).
- [5] M. Movre and G. Pichler, *J. Phys. B.* **10**, 2631 (1977).
- [6] N. Herschbach, P.J.J. Tol, W. Vassen, W. Hogervorst, G. Woestenenk, J.W. Thomsen, P. van der Straten, and A. Niehaus, *Phys. Rev. Lett.* **84**, 1874 (2000).

Chapter 2

Experimental Setup

2.1 Introduction

The experiments described in this thesis have been carried out using cold, trapped metastable He atoms. The metastable atoms are in the 2^3S_1 state and will be denoted from now on as He* atoms. A sample of cold atoms is produced by laser cooling and trapping the atoms. In 1975 the idea to cool atoms with nearly resonant laser light was proposed by Hänsch and Schawlow [1] and by Wineland and Dehmelt [2]. Since then various techniques have been developed to cool and trap neutral atoms with laser light and laser cooling and trapping has become widely established. Laser cooling and trapping has made a new area available for studies, namely the interactions between ultra-cold atoms, and in many laboratories around the world experiments are carried out using laser cooled atoms. Examples of these experiments are studies of collisions between ultra-cold atoms [3,4], Bose-Einstein condensation [5] and high precision spectroscopy experiments [6]. One of the main tools in the experiments is the magneto-optical trap (MOT). Among the elements of the periodic table that are studied, the metastable rare gases play an important role [4, 7, 8].

In this chapter we will describe the experimental setup in which we cool and trap He* atoms. In Sec. 2.2 the basic principles of laser cooling and trapping will be described. The experimental setup will be discussed in Sec. 2.3. Special emphasis is put on the production of a slow and intense He* beam in Sec. 2.4, since the design of the source that produces the beam is new. The He* beam is used to load a MOT. The properties of the atoms in the MOT are discussed in Sec. 2.5.

2.2 Laser cooling and trapping

Using nearly resonant light, a force can be exerted on atoms. If we consider a two level atom, with one ground and one excited state, the atom can be excited from the ground to the excited state by absorption of resonant laser light. When the atom absorbs a photon, momentum from the laser beam is transferred to the atom in the propagation direction of the light. Since the excited state has a finite lifetime, the atom spontaneously decays back to the ground state while emitting a photon in a random direction. In this process recoil momentum is transferred to the atom in a random direction. After a large number of excitation and spontaneous emission cycles this random recoil momentum averages out to zero and a net force is exerted on the atoms in the propagation direction of the laser beam. This is called radiation pressure.

A slowly moving atom that is irradiated by two laser beams, having identical frequency and polarization but opposite propagation directions, can experience a damping force if the laser light is tuned below the atomic resonance [9]. This is illustrated in Fig. 2.1 where the force is shown as a function of the velocity of the

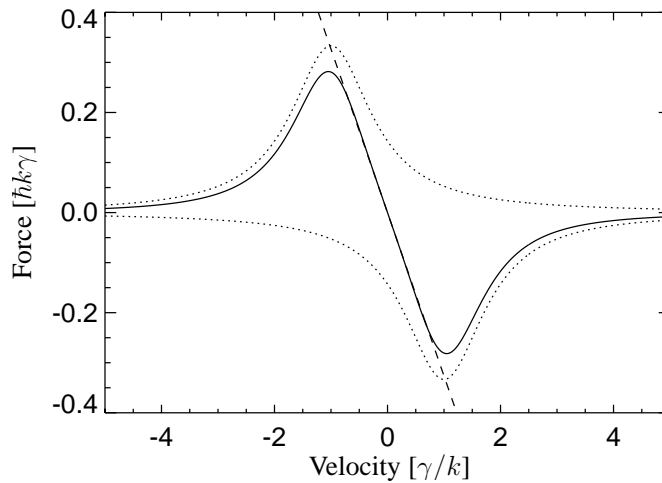


Figure 2.1 Damping force for slow atoms as a function of the velocity of the atoms. The velocity is expressed in γ/k , where γ is the natural linewidth of the excited state and k is the wave number of the light. The force is expressed in $\hbar k \gamma$.

atoms. For small velocities the force can be approximated by $F = -\beta v$, where v is the velocity of the atoms and the damping coefficient β is given by

$$\beta = -\hbar k^2 \frac{8s_0(\Delta/\Gamma)}{(1 + (2\Delta/\Gamma)^2)^2}, \quad (2.1)$$

where k is the wave number of the light, s_0 the saturation parameter, Δ the detuning of the laser light from atomic resonance and Γ the natural linewidth of the excited state. If the atoms have a velocity $v \neq 0$, they will see the light of both laser beams with a Doppler-shift. The atoms will interact strongest with light that is Doppler-shifted towards resonance. If the light is tuned below resonance the atoms will absorb more photons from the beam that travels opposite to the direction of the motion of the atoms and thus their velocity is reduced. The viscous damping force on an ensemble of atoms is called optical molasses. The effect was demonstrated experimentally for the first time by Chu *et al.* [10].

2.2.1 Zeeman slowing

The initial velocity of metastable helium atoms is relatively high, compared to *e.g.* alkali atoms. Unlike in experiments with alkali atoms, not the ground state of the atom is used, but a metastable excited state with a very long lifetime. The metastable state is produced in a discharge, usually in a DC-discharge source. If the source is not cooled, the mean velocity of a beam of He* atoms emerging from the source is 2000 m/s [11]. Even if it is cooled with liquid nitrogen the mean velocity is still 900 m/s [12]. Since the capture velocity of a standard He* MOT lies around 60 m/s, a beam used to load the MOT needs to be pre-cooled, which is mostly done in a Zeeman slower, before the atoms can be trapped.

A beam of neutral atoms can be slowed by irradiating it with a counter-propagating laser. The radiation pressure changes the velocity of the atoms and thereby changes the Doppler shift with which the atoms see the laser light. Since the Doppler shift is usually much larger than the power broadened linewidth, the atoms are shifted out of resonance with the laser light. The Zeeman-compensation technique [13] compensates for the Doppler shift by applying an inhomogeneous magnetic field. In the magnetic field the ground and the excited states are shifted due to the Zeeman effect. The magnetic field of the Zeeman slower is constructed in such a way that over the whole slowing path the Zeeman shift induced by the varying magnetic field compensates the varying Doppler shift. In this way the atoms in the beam can be cooled, *i.e.* they are slowed down to low velocities,

in our case to the capture velocity of a MOT, and the velocity distribution is narrowed. As will be described in Sec. 2.4.3 there are certain difficulties connected to the use of the Zeeman slowing technique and the experiment can be greatly simplified if atoms can be loaded into a MOT without being pre-cooled in a Zeeman slower.

2.2.2 Magneto-optical trap

Many experiments require a dense sample of cold atoms. Therefore it is not just enough to cool the atoms, they also need to be spatially confined. The damping force shown in Fig. 2.1 only cools the atoms. In a magneto-optical trap (MOT) the atoms are both cooled and trapped in three dimensions. The construction of a MOT was first demonstrated in 1987 by Raab *et al.* [14]. A three-dimensional schematic picture of a MOT is shown in Fig. 2.2b. Six counter-propagating laser beams in three mutually orthogonal directions overlap in the center and produce a damping force. The confining force is generated by the combination of an inhomogeneous magnetic field and the laser light. The magnetic field is produced

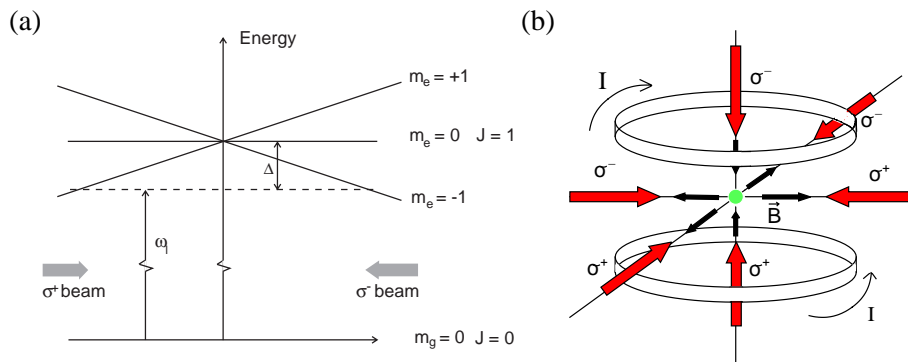


Figure 2.2 Part (a) shows a one dimensional representation of the MOT, where m_g indicates the ground state and m_e the excited state magnetic substates. ω_l is the laser frequency and Δ is the detuning with respect to the atomic resonance. Part (b) is a three dimensional representation of the MOT. The coils that generate the magnetic field are shown and the direction of the current. Furthermore the laser beams, coming from six directions with circular polarizations σ^+ and σ^- are indicated.

by two coils in an anti-Helmholtz configuration. It is zero in the center of the trap and linearly increasing with the distance from the center for small distances from the center.

In Fig. 2.2a the principle of the MOT is shown in one dimension when a $J = 0 \rightarrow J = 1$ transition is used. The inhomogeneous magnetic field splits the magnetic substates of the states of the atom. In the one-dimensional example shown in Fig. 2.2a the ground state has an angular momentum of $J = 0$, so only the substates of the excited state are split. Two counter-propagating laser beams have opposite circular polarizations, σ^+ and σ^- . For a negative detuning Δ of the laser, the excited state with $m_e = +1$ is shifted away from the laser frequency for positive B-field, while the state with $m_e = -1$ is shifted towards the frequency. Therefore at positive magnetic field the atoms scatter more light from the σ^- beam than from the σ^+ beam and the atoms are driven towards the center of the trap, where the magnetic field is zero. In addition the atoms are cooled by the velocity damping force shown in Fig. 2.1 as the laser light is tuned below the atomic resonance.

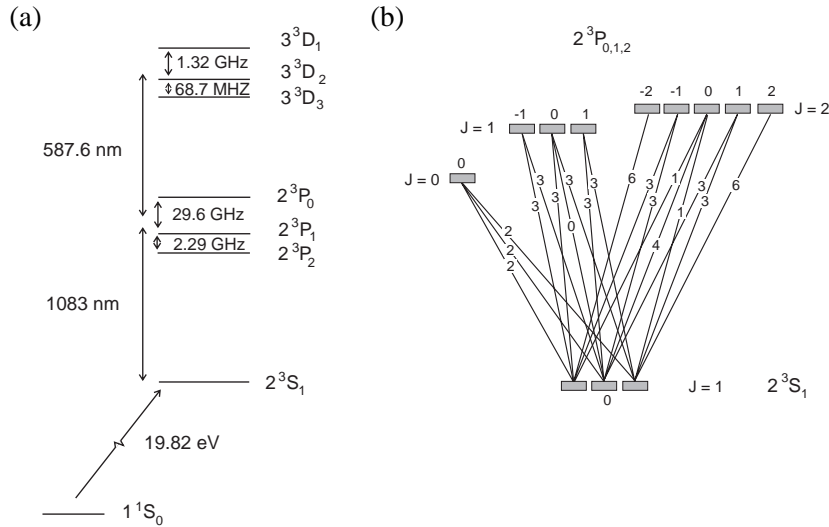


Figure 2.3 Part (a) shows the level scheme of He. In part (b) the transition strengths for the possible optical transitions are shown for the $2^3S_1 \rightarrow 2^3P$ transition. The weakest allowed transition is chosen to be 1.

In the case of He* the $2^3S_1 \rightarrow 2^3P_2$ transition is used as a cooling transition. In Fig. 2.3a the level scheme of helium is shown in the range that is relevant for the experiments discussed in this thesis. The $2^3S_1 \rightarrow 2^3P_2$ transition has a wavelength of 1083 nm. The lowest metastable state (the He (2^3S_1) state) has an angular momentum of $J = 1$ while the atom in the picture of the 1D MOT has an angular momentum of $J = 0$ in the ground state. As a consequence we do not have a two level system but a multilevel system. Since it is a closed system, laser cooling is possible. The transition strengths of the various lines are shown in Fig. 2.3b.

2.3 Experimental setup

A schematic picture of the experimental setup is shown in Fig. 2.4. The setup consists of several parts. First, a slow He* beam is produced in a DC-discharge source. The construction of this source and the properties of the beam will be described in Sec. 2.4. Subsequently, the atoms are slowed down and trapped in a MOT. The characteristics of the cloud of trapped atoms will be described in Sec. 2.5.

The setup is a UHV setup which is differentially pumped. In this way the pressure in the MOT chamber is minimized and losses of atoms from the trap which

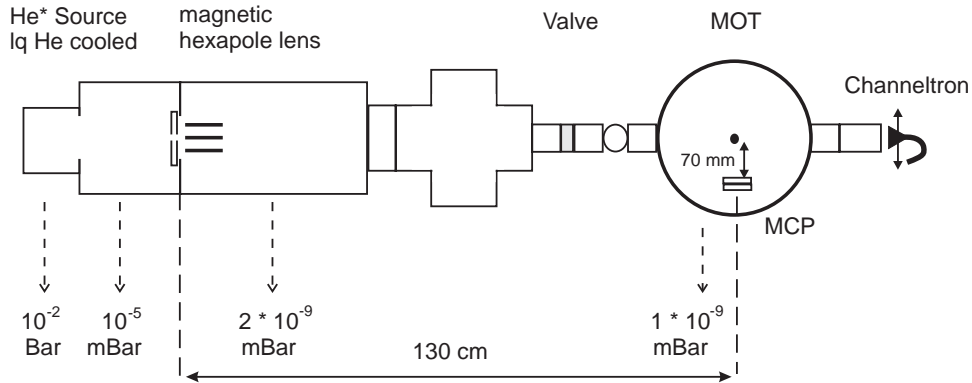


Figure 2.4 Schematic picture of the setup with typical pressures during operation indicated at the bottom. MCP stands for micro-channel plates.

are induced by collisions with background atoms are reduced. The pressures are indicated in Fig. 2.4. The apparatus is pumped by magnetically suspended turbo molecular pumps (Balzers, types TCM 180 and TCM 520).

In the experiment two types of lasers are used. The $2^3S_1 \rightarrow 2^3P_2$ transition is the transition that is used to cool and trap the atoms. The corresponding wavelength is 1083 nm. The light is generated by diode lasers (Spectra Diode Lab, SDL-6702-H1). The current through the diode and the temperature of the diode are controlled by home made units and by a commercial unit (TUI, DC 100). The laser beam is collimated with an anti-reflection coated lens to a beam of 8×2 mm. The output power of the lasers is around 40 mW. The laser light is linearly polarized and the laser linewidth is 3 MHz.

Furthermore, a single mode CW ring dye laser is used to pump the $2^3P \rightarrow 3^3D$ transition, which has a wavelength of 587.6 nm. This transition is used to image the cloud of trapped atoms with visible light. The laser produces around 600 mW linearly polarized light and it is pumped with a 7 Watt argon ion laser. The light is coupled into a single mode polarization preserving optical fiber with a length of 100 m. The fiber is saturated at 20 mW and this intensity is coupled out.

The trapping laser is locked on the atomic $2^3S_1 \rightarrow 2^3P_2$ transition. To be able to lock the laser on the atoms that have zero velocity, saturated absorption

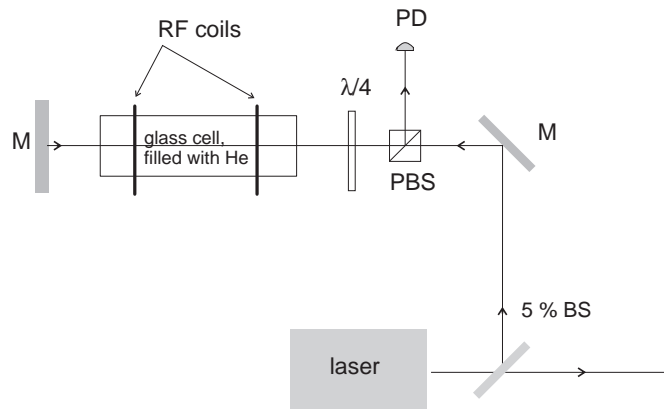


Figure 2.5 The saturation spectroscopy setup. BS stands for beam splitter, M for mirror, PBS for polarizing beam splitter, $\lambda/4$ for quarter wave retardation plate, and PD for photo diode.

spectroscopy is used, in a pump-probe setup. A laser beam is sent through a sample of He* atoms and retro-reflected. The incoming laser beam is used as a pump beam, while the retro-reflected beam is used as a probe beam. The power of the probe beam is smaller than the power of the pump beam since light of the pump beam is absorbed. In this way the laser can be locked on the Lamb-dip, *i.e.* on the atoms which have zero velocity, and the line is not Doppler-broadened. The linewidth of the locked laser lies below 10 MHz.

In Fig. 2.5 the setup that is used to lock the laser is shown. 5% of the laser light is led to a glass cell. In this cell He 2^3S_1 atoms are produced, by exciting ground state He atoms to the He 2^3S_1 metastable state in a RF induced discharge, with an RF frequency of 23 MHz. It is important that only He atoms are excited in the discharge. Therefore special care is taken to reduce impurities in the He gas. Before the cell is filled with helium it is baked out and pumped down. Then helium is let in through a liquid nitrogen cooled tube. The pressure in the cells is a few times 10^{-1} mBar.

2.4 Metastable helium source

In this section the production of an intense low velocity metastable helium beam is demonstrated. It is used to load a MOT without a Zeeman slower and hence avoids the difficulties encountered in loading a metastable rare gas MOT from a Zeeman slower. Furthermore, we have constructed a magnetic hexapole lens. Because of the low initial velocity of the atoms produced in the source the hexapole lens can efficiently focus the atomic beam.

2.4.1 Construction

The source is shown schematically in Fig. 2.6. In the source metastable helium atoms He(2^1S) and He(2^3S) are produced in a DC-discharge by electron impact. The source is cooled by liquid helium. The discharge runs between a discharge needle and a nozzle plate. A Pyrex glass tube with an orifice of 1 mm inserted in a Teflon holder, is placed in a copper assembly as shown in Fig. 2.6. The gas flows on the outside of the glass tube, along the cold cryostat and cold nozzle, before it expands into the vacuum chamber. Part of the gas is pumped out by a mechanical pump through the glass tube, in the same way as in the design of a liquid nitrogen cooled DC-discharge source by Kawanaka *et al.* [15].

The glass tube and nozzle assembly were placed inside a cryostat, which was cooled to about 10-15 K by liquid helium. Lower temperatures could be obtained

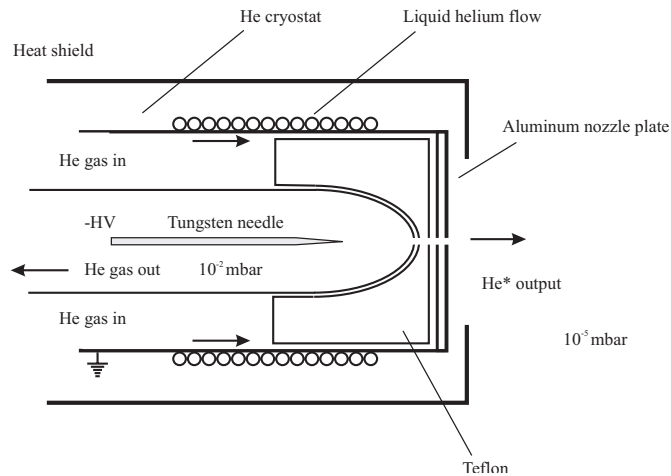


Figure 2.6 Schematic drawing of the source cooled with liquid helium.

but at the expense of instability of the source output. This is possibly due to helium condensation taking place in the source. The cryostat is heat shielded by a gold plated cylinder. The nozzle was made of an aluminum plate of 1 mm thickness to reduce heat gradients (a copper nozzle did not produce as well a discharge as an aluminum one) and the exit hole diameter used was 0.5 mm. As a discharge needle we used a tungsten rod with a diameter of 2 mm, which was sharpened at the end and kept in the middle of the glass tube by ceramic spacers. The optimal distance from the nozzle plate to the discharge needle was found to be 7 mm, ensuring both a high output stability and a high yield of the source. To minimize heating effects the source is operated at a low discharge power of typical 50-100 mW (about 0.1 mA) and a low discharge pressure of 10^{-2} mBar. In this design the helium discharge is burning inside the source, *i.e.* between the discharge needle and the nozzle plate. This is in contrast to conventional metastable sources which operate at higher pressures (a few mBar) with a discharge burning outside the nozzle, *i.e.* between the discharge needle and the skimmer, to reduce quenching of the metastable atoms by the high pressure [11, 16]. We observed that this operation was only possible at higher source pressures and currents, and therefore at higher temperatures. However, we estimated the quenching of the metastables in our design to be of minor importance due to our low source pressure of 10^{-2}

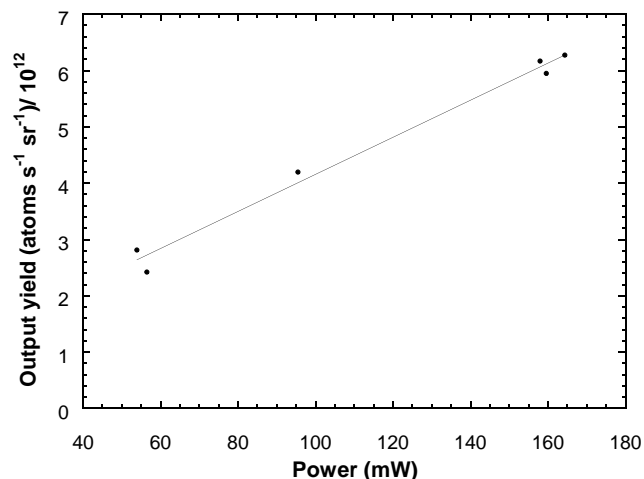


Figure 2.7 Output yield of source as a function of discharge voltage. The contribution from UV photons has been subtracted.

mBar. Operating at minimum power and pressure yields a total flux of a few times 10^{12} atoms/s sr. This output is two orders of magnitude lower than the output of conventional sources, but the mean velocity of the atoms is decreased from 2000 m/s to 300 m/s, as is shown in Sec. 2.4.2. As expected higher source voltages increase the output yield further. This effect is illustrated in Fig. 2.7.

2.4.2 Results

In the source He (2^3S) atoms, He (2^1S) atoms, and UV photons are produced. The atoms and the photons were detected with a channeltron detector, located 60.3 cm away from the source exit. The total number of UV photons in the beam was deduced from time of flight (TOF) measurements discussed below and subtracted from the signal measured with the channeltron detector. The fraction of He 2^1S atoms produced in the source was measured by deflecting all He 2^3S atoms out of the beam with a diode laser resonant with the $2^3S_1 \rightarrow 2^3P_2$ transition. The beam flux was measured with and without deflection, which enabled us to determine the number of singlet atoms. The fraction of singlet atoms was found to be 5–8% of the total beam flux which is rather low compared to previous source designs [16].

The velocity distribution was measured by a TOF technique. Fig. 2.8 shows a typical TOF spectrum together with the corresponding velocity distribution. The TOF spectrum was obtained by the use of a mechanical chopper inserted in the beam. The sharp photon peak in the beginning of the spectrum provided a convenient time zero as well as an indication of the time resolution in this measurement, which was estimated to be better than $2 \mu\text{s}$. Furthermore we used the photon peak to determine the photon flux. We found the photon flux to be approximately 25% of the total source output. The mean velocity of the spectrum shown in Fig. 2.8 is 300 m/s, which corresponds to a temperature of 15 K. In Fig. 2.9 the mean source velocity is plotted against discharge power. As the discharge power increases the

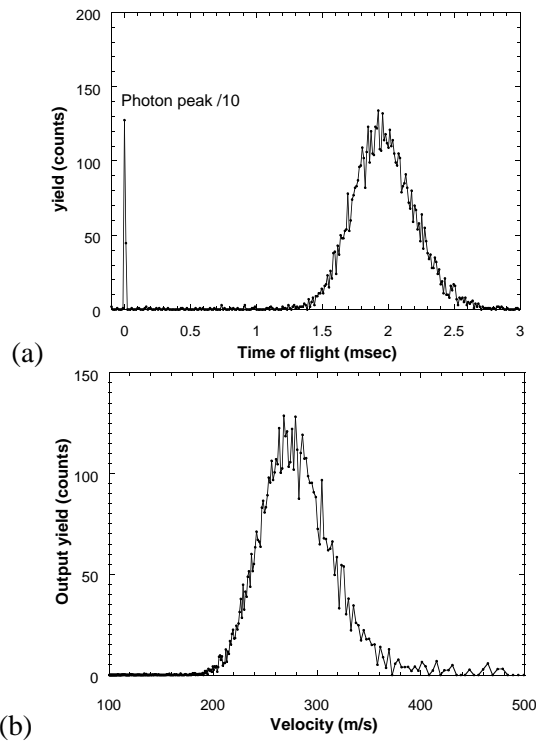


Figure 2.8 Part (a) shows a typical time of flight spectrum obtained using a mechanical chopper. A channeltron detector located 60.3 cm away from the chopper monitored the beam particles and photons. Part (b) displays the corresponding velocity distribution.

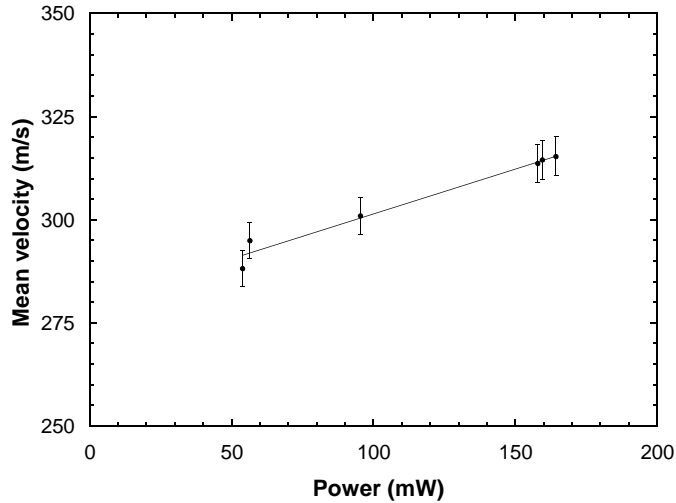


Figure 2.9 Mean velocity of He* beam as a function of discharge power.

mean velocity increases slightly, due to heating of the discharge. At typical settings of the source we find a mean velocity of less than 300 m/s, compared to 1000 m/s for a liquid nitrogen cooled source [15], or 2000 m/s for a conventional source [11, 16].

2.4.3 Loading the MOT

Our source of slow metastable triplet helium atoms is used to load a magneto-optical trap (MOT). A schematic picture of the setup is shown in Fig. 2.10. Usually a MOT for metastable rare gases is loaded from a high-pressure discharge source cooled with liquid nitrogen [4, 17–19]. In that case the helium atoms in the beam need to be slowed down in a Zeeman slower from 1000 m/s to the capture velocity, *i.e.* 60 m/s, of the MOT, before they can be captured in the MOT. Using a Zeeman slower makes the experiment more complex since special care has to be taken to avoid reduction of density of the beam [20]. In a Zeeman magnet the beam is slowed down in the longitudinal direction and as it is slowed down, the transverse part of the velocity becomes more and more dominant. The beam will ultimately fan out and the flux in the center of the beam will strongly decrease. This effect limits the number of atoms that can be captured in the MOT. It can

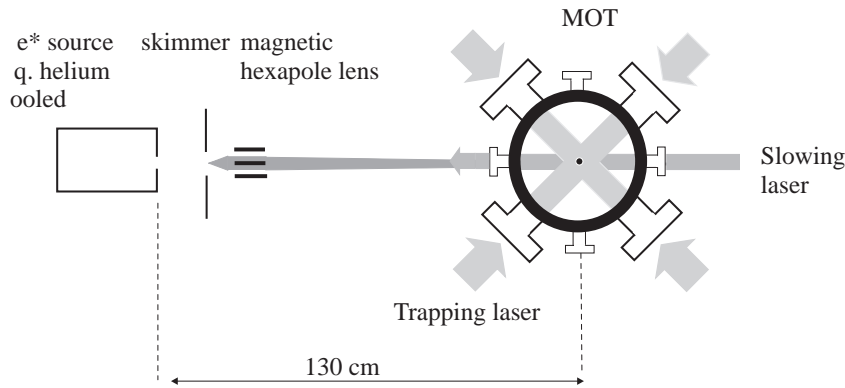


Figure 2.10 Schematic picture of the slowing and trapping setup.

be compensated for by inserting a transverse cooling section in front of and/or at the end of the slowing unit [17]. At the entrance of the slower the velocity of the atoms in the beam is high and consequently the interaction time of cooling light with the atoms is short. This limits the momentum that can be transferred to the atoms. A complication that arises when using a Zeeman slower is extraction of slow atoms from the end of the slower. The extraction can be made more efficient by placing additional coils at the exit of the magnet, or by using an increasing magnetic field [21]. These modifications also shift the atoms out of resonance with the slowing laser light after they have left the slower and hence prevent further deceleration of the beam and broadening of the velocity distribution at that point.

To improve the load characteristics of our He* MOT compared to previous experiments [12, 22], we decided to use the cryogenic helium source instead of a source cooled with liquid nitrogen. Since the mean velocity is only 300 m/s instead of 1000 m/s, we could decrease the length of the experiment considerably and hence increase the loading rate dramatically. The coils that generate the MOT magnetic field in our setup are large in diameter (~ 400 mm). These large coils are particularly favorable for loading a MOT from the cryogenic source, since no additional Zeeman slower is needed. The atoms are slowed down by a counter propagating laser beam, and the Zeeman shift that is needed to compensate the Doppler shift is produced by the radial magnetic field of the MOT. The beam still fans out, but the effect is smaller than for a liquid nitrogen cooled beam for two

reasons. First, due to the lower initial velocity of the atoms the beam does not spread out as much during the deceleration. Second, since the atoms are slowed down in the MOT chamber the beam spreads out most in the region where the trapping laser beams are present. This reduces the losses considerably. Fig. 2.11 shows a simulation of the slowing in the radial MOT magnetic field by a single counter-propagating laser. As a reference we have also plotted the measured and calculated radial magnetic field. The detuning and intensity of the slowing laser that are used in the simulation are identical to the values that are used in the actual experiment, which are given below.

For a slowing laser detuned 40 MHz below the $2^3S_1 \rightarrow 2^3P_2$ asymptote with

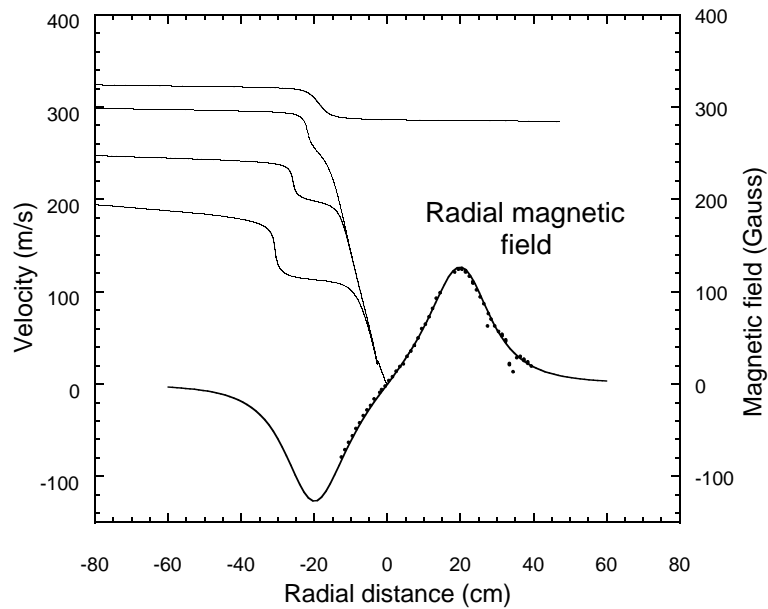


Figure 2.11 Simulation of the deceleration of the slow He* beam in the radial magnetic field of the MOT. For reference we have also added the radial magnetic field component on the graph. The dots are measured magnetic field values. The beam of He* atoms enters the MOT chamber at the negative radial distance side. The simulation is shown for various initial velocities of the atoms. It can be seen that atoms with a velocity smaller than 325 m/s can be slowed down enough to be trapped in the MOT.

a saturation parameter of $s_0 = 400$ we are able to slow down all atoms with a velocity that is less than 325 m/s, *i.e.* most of velocity distribution. Experiments show that it is indeed possible to trap most of the atoms from the slow metastable helium beam. We easily trap about 10^6 atoms in the MOT, where in the previous experiment only 10^5 atoms were trapped by loading the MOT from a liquid nitrogen cooled Zeeman slowed beam [12]. The volume is 1 mm^3 leading to an average density of a few times 10^9 cm^{-3} and the temperature is 1 mK. The total number of trapped atoms is measured with micro-channel plates and the spatial size of the MOT is measured by a CCD camera. In Sec. 2.5 it will be described in more detail how the characteristics of the MOT are determined. With this number and density of atoms we have entered the regime where intra-MOT collisions are more important than collisions with background atoms. This can clearly be seen in Fig. 2.12 where a typical decay curve of the MOT is shown. Since the decay is not a single exponential in time, the main ion production results from intra-MOT collisions [23].

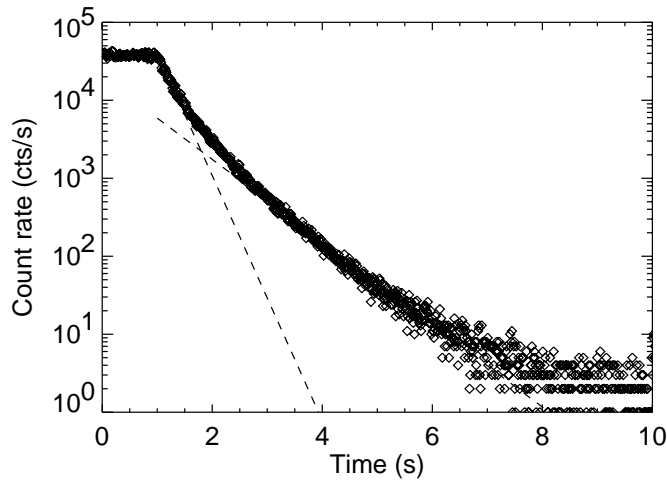


Figure 2.12 Decay curve of the MOT. The loading of the MOT is shut off at $t = 1.0 \text{ s}$. The two dashed lines represent the contributions to the decay rate of intra-MOT collisions (steep slope) and of collisions with background atoms (weak slope).

2.4.4 Hexapole magnetic lens

Our beam line of slow metastable helium atoms offers the possibility of manipulating the initial divergent beam profile with magnetic fields. At these low atomic velocities moderate magnetic field gradients are sufficient to reduce the initial beam divergence and to project a larger part of the flux of the source into the capture region of the MOT. This can result in a significant increase in the number of captured atoms. The best way to accomplish this is by focusing the atoms emerging from the source into the center of the MOT. We have used a magnetic hexapole lens to focus the He^* atoms. In Fig. 2.10 the position of the magnetic lens is shown, and in Fig. 2.13 a schematic picture of the hexapole lens can be seen. We have chosen a hexapole configuration which produces a field gradient that increases linearly with the distance from the center of the hexapole. Metastable atoms with a large divergence thus experience a larger force than atoms with a small divergence and in principle all atoms will be focused into the same focal point. This is in contrast to a quadrupole configuration where the gradient is

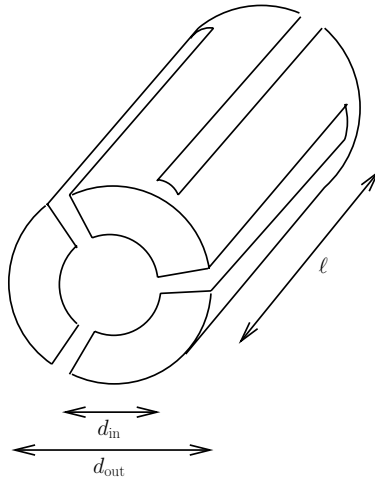


Figure 2.13 Schematic diagram of the hexapole lens. The inner diameter of the tube is $d_{\text{in}}=2.6$ mm, the outer diameter $d_{\text{out}}= 5$ mm and the length $\ell= 40$ mm. Note, that due to the special arrangement of the slots the direction of the current alternates between two adjacent segments.

constant as a function of distance. The hexapole thus resembles a lens for mono-velocity atoms. However, in our case the atoms in the beam have a certain velocity spread and velocity aberration can be important.

The hexapole is constructed from a tube of copper with a length of 40 mm, an inner diameter of $d_{\text{in}} = 2.6$ mm and an outer diameter of $d_{\text{out}} = 5$ mm. The hexapole structure is obtained by cutting 6 slots in the copper tube along its side with a spark cut method such that six wire segments are created (see Fig. 2.13). At each end of the tube 2 neighboring segments remain connected to each other such that the current is allowed to flow alternately in opposite directions. The tube assembly is connected to two wires supplying the current. The distance between each wire segment of the hexapole is about one millimeter. A ceramic tube with an inner diameter of 1.6 mm is put in the hexapole lens to ensure that the segments remain fixed at their positions, avoiding unwanted contact between the segments. Our hexapole structure can take a continuous current of about 15-20 A, without cooling, and a maximum of 80 A for a short period of time. At high currents the surroundings of the lens warm up, leading to an increase in pressure by outgassing and a corresponding quenching of the metastables. Since our hexapole is most efficient at higher currents we plan to use permanent magnets in the future.

To gain knowledge of the hexapole we modeled the atom trajectories and kinematics through the lens. We assume that the magnetic field is generated by six infinite point wires put at a distance a from the center of the hexapole. To test this assumption we have carried out numerical simulations of the actual field and compared it to our analytical results, which will be discussed below, and found that the distance a is just the average of the inner radius $a_{\text{in}} = d_{\text{in}}/2$ and the outer radius $a_{\text{out}} = d_{\text{out}}/2$, or $a = (a_{\text{in}} + a_{\text{out}})/2$. For six point wires we obtain in cylindrical coordinates (r, θ) for the magnetic field:

$$B(r, \theta) = \left(\frac{\mu_0}{4\pi}\right) \frac{12Ir^2}{a^3} \frac{1}{\sqrt{1 + \left(\frac{r}{a}\right)^{12} - 2\left(\frac{r}{a}\right)^6 \cos(6\theta)}}, \quad (2.2)$$

where I is the current sent through each wires. This expression is exact for all points (r, θ) in the plane. For small $r \ll a$ we obtain

$$B(r, \theta) = \left(\frac{\mu_0}{4\pi}\right) \frac{12Ir^2}{a^3}, \quad (2.3)$$

which we find to be valid for $r \leq a/2$. Note that the field depends quadratically on the radius r from the center and thus that the gradient is linearly proportional to the radius. Therefore the hexapole field provides the right field for an atomic

lens. For a quadrupole configuration we obtain an r/a^2 dependence of the field, which does not yield the right dependence for a lens. The interaction between the atom and the magnetic field is given by the Zeeman shift:

$$V = \mu_b g_s m_j B, \quad (2.4)$$

where μ_b is the Bohr magneton, g_s is the spin gyromagnetic ratio, and m_j is the projection of the total electronic angular momentum along the r direction. The force on the atom is given by:

$$F(r) = -\text{grad}V = -\mu_B g_s m_j \frac{\partial B}{\partial r} = -\kappa r, \quad (2.5)$$

with the spring constant κ given by

$$\kappa = \mu_B g_s m_j \left(\frac{\mu_0}{4\pi} \right) \frac{24I}{a^3}. \quad (2.6)$$

We assume the m_j distribution to be random, since the atoms move too fast through the lens for adiabatic following to take place. Thus along the r direction one third of the metastables will be in each of the states $m_j = 0, \pm 1$. For atoms in the $m_j = +1$ state the atoms will be deflected towards the axis of the hexapole, atoms in the $m_j = 0$ state will not experience any influence, while atoms in the $m_j = -1$ state will be deflected away from the axis.

In the hexapole the atoms will undergo an oscillatory motion. If the interaction time $\tau = \ell/v_0$ is small compared to the oscillation period $T = 2\pi/\omega$, where $\omega = \sqrt{\kappa/m}$ is the oscillation frequency, a parallel beam of atoms will be focused at a distance f from the lens given by

$$f = \frac{m v_0^2}{\kappa \ell} \quad (2.7)$$

and f thus represents the focal length of our lens. Here we have assumed that $\tau/T \ll 1$, *i.e.* we have made the thin lens approximation, which is not strictly valid in our case, but without this approximation we obtain equivalent results. Note, that the focal length of the lens is proportional to the square of the velocity and thus shows strong velocity aberrations. In our case, we can generate a gradient of $d^2B/dr^2 = 6000 \text{ G/cm}^2$ with a current of 20 A and for atoms with a velocity of 300 m/s we obtain a focal length of 12 cm.

In the present setup we are not interested in the focal properties of the lens, since the spread in the velocity of the atoms is too high. Instead we are interested

to use the hexapole lens to boost the flux of atoms which can be loaded in the MOT. Solving the equation of motion for a given velocity and entrance coordinate in the hexapole enables us to determine the impact position in the detector plane located approximately 1.6 m away from the hexapole. In the calculation we assumed the initial beam profile to be Gaussian and the velocity distribution, depicted in Fig. 2.8, to be of the form

$$f(v) = Cv^3 \exp\left(-\left(\frac{v - v_0}{\Delta v}\right)^2\right), \quad (2.8)$$

where C is a normalization constant, $v_0=300$ m/s is the mean velocity and $\Delta v=50$ m/s describes the width of the distribution. The beam profile $P(r)$ in the detector plane is obtained from

$$P(r) = \int_0^\infty A(v, r) f(v) dv, \quad (2.9)$$

where $A(v, r)$ is the beam profile transformed first by the hexapole and then by propagation to the detector plane.

We have calculated the beam profile for a number of values of the current through the hexapole, varying from $I = 20$ A to $I = 100$ A, and also measured the beam profile for various values of I . The maximum calculated flux enhancement is a factor of 12. The detector can only be scanned in one direction and might not be at the optimal position perpendicular to the scanning direction, since a small misalignment of the hexapole lens can have a large effect at the distance where the detector is placed. Therefore we have plotted the enhancement of the flux at a fixed position of the detector and used the calculation that fits the measurements the best. The measurements and the calculations are plotted in Fig. 2.14, where the background of UV photons and He (2^1S) atoms has been subtracted from the measured signal. It can be seen that if the current scale of the calculations is multiplied by a factor of 2, the agreement between the measurements and the calculations is rather well.

A few assumptions have been made in the calculations that might explain this discrepancy in the current scale. First of all, we have assumed that the He* source is a point source, while in reality the diameter of the nozzle is too large and the source is too close to the lens to be regarded as a point source. Furthermore, the atoms might spiral through the lens due to the magnetic field, since the velocity of the atoms has both a radial and a longitudinal component as a result of the finite

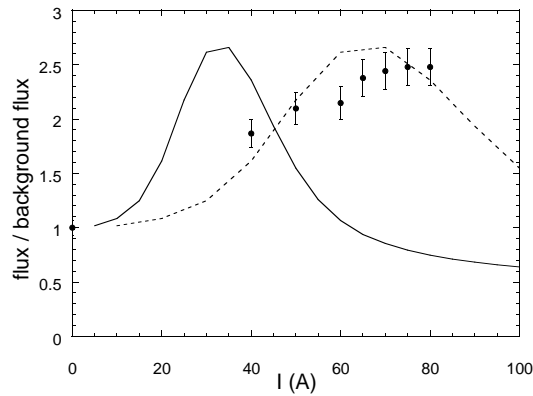


Figure 2.14 Comparison of the measured flux enhancement due to the hexapole lens as a function of the current I compared to the calculated flux enhancement. The dots are the measured values, the solid line is the calculation and the dashed line is the calculation where the current scale has been multiplied by 2 to obtain better agreement with the measurements.

extent of the source. Finally, we have not been able to measure the magnetic field in the hexapole, to check whether our calculations are correct.

We can conclude that we can indeed enhance the beam flux with the hexapole magnet, although not in the way we expected. To improve the flux even more the hexapole lens should be positioned farther away from the source, so that a lens with a larger focal length should be optimal and hence lower currents could be used. Another possibility is to use permanent magnets to create the magnetic hexapole field in order to obtain higher field gradients.

2.4.5 Conclusions

We have constructed an intense low velocity beam of metastable helium atoms. The mean velocity is about 300 m/s and the output yield 10^2 atoms/s sr. The beam is used to improve the loading characteristics of a MOT. To further improve the beam flux we have started to investigate the possibility of using a magnetic hexapole lens to focus the beam. Initial studies show a factor of 2.5 increase in the beam flux but more is expected when the hexapole is constructed from permanent magnets.

2.5 Characteristics of the MOT

In Sec. 2.2.2 the basic principles of the operation of the MOT are explained. In this section the characteristics of the cloud of trapped atoms and the manner in which they are determined will be discussed.

In Fig. 2.15 a picture of the MOT chamber is shown, together with the optics used for the trapping laser. Furthermore a set of two micro-channel plates (MCPs) is shown, which is used for the detection of ions and He* neutrals. In front of the MCPs a grid is placed which is used to either attract or repel the positive ions which are created during Penning ionization of colliding He* atoms. The MCPs have a diameter of 18 mm.

The trapping laser beam is blown up to a size of $40 \times 20 \text{ mm}^2$. The saturation parameter s_0 is 70 per beam. One laser beam provides the configuration of six laser beams shown in Fig. 2.2b. It is recycled for all directions, by reflecting it 18 times. The trapping laser runs at a detuning of $\Delta = -20 \text{ MHz}$, or -12.5Γ .

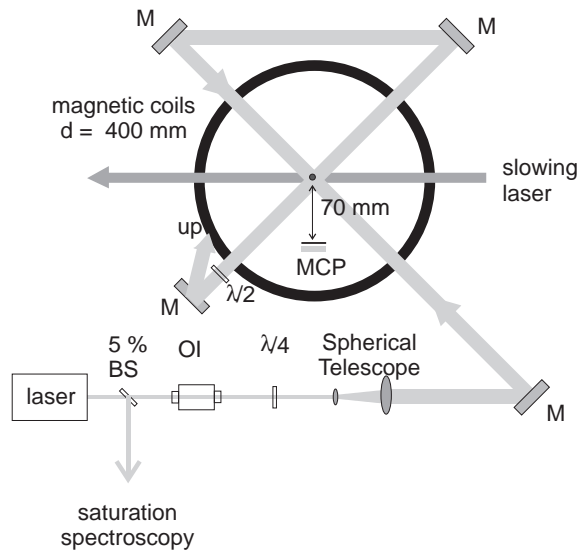


Figure 2.15 MOT chamber and trapping laser beam. BS stands for beam splitter, OI for optical isolator, $\lambda/4$ for quarter wave retardation plate, M for mirror, $\lambda/2$ for half wave retardation plate and MCP for micro-channel plates.

When the trap is on, we typically measure 10^6 ions/s. The major ion production comes from intra-MOT collisions and only a small fraction results from collisions between trapped atoms and background gas atoms, as can be deduced from the decay curve shown in Fig. 2.12.

The magnetic field coils that generate the quadrupole field have an inner radius $R_i = 180$ mm and an outer radius $R_o = 235$ mm. The typical current through the coils is 10 A and the number of windings is 588. The magnetic field gradient in the z-direction is 15 Gauss/cm. The coils are water-cooled.

2.5.1 MOT temperature

The temperature of the atoms in the MOT is determined by means of a time of flight method. The atoms in the MOT are released, by detuning the frequency of the trapping beam far to the red of the $2^3S_1 \rightarrow 2^3P_2$ transition. The metastables make ballistic trajectories and part of them hit the MCPs which are located 70 mm from the center of the vacuum chamber, perpendicular to the x-y plane. The metastables are measured as a function of their arrival time at the MCPs. The

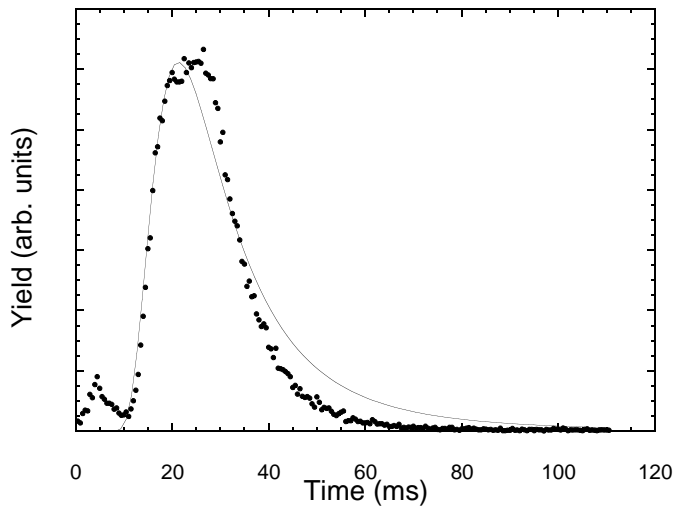


Figure 2.16 TOF measurement of the He* atoms in the MOT. The dots are the measurement and the line is the the fitted Maxwell Boltzmann distribution.

spectrum can be fitted with a Maxwell-Boltzmann distribution, that is given by

$$f(t) \propto \left(\frac{M}{3k_B T} \right)^{3/2} \frac{L^3}{t^4} e^{-ML^2/6k_B T t^2}, \quad (2.10)$$

where M is the mass, T is the temperature, L is the traveled distance, and t is the time.

A TOF spectrum is shown in Fig. 2.16. From the fit of this spectrum we find a temperature of the MOT that is 1.3 mK. The agreement between the fit and the data points is not very good, and we can conclude that velocities of the trapped atoms do not have a pure Maxwell-Boltzmann distribution. In the fit we did not take gravity into account, since the effect of the gravity is negligibly small. We have no explanation for the peak in the spectrum at small time scales. The mean velocity of the atoms in the MOT is 2 m/s. If we integrate all the counts in the spectrum and take the solid angle and the detector efficiency into account, we find the number of atoms in the MOT, which is $8 \cdot 10^5$ in this case.

2.5.2 Spatial distribution

The spatial distribution in the MOT is measured by exciting the He* atoms to the 3^3D state, using visible light, as was first done by Kumakura and Morita [24]. For this purpose a dye laser beam is used with a wavelength of 587.6 nm. A fraction

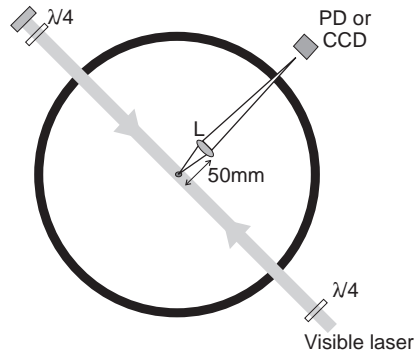


Figure 2.17 Imaging setup. M stands for mirror, $\lambda/4$ for quarter wave retardation plate, L for lens, PD for photo diode and CCD for CCD camera

of the laser light is led to a glass cell filled with helium to find the $2^3P \leftrightarrow 3^3D$ transition. In the cell He 2^3S_1 atoms are produced, which are excited to the 2^3P_2 -state in the manner described in Sec. 2.3. The atoms in the MOT are irradiated with light which has a saturation parameter s_0 of the order 1. The laser beam is circularly polarized and is retro-reflected. The trapped cloud is slightly disturbed by the visible laser beam. It is elongated in the direction of the laser beam and the temperature is increased from 1.3 mK to 1.7 mK.

A lens is placed in the vacuum chamber, as is shown in Fig. 2.17, in order to maximize the solid angle for the fluorescence and to enlarge the image of the trapped atoms. Outside the vacuum chamber, at the position of the image, either a CCD camera or a photodiode can be placed. The CCD camera has an array of 752×582 pixels and is used to measure the spatial profile of the cloud. The photodiode is used to monitor the emitted fluorescence, which is a measure for the number of trapped atoms.

A typical image, taken with the CCD camera is shown in Fig. 2.18a. A cross section through the cloud is shown in Fig. 2.18b. With the CCD camera we can determine r_x and $r_{yz} = \sqrt{r_y^2 + r_z^2}$, by fitting the cross section with a Gaussian distribution. Here r_x is the 1/e half width in the direction of the visible laser beam, r_y is the 1/e half width in the horizontal plane perpendicular to the direction of r_x , and r_z the 1/e half width in the vertical direction. To obtain r_y and r_z from r_{yz} we have assumed that r_y is a factor of $\sqrt{2}$ larger than r_z , due to the difference in the magnetic field gradient in the **y**- and **z**- direction. From the fit follows then that $r_x = 0.61$ mm, and $r_y = 0.37$ mm, and $r_z = 0.26$ mm. In the direction of the visible laser beam the cloud is elongated, because it is perturbed by the laser. When the visible laser beam is off, r_x should be equal to r_y . We use the sizes without the laser beam and the number of atoms to find the central density in the atomic cloud, which is $2 \cdot 10^9 \text{ cm}^{-3}$.

The visible fluorescence measured with the photodiode is 2.5 nW. The photodiode is calibrated for the wavelength of 587 nm. If the fraction of atoms in the 3^3D state is known the number of atoms in the trap N can be calculated using the following formula:

$$N = \frac{f}{\eta_e \eta_d h \nu \rho_d \Gamma}, \quad (2.11)$$

where f is the measured fluorescence, $\eta_e = 0.016$ is the geometrical detection efficiency, η_d is the detection efficiency taking into account losses due to scattering on optical elements and is estimated to be 25%, $h \nu = 3.377 \cdot 10^{-19}$ J is the energy of the photons, $\Gamma = 71.4$ MHz is the natural line width of the doubly excited

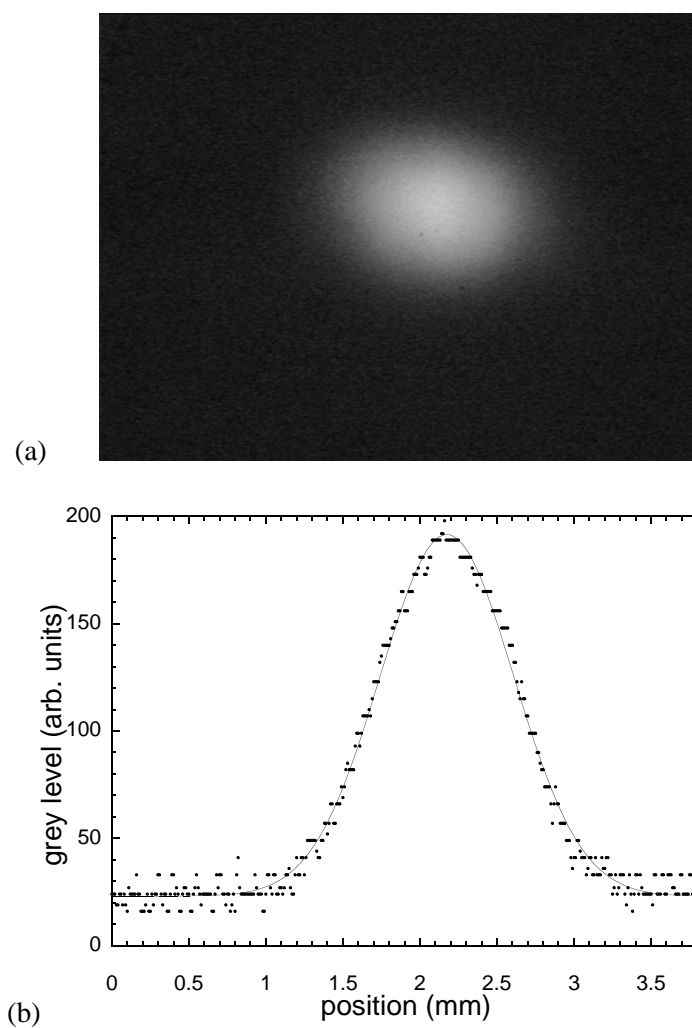


Figure 2.18 Image of the MOT taken with the CCD camera. The upper part shows the image, the lower part a horizontal cut trough the center of the cloud. The line is a fit with a Gaussian distribution

state and $\rho_d = 0.05$ is the fraction of atoms in the excited state. The excited state population is found by numerically solving the optical Bloch equations for a

coupled three-level system. From the numbers above it follows that the measured fluorescence corresponds to a number of atoms of $1.6 \cdot 10^5$. This number is smaller than the number of atoms that is deduced from the TOF measurement discussed in Sec. 2.5.1. A reason for this might be the disturbance of the cloud of trapped atoms by the visible laser light.

2.6 Conclusions

We have constructed an intense source of slow He* atoms. The beam of atoms is used to load a MOT. As a result of the small initial velocity of the atoms it is possible to capture them into the trap without making use of a Zeeman slowing unit, which simplifies the experiment. The loading characteristics of our MOT have been improved with respect to previous experiments [12,22]. The density in the MOT has reached the regime where intra-MOT collisions are dominant over collisions between atoms in the MOT and background gas atoms. This makes our MOT a useful tool to study interactions between ultra-cold atoms.

We have studied and described the properties of the cloud of trapped atoms. We have a cloud of about 10^6 atoms, with a density of a few times 10^9 cm^{-3} and a temperature of about 1 mK.

References

- [1] T.W. Hänsch and A.L. Schawlow, *Opt. Comm.* **13**, 68 (1975).
- [2] D. Wineland and H. Dehmelt, *Bull. Am Phys. Soc.* **20**, 637 (1975).
- [3] J. Weiner, *Adv. Atom. Mol. Opt. Phys.* **35**, 45 (1995).
- [4] H. C. Mastwijk, J. W. Thomsen, P. van der Straten, and A. Niehaus, *Phys. Rev. Lett.* **80**, 5516 (1998).
- [5] M.H. Anderson, J.R. Ensher, M.R. Matthews, C.E. Wieman, E.A. Cornell, *Science* **269**, 198 (1995).
- [6] P. D. Lett, P. S. Julienne, and W. D. Phillips, *Annu. Rev. Phys. Chem.* **46**, 423 (1995).
- [7] M. Walhout, U. Sterr, C. Orzel, M. Hoogerland, and S. L. Rolston, *Phys. Rev. Lett.* **74**, 506 (1995).
- [8] N. Herschbach, P.J.J. Tol, W. Vassen, W. Hogervorst, G. Woestenenk, J.W. Thomsen, P. van der Straten, and A. Niehaus, *Phys. Rev. Lett.* **84**, 1874 (2000).

- [9] H.J. Metcalf and P. van der Straten, *Laser Cooling and Trapping*, Springer-Verlag, New York (1999).
- [10] S. Chu, L. Hollberg, J.E. Bjorkholm, A. Cable, and A. Ashkin, *Phys. Rev. Lett.* **55**, 48 (1985).
- [11] D.W. Fahey, W.F. Parks, and L.D. Scheerer, *J. Phys. E: Sci. Instrum.* **13**, 38 (1980).
- [12] H. C. Mastwijk, *Cold Collisions of Metastable Helium atoms*, Ph.D. Thesis, Utrecht University, (1997).
- [13] W. Phillips, and H. Metcalf, *Phys. Rev. Lett.* **48**, 596 (1982).
- [14] E. Raab, M. Prentiss, A. Cable, S. Chu, and D. Pritchard, *Phys. Rev. Lett.* **59**, 2631 (1987).
- [15] J. Kawanaka, M. Hagiuda, K. Shimizu, F. Shimizu, and H. Takuma, *Appl. Phys. B* **56**, 21 (1993).
- [16] K. Ohno, T. Takami, K. Mitsuke, and T. Ishida, *J. Chem. Phys* **94**, 2675 (1991).
- [17] P. J. J. Tol, N. Herschbach, E. A. Hessels, W. Hogervorst, and W. Vassen, *Phys. Rev. A* **60**, R761 (1999).
- [18] M. Kumakura, and N. Morita, *Phys. Rev. Lett.* **82**, 2848 (1999).
- [19] A. Browaeys, J. Poupard, A. Robert, S. Nowak, W. Rooijackers, E. Arimondo, L. Marcassa, D. Boiron, C. Westbrook, and A. Aspect *Eur.Phys.J.D* **8**, 199 (2000).
- [20] P. A. Molenaar, P. van der Straten, H.G.M. Heideman, and H. Metcalf, *Phys. Rev. A* **55**, 605 (1997).
- [21] T.E. Barrett, S.W. Dapore-Schwartz, M.D. Ray, and G.P. Lafyatis, *Phys. Rev. Lett.* **67**, 3483 (1991).
- [22] H.C. Mastwijk, M. van Rijnbach, J.W. Thomsen, P. van der Straten, and A. Niehaus, *Eur. Phys. J. D.* **4**, 131 (1997).
- [23] F. Bardou, O. Emile, J.-M. Courty, C.I. Westbrook, A. Aspect, *Europhys. Lett.* **20**, 681 (1992).
- [24] M. Kumakura and N. Morita, *Jpn. J. Appl. Phys.* **31**, L276 (1992).

Chapter 3

Long-Range States of He_2^*

3.1 Introduction

Collisions of cold atoms primarily probe the molecular interactions at large inter-nuclear distances. To obtain insight into these collisions it is important to have a good description of the long-range potentials. The experiments which are described in this thesis involve collisions between two cold He^* atoms. For collisions of cold alkali atoms the long-range potentials have been studied both experimentally and theoretically [1,2]. We have applied similar methods as have been used for alkali atoms to describe the long-range interactions between cold He^* atoms theoretically. The methods we use and the results that are obtained will be described in this chapter.

First the angular momenta, which play a role in collisions and in the formation of molecules, will be discussed in Sec. 3.2. In Sec. 3.3 the molecular eigenstates for $2^3S_1 - 2^3S_1$ and the $2^3S_1 - 2^3P_{0,1,2}$ system are described. The potential curves are calculated in Sec. 3.4 and their behavior is discussed in Sec. 3.5. The contribution of partial waves to the collision is discussed in Sec. 3.6. Penning ionization is briefly described in Sec. 3.7.

3.2 Angular momenta

It is important to carefully define the angular momenta which play a role in collisions between atoms and in the formation of molecules. In this section notations for the angular momenta are given, that will be used throughout the whole thesis.

The angular momenta of the atoms a and b involved in the collision are given below:

$l_{a,b}$: electronic orbital angular momentum
 $s_{a,b}$: electronic spin
 $\mathbf{j}_{a,b}$: total electronic angular momentum, $\mathbf{j} = \mathbf{l} + \mathbf{s}$
 $m_{a,b}$: projection of $\mathbf{j}_{a,b}$ on the internuclear axis

The angular momenta for the molecule can be expressed in terms of the angular momenta of the atom. They are:

$\mathbf{L} = \mathbf{l}_a + \mathbf{l}_b$: total electronic orbital angular momentum
 $\mathbf{S} = \mathbf{s}_a + \mathbf{s}_b$: total electronic spin
 ℓ : nuclear rotational angular momentum
 $\mathbf{J} = \mathbf{L} + \mathbf{S} + \ell$ total molecular angular momentum
 $j = \mathbf{L} + \mathbf{S}$: total electronic angular momentum

The general dipole selection rules apply and they can be found in textbooks [3].

The molecular quantum numbers are not good quantum numbers at all internuclear distances, depending on the coupling between the total electronic spin, \mathbf{S} , and the molecular orbital angular momentum, \mathbf{L} . The limiting coupling cases can be treated in terms of the various Hund's cases, which are described in Ref. [3]. In the present context Hund's case (a) and Hund's case (c) are relevant and therefore they will be discussed below.

3.2.1 Hund's case (a)

At short internuclear distances the electronic motion is strongly coupled to the internuclear axis and the molecule is described by Hund's case (a). A schematic picture of the molecule in Hund's case (a) is shown in Fig. 3.1. In this case the projection of \mathbf{L} on the internuclear axis, which is denoted by Λ , and the projection of \mathbf{S} on the internuclear axis, which is denoted by Σ , are good quantum numbers. The projection of j on the internuclear axis, which is denoted by Ω , is also a good quantum number. It is defined as $\Omega = \Lambda + \Sigma$. States which have quantum numbers of $\pm\Omega$ are degenerate, so only positive eigenvalues of Ω are used. The Hund's case (a) states are labeled with $^{2S+1}\Lambda_{g,u}^{\pm}$. The g,u and the \pm labels represent symmetry properties of the molecule and will be discussed in Sec. 3.2.3. The notation for $\Lambda = 0$ is Σ , for $\Lambda = 1$ it is Π , etc.

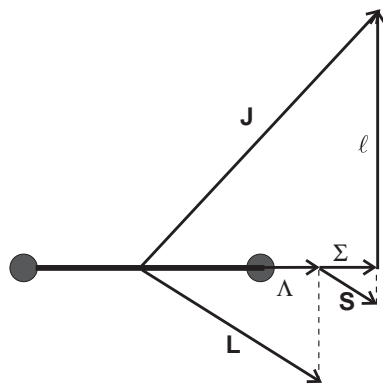


Figure 3.1 Vector diagram for Hund's case (a). The angular momenta are defined in the text.

3.2.2 Hund's case (c)

The Hund's case (c) description is valid when the spin-orbit coupling is stronger than the coupling to the internuclear axis. This is the case at large internuclear

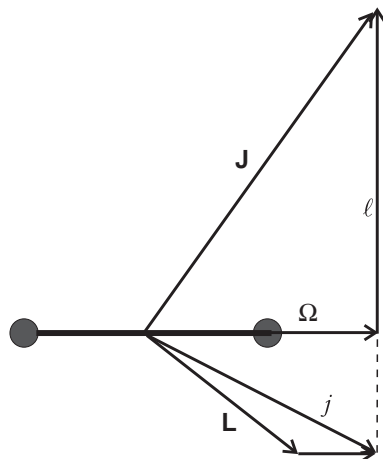


Figure 3.2 Vector diagram for Hund's case (c). The angular momenta are defined in the text.

distances. In the experiments described in this thesis the excitations from the S-S potential to the S-P potential are made at these distances.

In Fig. 3.2 a schematic picture of the molecule in Hund's case (c) is shown. Since \mathbf{L} and \mathbf{S} are strongly coupled, they are no longer good quantum numbers. The projection of j on the internuclear axis, Ω , is now a good quantum number. The Hund's case (c) states are labeled with $\Omega_{g,u}^{\pm}$, where g,u and \pm are the same labels for symmetry properties as in Hund's case (a). The notation for $\Omega = 0$ is 0, for $\Omega = 1$ it is 1, etc.

3.2.3 Symmetry rules

Homonuclear diatomic molecules have symmetry properties. Due to these symmetries some combinations of quantum numbers are not allowed. In this section various symmetry rules will be discussed. Some of them are used to label the molecular states. The other symmetry relations that we discuss are used to exclude some combinations of quantum numbers.

First we describe the two symmetry properties that are used to label the molecular states. The reflection of the molecule in the center of mass is denoted as i_e . The wavefunction can be either symmetric or anti-symmetric for this reflection:

$$i_e |\Psi_{mol}\rangle = (-1)^{\sigma} |\Psi_{mol}\rangle. \quad (3.1)$$

The wavefunction with $\sigma = 0$ is named *gerade* (g) and the wavefunction with $\sigma = 1$ is named *ungerade* (u). The corresponding labels that are used are g and u .

States with $\Lambda \neq 0$ or $\Omega \neq 0$ are doubly degenerate. The non-degenerate states, with $\Lambda = 0$ or $\Omega = 0$, can be labeled with their symmetry property for reflection of the wavefunction in a plane containing the internuclear axis. When the wavefunction changes sign it is labeled with $-$ and when it remains unchanged it is labeled with $+$.

For the analysis of the experimental results discussed in this thesis we use symmetry rules to find allowed combinations of quantum numbers. The combinations that are relevant for the analysis of the experiments are discussed below. First we consider the exchange of two colliding He^* atoms, which will be denoted as v_n . Since the He^* atoms are bosons, the molecular wavefunction must be symmetric when the two atoms are exchanged. The exchange of two atoms corresponds to applying both the operations $\mathbf{k} \rightarrow -\mathbf{k}$, where \mathbf{k} is the wave number for the relative motion of the two atoms, and $\mathbf{j}_a \mathbf{m}_a \leftrightarrow \mathbf{j}_b \mathbf{m}_b$. The exchange rules for

Clebsch-Gordon coefficients [4] are used to find that the exchange corresponds to:

$$v_n |\Psi_{mol}\rangle = (-1)^{\ell+j-j_a-j_b} |\Psi_{mol}\rangle. \quad (3.2)$$

Therefore $\ell + j - j_a - j_b$ must be even. When two He 2^3S_1 atoms are colliding, $j_a = j_b = 1$. It then follows from Eq. 3.2 that when j is even, ℓ must be even too.

The other symmetry relation is deduced from the exchange of the electrons positioned at the two different nuclei. Due to the Pauli exchange principle, the wavefunction must be anti-symmetric for the exchange of two electrons. This operation is denoted as v_e . For the electronic spin wavefunction $|\chi_e\rangle$ this operation corresponds to:

$$v_e |\chi_e\rangle = (-1)^{S+1} |\chi_e\rangle, \quad (3.3)$$

as will be shown in Sec. 3.3.1. The electronic exchange, when the spin part is not included, corresponds to the operations $\mathbf{k} \rightarrow -\mathbf{k}$ and i_n , where i_n is the inversion of the nuclei with respect to the center of mass. Inverting the nuclei corresponds to the operations i_e and i_t , where i_t is the inversion of all spatial coordinates with respect to the center of mass. Thus it follows that:

$$v_e |\Psi_{mol}\rangle = (-1)^{S+1+\sigma+\pi_a+\pi_b+2\ell} |\Psi_{mol}\rangle = -\Psi_{mol}, \quad (3.4)$$

where $\pi_{a,b}$ is the parity of the atomic wavefunction for atom a or b . Therefore $S + \sigma + \pi_a + \pi_b$ must be even. In a He $2^3S_1 - 2^3S_1$ molecule $\pi_a = \pi_b = 0$, so $S + \sigma = \text{even}$. Therefore wavefunctions with total spin $S = 0$ (singlet) and total spin $S = 2$ (quintet) must have *gerade* symmetry and wavefunctions with total spin $S = 1$ (triplet) must have *ungerade* symmetry.

3.3 Molecular wavefunctions

In this section we construct the wavefunctions for the He $2^3S_1 - 2^3S_1$ system and the He $2^3S_1 - 2^3P_{0,1,2}$ system. First the electronic spin states will be described and then the spatial part of the wavefunction will be given, for both the potentials connected to the $2^3S_1 - 2^3S_1$ asymptote and the potentials connected to the $2^3S_1 - 2^3P_{0,1,2}$ asymptotes. The number of states is found and the labels for the states are given. In this section only the Hund's case (a) states are discussed, *i.e.* these states are eigenstates only at short internuclear distances.

3.3.1 Spin states

Both the atoms in the 2^3S_1 state and the atoms in the $2^3P_{0,1,2}$ state have a spin of $s_{a,b} = 1$. These spins combine to singlet, triplet and quintet spin wave functions. To avoid lengthy notations $s_{a,b} = 1; m_s = +1$ will be denoted as $\uparrow\uparrow$, $s_{a,b} = 1; m_s = 0$ as \Leftrightarrow and $s_{a,b} = 1; m_s = -1$ as $\downarrow\downarrow$. The lowest quintet state is $\downarrow\downarrow$. The other quintet states are found by applying the ladder operator S_{\pm} . There are 5 quintet states which have $m_s = 0, \pm 1, \pm 2$. The lowest triplet state, with $m_s = -1$, must be orthogonal to the ${}^5\chi_{-1}$ state, where ${}^{2S+1}\chi_{m_s}$ is the spin wavefunction. The other triplet states are found using the ladder operator again. Finally the singlet state must be orthogonal to both the ${}^5\chi_0$ and the ${}^3\chi_0$ state. We find the following combinations for the spin states of the molecule:

$$\begin{array}{lll}
 {}^1\chi_0 = \uparrow\downarrow - \Leftrightarrow\uparrow + \downarrow\uparrow & & \\
 {}^3\chi_{+1} = \uparrow\uparrow - \Leftrightarrow\uparrow & {}^3\chi_0 = \uparrow\downarrow - \downarrow\uparrow & {}^3\chi_{-1} = \downarrow\downarrow - \Leftrightarrow\downarrow \\
 {}^5\chi_{+2} = \uparrow\uparrow & {}^5\chi_{+1} = \uparrow\uparrow + \Leftrightarrow\uparrow & {}^5\chi_0 = \uparrow\downarrow + 2\Leftrightarrow\uparrow + \downarrow\uparrow \\
 {}^5\chi_{-1} = \downarrow\downarrow + \Leftrightarrow\downarrow & {}^5\chi_{-2} = \downarrow\downarrow &
 \end{array} \tag{3.5}$$

The singlet and quintet spin functions are symmetric under exchange of a pair of electrons and the triplet spin function is anti-symmetric under exchange of an electron pair.

3.3.2 He 2^3S_1 - 2^3S_1 molecular wavefunctions

In this section we discuss the wavefunctions for the potentials connected to the 2^3S_1 - 2^3S_1 asymptote, which describe both the spatial and the spin part of the wavefunction.

Atom a has two electrons, ($1s2s$), with spin $s_a = 1$ and $m_s = -1, 0, 1$. The same is true for atom b . Since for both atoms the electrons are in the ($1s2s$) state, the electronic orbital angular momenta are $l_a = l_b = 0$ and $m_a^l = m_b^l = 0$. Therefore there are $3 \times 3 = 9$ potentials which connect to the 2^3S_1 - 2^3S_1 asymptote. The wavefunctions have been found using Slater determinants to make sure that the wavefunctions obey the Pauli principle, *i.e.* they are anti-symmetric for the exchange of two electrons [5].

The 9 wavefunctions that we found can be described by the ${}^1\Sigma_g^+$ state, the ${}^3\Sigma_u^+$ state and the ${}^5\Sigma_g^+$ state. The wavefunctions are symmetric when they are reflected in a plane containing the internuclear axis and therefore all wavefunctions are labeled with +, as was discussed in Sec. 3.2.3. The wavefunctions fulfill the requirements already formulated in Eq. 3.4, that the singlet and the quintet

states must have *gerade* symmetry, while the triplet states must have *ungerade* symmetry.

3.3.3 He $2^3S_1 - 2^3P_{0,1,2}$ molecular wavefunctions

We follow the same procedures as in Sec. 3.3.2 to obtain the wavefunctions for the potentials connected to the $2^3S_1 - 2^3P_{0,1,2}$ asymptote. We assume that the electron configuration for atom a is $(1s2s)$. The electronic orbital angular momentum is $l_a = 0$ with $m_a^l = 0$ and the spin momentum is $s_a = 1$, with $m_s = -1, 0, 1$. Therefore there are 3 possible states for atom a . The electron configuration for atom b must then be $(1s2p)$. The electronic orbital angular momentum is $l_b = 1$ and can be aligned in three ways, $m_b^l = -1, 0, 1$. Furthermore, the electronic spin $s_b = 1$ can be also aligned in three ways, $m_b^s = -1, 0, 1$. This results in $3 \times 3 = 9$ possible states for atom b . Since in addition atoms a and atom b can be exchanged, there are in total $3 \times 9 \times 2 = 54$ possible states, which connect to the $2^3S_1 - 2^3P_{0,1,2}$ asymptotes. There are 6 singlet states, 18 triplet states and 30 quintet states. Again the Slater determinants have been used to find the spatial part of the wavefunction. Linear combinations of Slater determinants have been made to construct wavefunctions which are anti-symmetric when two electrons are exchanged. The wavefunctions can be described by the $^{1,3,5}\Sigma_{g,u}^+$ states and $^{1,3,5}\Pi_{g,u}$ states. The Π states are doubly degenerate. The wavefunctions with $\Lambda = 0$ all remain unchanged when they are reflected in a plane containing the internuclear axis and hence are all labeled with $+$.

3.4 Calculation of long-range potentials

In the analysis of the experimental results mainly the long range potential curves which connect to the S-P asymptote are used. In this section only the S-P long-range potentials will be discussed, since they are most relevant for the analysis done in this thesis. The long-range potentials which connect to the S-S asymptote can be constructed in a similar way.

To calculate the long-range behavior of the S-P potential curves, we consider a pseudo two-electron system, since only the two outer electrons, the electron in the 2s and the electron in the 2p state, play a role in the interaction. The long-range interaction is determined by the Coulomb interactions and can be described by:

$$V_{int} = \frac{1}{|\mathbf{R}|} - \frac{1}{|\mathbf{R} - \mathbf{r}_a|} - \frac{1}{|\mathbf{R} + \mathbf{r}_b|} + \frac{1}{|\mathbf{R} + \mathbf{r}_b - \mathbf{r}_a|}, \quad (3.6)$$

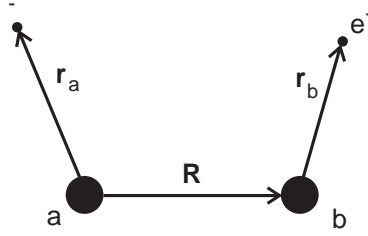


Figure 3.3 Coordinate system for a diatomic molecule with two active electrons. The nuclei are at positions a and b . The position of nucleus b with respect to nucleus a is \mathbf{R} , \mathbf{r}_a is the position of electron a with respect to nucleus a , and \mathbf{r}_b is the position of electron b with respect to nucleus b .

where the distances \mathbf{R} , \mathbf{r}_a , and \mathbf{r}_b are defined in Fig. 3.3. The first term gives the Coulomb interaction between the nuclei, the second term the interaction between electron a and nucleus b , the third term the interaction between electron b and nucleus a and the last term the interaction between the two electrons. If the two electron wavefunctions do not overlap appreciably, the interaction potential can be expanded in a multipole expansion [6]:

$$V_{int} = \sum_{\alpha, \beta=1}^{\infty} H_{\alpha, \beta}(\hat{R}), \quad (3.7)$$

where

$$H_{\alpha, \beta}(\hat{R}) = (-1)^\beta C_{\alpha, \beta} \frac{r_a^\alpha r_b^\beta}{R^{\alpha+\beta+1}} \sum_{\lambda=-\alpha}^{\alpha} \sum_{\mu=-\beta}^{\beta} Q_{\lambda, \mu} Y_{\alpha, \lambda}(\hat{r}_a) Y_{\beta, \mu}(\hat{r}_b) Y_{\alpha+\beta, \lambda+\mu}^*(\hat{R}), \quad (3.8)$$

where $C_{\alpha, \beta}$ and $Q_{\lambda, \mu}$ are constants, $Y_{l, m}$ is the spherical harmonic, and r_a^α stands for $r_a = |r_a|$ to the power α . The order of the multipole terms in the expansion is given by α and β .

We now want to calculate $\langle j | V_{int} | k \rangle$. In order to do this we must choose a basis set, for which we use a combination of atomic wavefunctions:

$$|j\rangle = |n_a l_a m_a^l; n_b l_b m_b^l\rangle, \quad (3.9)$$

where $l_{a, b}$ is defined in Sec. 3.2 and $m_{a, b}^l$ is the projection of $l_{a, b}$ on the internuclear axis. From the relation in Eq. 3.8 it follows that $m_a + m_b$ is preserved, *i.e.* $m_a +$

$m_b = m'_a + m'_b$. We can find the matrix elements $\langle j | V_{int} | k \rangle$ in terms of the multipole expansion and diagonalize the matrix elements to obtain the interaction potential.

For the S-P potential the $|s0; pm\rangle$ states and the $|pm; s0\rangle$ states are coupled by the dipole interaction. Therefore the first non-zero term in the multipole expansion is the term where $\alpha = \beta = 1$ and the lowest order interaction term scales as $\frac{1}{R^3} \langle n_a l_a | r | n'_a l'_a \rangle \langle n_b l_b | r | n'_b l'_b \rangle$. We find that the diagonal matrix elements are zero and that the non-diagonal matrix elements are given by:

$$\begin{aligned} \langle j | V_{int} | k \rangle &= -\frac{2}{3} \frac{\mu^2}{R^3} & m = 0 \\ \langle j | V_{int} | k \rangle &= \frac{1}{3} \frac{\mu^2}{R^3} & |m| = 1, \end{aligned}$$

where μ is the electric dipole matrix element for the $s \rightarrow p$ transition and is given by

$$\mu = e \langle s | r | p \rangle. \quad (3.10)$$

If we diagonalize the matrix we find the energy shifts ε of the states to be:

$$\begin{aligned} \varepsilon_{1,2} &= \pm \frac{2}{3} \frac{C_3}{R^3} & \Sigma \text{ state} \\ \varepsilon_{1,2} &= \pm \frac{1}{3} \frac{C_3}{R^3} & \Pi \text{ state,} \end{aligned}$$

where $C_3 = \mu^2$.

The expressions above are only valid in the region where the Hund's case (a) coupling can be applied. To extend the calculation to larger internuclear distances, the fine-structure interaction should be included. The Movre-Pichler analysis [7] is used to do this. This analysis was developed to calculate long range potentials for diatomic alkali molecules, but it can also be applied to diatomic He* molecules. Now potential curves can be calculated in the range where the dipole-dipole interaction energy is comparable to the fine-structure splitting and in the pure Hund's case (a) and Hund's case (c). We start with an atomic basis including fine-structure and then calculate the dipole-dipole interaction. The atomic basis is given by:

$$|j\rangle = |n_a(l_a s_a) j_a m_a; n_b(l_b s_b) j_b m_b\rangle, \quad (3.11)$$

where $n_{a,b}$ is the principal quantum number for the electron at atom a or b . The potentials which are calculated for the Hund's case (a) region are degenerate for

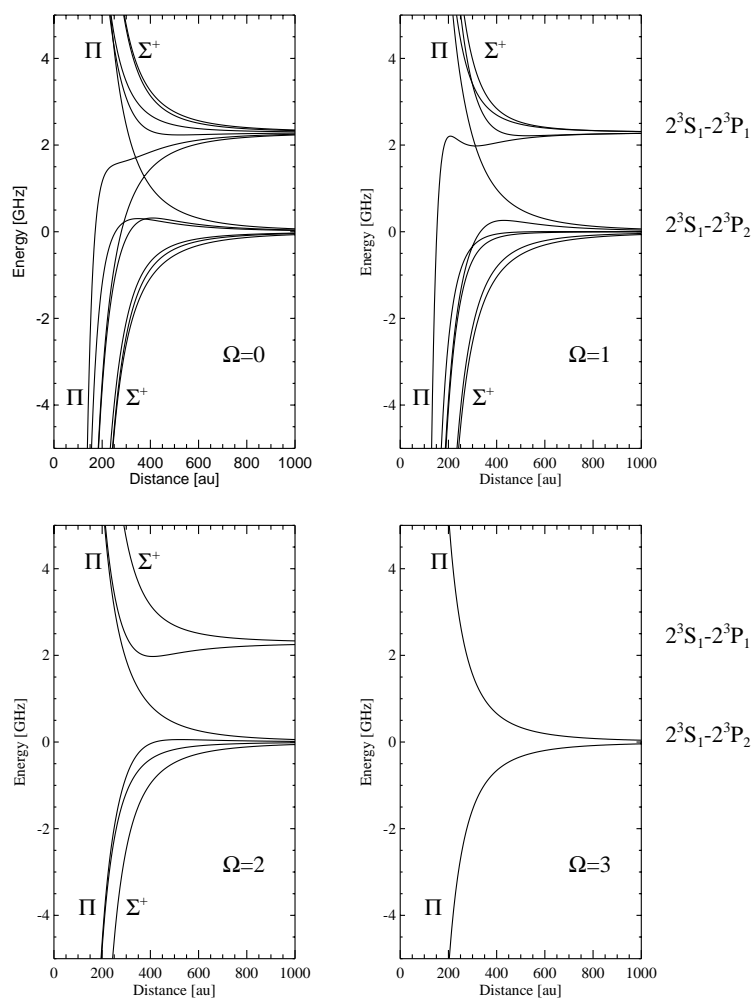


Figure 3.4 Potential curves which connect to the $2^3S_1 - 2^3P_2$ and the $2^3S_1 - 2^3P_1$ asymptotes. The attractive potential couple at short range to the $1,5\Pi_g$, the $3\Pi_u$, the $1,5\Sigma_u^+$, and the $3\Sigma_g^+$ states. For $\Omega = 3$ the attractive potential couples at short range only to the $5\Pi_g$ state. The repulsive potentials couple at short range to the $1,5\Pi_u$, the $3\Pi_g$, the $1,5\Sigma_g^+$, and the $3\Sigma_u^+$ states. For $\Omega = 3$ the repulsive potential couples at short range only to the $5\Pi_u$ state.

states with equal j . However, when fine-structure is included these states are non-degenerate. Since the interaction potential V_{int} depends on $l_{a,b}$ and not on $j_{a,b}$, the basis functions have to be expanded in terms of $|nlm^l\rangle$ for the electron at nucleus a and the electron at nucleus b :

$$|n(ls)jm\rangle = \sum_{l,m^l,s,m^s} |nlm^l; sm^s\rangle \langle lm^l; sm^s | jm\rangle. \quad (3.12)$$

When calculating the matrix elements we take into account that states with different $m_a + m_b$ do not combine. The diagonal matrix elements give the energies of the potentials. The coupling between the potentials is important in the region where the fine structure splitting is comparable to the depth of the potential. All potential curves which are connected to the $2^3S_1 - 2^3P_{1,2}$ asymptotes and which are calculated with the above described method are shown in Fig. 3.4. Note that the rotation of the molecule is not included in the calculation given above.

The basis functions which are introduced in Sec. 3.3.3 are no eigenfunctions for the long range. In this range $\Omega = |m_a + m_b|$ is a conserved quantity. The eigenfunctions for this region are constructed using the correct basis functions, shown in Eq. 3.11. The eigenfunctions are labeled with Ω as was shown in Sec. 3.2.2. We find 7 basis functions for $\Omega = 0$, 6 for $\Omega = 1$, 3 for $\Omega = 2$ and 1 for $\Omega = 3$. The basis functions are used to create eigenfunctions with the correct symmetry properties. The states can have either *gerade* or *ungerade* symmetry, so there are 2×7 ($0_{g,u}$) states. The states with $\Omega \neq 0$ are doubly degenerate and therefore there are $2 \times 2 \times [6 (1_{g,u}) + 3 (2_{g,u}) + 1 (3_{g,u})]$ states. In total there are 54 Hund's case (c) states so the total number of states is conserved as it should be.

3.5 The behavior of the long-range potentials

As is discussed in previous sections, several ranges of internuclear distances can be distinguished where different molecular coupling cases apply. These regions are schematically shown in Fig. 3.5. In Sec. 3.4 potential curves have been calculated for internuclear distances in the regions II, III, and IV. In the regions II and IV, where Hund's case (a) and (c) respectively can be applied, the interaction is a pure C_3/R^3 interaction, as was shown in Sec. 3.4. In the region indicated by III the behavior of the potential curves deviates from this C_3/R^3 interaction. This deviation results from the mixing of states due to the fine-structure interaction and is important in the range where the dipole-dipole interaction energy is comparable

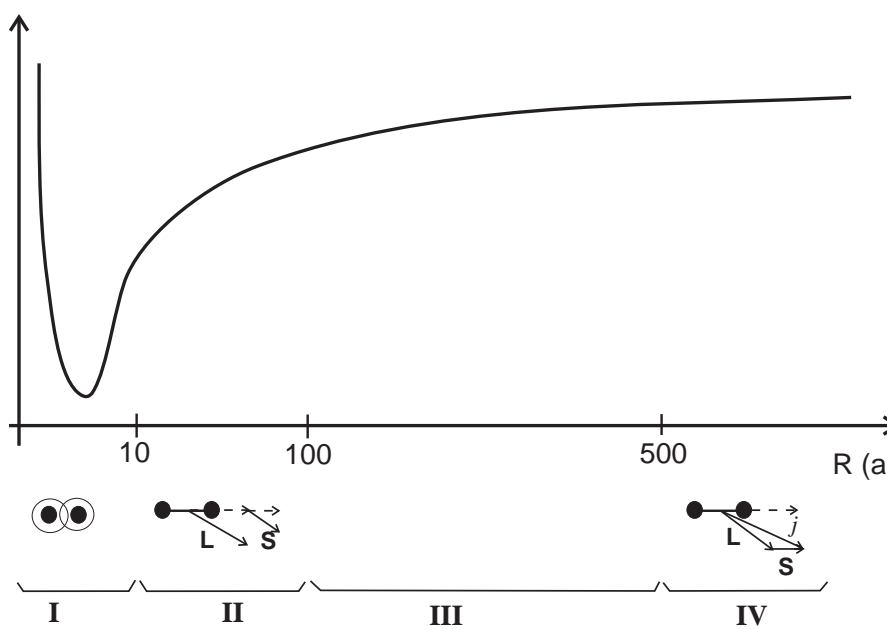


Figure 3.5 A potential energy curve is plotted as a function of the internuclear distance R . Below the x -axis several regions are shown. Region I is the region where the electronic wavefunctions of the atoms overlap. In this region chemical interactions are dominant. In region II the electronic motion is strongly coupled to the internuclear axis. In both regions I and II Hund's case (a) coupling can be applied. Region III is an intermediate region, where neither Hund's case (a) nor Hund's case (c) apply. In region IV the spin-orbit coupling is larger than the coupling to the internuclear axis and the molecule is described by Hund's case (c). On the x -axis we have indicated the order of magnitude of the distances R where the regions begin.

to the fine structure interaction. At these ranges the eigenstates are described with Hund's case (c) states. The Hund's case (c) states are linear combinations of the Hund's case (a) states that describe the molecule at short internuclear distances. As a result of the coupling the linear combinations vary with the internuclear distance.

We have projected the Hund's case (c) states on the Hund's case (a) states. As an example the projection of a 2_u state on the Hund's case (a) states is plotted in Fig. 3.6a. It can be seen that the linear combination of Hund's case (a) states

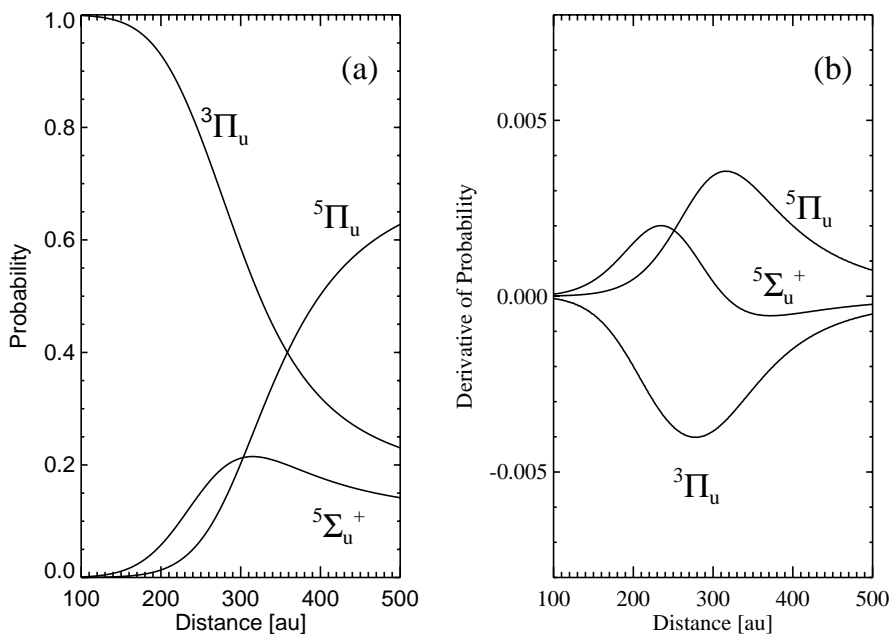


Figure 3.6 In part (a) the projection of the 2_u state on Hund's case (a) states is shown as a function of the internuclear distance. In part (b) the derivative of the projection on these states is shown as a function of the internuclear distance.

changes completely with the internuclear distance.

In Fig. 3.6b the spatial derivative of the projection of this 2_u state is shown. The spatial derivative is a measure for coupling with other states which have the same symmetry. The coupling is strongest in the region between 280 and 320 a_0 , but it is still effective in the whole region from 100 to 500 a_0 .

3.5.1 Purely long-range potentials

States with identical symmetries are not allowed to cross due to the von Neumann-Wigner non-crossing rule. As a result of these avoided crossings there are potentials which are attractive at very long range, in region IV, and become repulsive at shorter internuclear distances, in region III. These potentials are denoted as purely

Table 3.1 List of purely long-range potentials and some of their properties.

symmetry	asymptote	E_{min} (GHz)	r_{min} (a_0)	r_{inner} (a_0)
0_u^-	$2^3S_1 - 2^3P_1$	-0.0565	524	419
0_u^+	$2^3S_1 - 2^3P_0$	-2.124	188	146
1_g	$2^3S_1 - 2^3P_1$	-0.320	313	100
1_g	$2^3S_1 - 2^3P_1$	-0.0756	528	424
1_g	$2^3S_1 - 2^3P_0$	-0.427	256	205
2_u	$2^3S_1 - 2^3P_1$	-0.317	408	315

long-range potentials. They have been proposed for the first time by Stwalley *et al.* [8]. We can find these purely long-range potentials by calculating the potentials with the method described in Sec. 3.4. The inner turning points of vibrational states in these potentials are extremely large, in the order of a few times $100 a_0$. In Tab. 3.1 a list of the purely long-range potentials of He_2^* , that are connected to the $2^3S_1 - 2^3P_{0,1,2}$ asymptote, is given and some of their properties are shown.

In Fig. 3.7 the purely long-range potentials connected to the $2^3S_1 - 2^3P_1$ asymptote and the ones connected to the $2^3S_1 - 2^3P_0$ asymptote are shown. From the figure it is clear that all potentials have very large inner turning points. One of the 1_g potentials that is connected to the $2^3S_1 - 2^3P_1$ asymptote has a very special double well structure. In a photoassociation spectroscopy experiment using cold Cs atoms a double well structure was responsible for a rather efficient spontaneous emission to cold ground state molecules [9].

We have calculated whether the purely long-range potentials support bound states. We have found positions of bound states for all 6 potentials. The positions of these bound states depend solely on atomic parameters and therefore the calculation can be done very accurately.

3.5.2 Lifetimes of the molecular states

The lifetimes of the long-range molecular states depend on their symmetry. The lifetimes of the Σ and Π Hund's case (a) states can easily be calculated. The states that are excited by an allowed transition have a linewidth Γ_{mol} of twice the atomic linewidth, *i.e.* $\Gamma_{mol} = 2\Gamma_{atom}$, while the states that are excited by a non-allowed transition are very stable and have a linewidth of $\Gamma_{mol} = 0$ [10]. This is only true

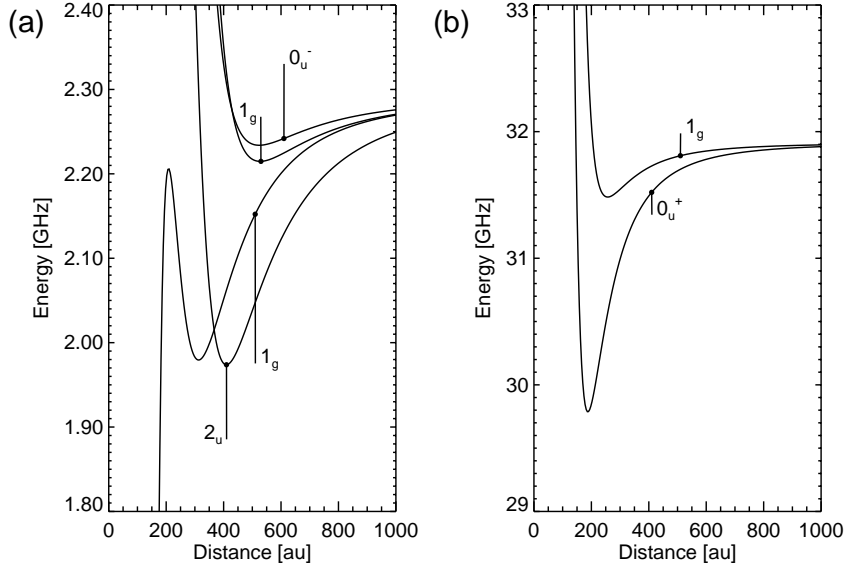


Figure 3.7 The purely long-range potentials connected to the $2^3S_1 - 2^3P_1$ asymptote are shown in part (a). The purely long-range potentials connected to the $2^3S_1 - 2^3P_0$ asymptote are shown in part (b).

for internuclear distances $R \ll \lambda = \lambda/2\pi$, where λ is the wavelength of the light. The dipole selection rules can be found in Ref. [3] and are *e.g.*

$$\Delta S = 0, \quad \Delta \Omega = 0, \pm 1, \quad g \leftrightarrow u, \quad g \leftrightarrow g, \quad u \leftrightarrow u. \quad (3.13)$$

This means that:

$$\begin{aligned} {}^{1,5}\Sigma_u^+, {}^3\Sigma_g^+, {}^{1,5}\Pi_u, {}^3\Pi_g &\rightarrow \Gamma_{mol} = 2\Gamma_{atom} \\ {}^{1,5}\Sigma_g^+, {}^3\Sigma_u^+, {}^{1,5}\Pi_g, {}^3\Pi_u &\rightarrow \Gamma_{mol} = 0 \end{aligned}$$

At long distance (in the regions III and IV) the states are superpositions of the Hund's case (a) states and their lifetime ($1/\Gamma_{mol}$) depends on the superposition. Since the linear combination of Hund's case (a) states depends on the internuclear distance R , the molecular lifetimes also depend on R . This can be seen in Fig. 3.8, where the lifetimes of various states are shown. In the figure can be seen that at

short internuclear distances the linewidths converge to either $\Gamma_{mol} = 2\Gamma_{atom}$ or $\Gamma_{mol} = 0$. Furthermore, the molecular lifetimes are also affected by retardation effects. This effect plays a role when the internuclear distance R becomes of the order of λ [11]. In Fig. 3.8 we can see that there is hardly any difference between the calculation where retardation has been neglected (the dashed line) and the calculation where retardation has been taken into account (the solid line), in the region that is relevant for the experiments. Only at internuclear distances larger than $R = 1000a_0$ retardation effects start to play a role.

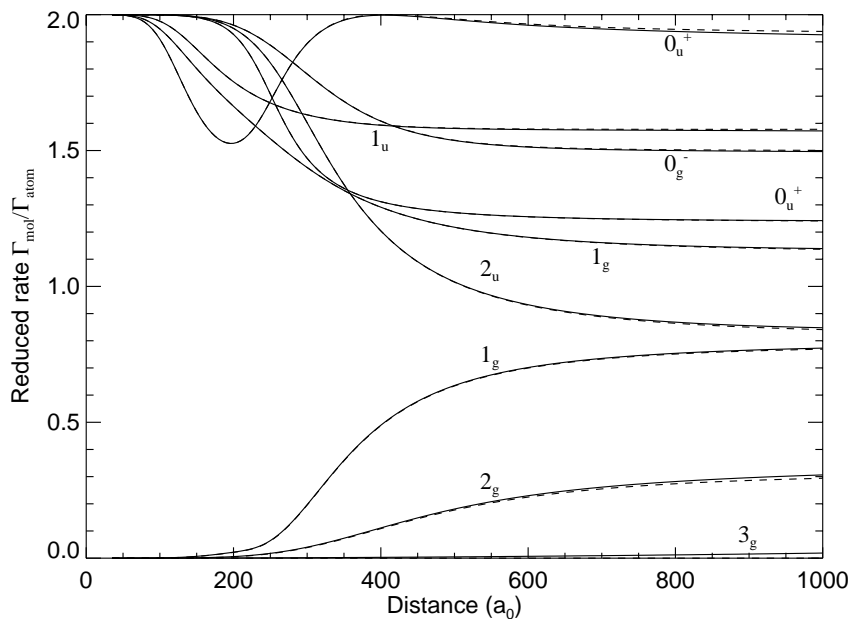


Figure 3.8 The molecular linewidth Γ_{mol} is plotted as a function of the internuclear distance for the potential curves that connect to the $2^3S_1 - 2^3P_2$ asymptote. The molecular linewidth is plotted in terms of the atomic linewidth Γ_{atom} . The dashed line is the calculation where retardation effects have not been taken into account, while the solid line does take retardation into account.

3.6 Partial waves

A collision of two structureless particles can be described by potential scattering. A central potential $V_{int}(R)$, where R is the internuclear distance, describes the interaction between the particles. The incoming wavefunction of the colliding particles can be expanded in partial waves, which have a well defined rotational angular momentum ℓ . The Schrödinger equation is then given by:

$$\left[-\frac{\hbar^2}{2\mu} \nabla^2 + \frac{\hbar^2 \ell(\ell+1)}{2\mu R^2} + V_{int} \right] \Psi = E \Psi \quad (3.14)$$

where μ is the reduced mass, ℓ is the mechanical rotational angular momentum, R is the internuclear distance, V_{int} is the interaction potential, and E is the total energy. The second term on the left side of the equation is responsible for the rotational barrier. In collisions of cold atoms, only a few partial waves can penetrate

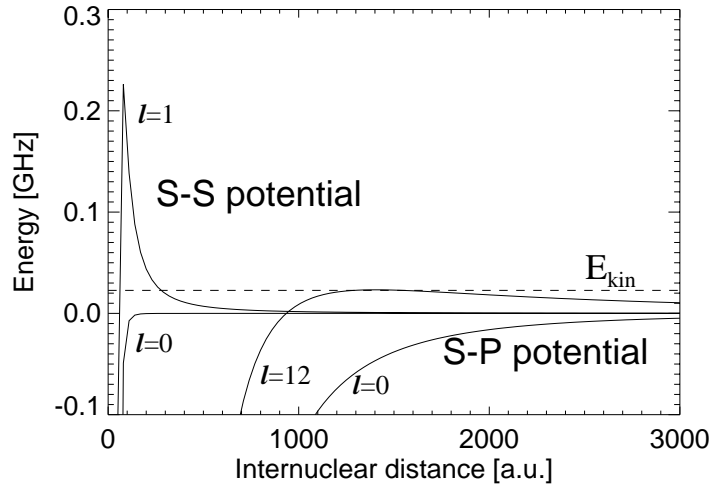


Figure 3.9 Plot of the S-S potential and the S-P potential, including the rotational barrier for various partial waves, denoted with ℓ . The asymptotic energies of the S-S potentials and the S-P potential are both set to 0. The dashed line represents the kinetic energy of the atoms, which corresponds to a temperature of 1 mK.

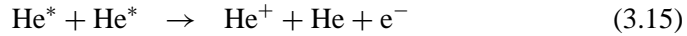
the rotational barrier and reach small internuclear distances.

The S-S potential is a Van der Waals interaction, which behaves as C_6/R^6 and is therefore small at large distances. In Fig. 3.9 the S-S potential is plotted using the actual C_6 coefficient. It can be seen that if the temperature of the colliding atoms is 1 mK, only s-waves can reach small internuclear distances. As is discussed in Sec. 3.4 the S-P potential goes as C_3/R^3 . This potential is much less flat than the C_6/R^6 potential. This S-P potential is also plotted in Fig. 3.9, using $C_3 = 10$ a.u. It can be seen that partial waves up to $\ell = 12$ can penetrate the rotational barrier and reach small internuclear distances. The number of partial waves that can be excited from the S-S potential to the S-P potential depends on the internuclear distance where the excitation has been made. When R decreases the number of partial waves that can reach R on the S-S potential decreases, because of the rotational barrier. Partial waves with $\ell \neq 0$ can reach an internuclear distance of the order of minimally a few $100 a_0$ on the S-S potential.

3.7 Penning Ionization

The He^* atom has a high internal energy. In this respect the metastable rare gas atoms differ from ground state atoms. Due to this high internal energy He^* atoms are not stable in close collisions with He^* atoms or other atoms. We will just consider close collisions between He^* atoms.

In a close collision of two He^* atoms, the system can spontaneously ionize.



The process shown in Eq. 3.15 is called Penning ionization (PI) and the process shown in Eq. 3.16 is called associative ionization (AI). For PI the relative kinetic energy is sufficient for dissociation to take place into an ion and an atom in the ground state. However, for AI the energy difference between the initial and the final state is smaller than the energy of two free atomic particles. The particles will remain bound and form molecular ions. Since we cannot distinguish between PI and AI in the experiments, both Penning ionization and associative ionization will be denoted as PI in the rest of the thesis. An extensive description of PI is given in Ref. [12]. Here it will only be discussed briefly.

In Fig. 3.10 a schematic picture of PI is shown. Since the Born-Oppenheimer approximation is used, the position of the nuclei does not change during the transition to the ionizing curve V^+ . The ionization process is possible if for some

distances the potential of the two colliding He* atoms, V^* , is in the continuum of the ionizing potential V^+ . In that case the colliding atoms spontaneously ionize. Ionization can be included in calculations using a complex potential:

$$\bar{V}^*(R) = V^*(R) - i\Gamma(R)/2, \quad (3.17)$$

where $\Gamma(R)$ is the total electronic transition rate for a transition from $V^*(R)$ to $V^+(R)$.

On the He $2^3S_1 - 2^3S_1$ potential, the PI probability for close collisions in the $1^1\Sigma_g^+$ and $3^3\Sigma_u^+$ state is almost unity at internuclear distances of a few a_0 . Due to the

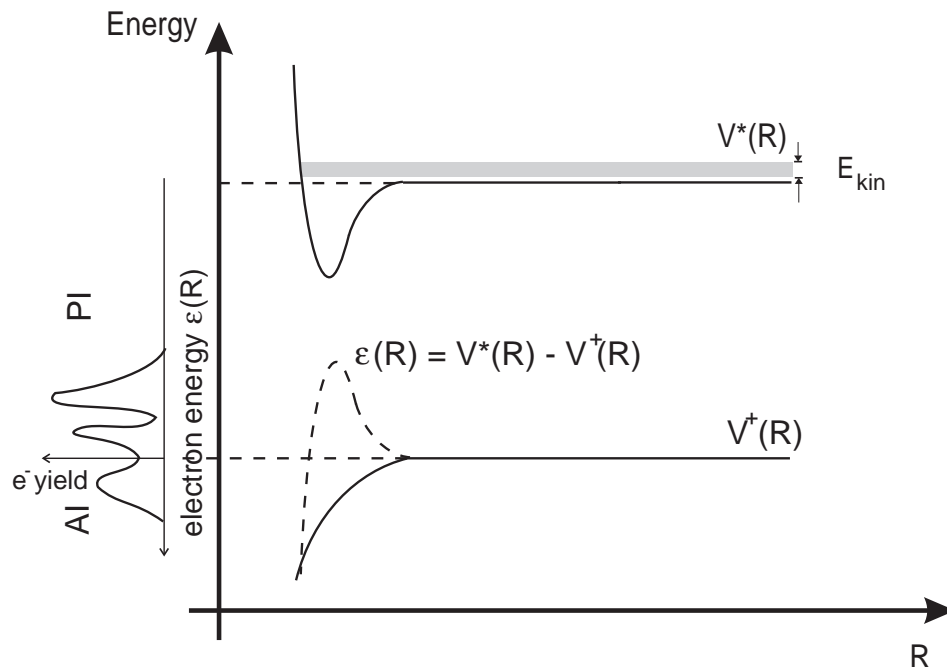


Figure 3.10 Schematic representation of PI and AI. $V^*(R)$ is the potential curve of the colliding metastable atoms and $V^+(R)$ is the potential curve describing the ionized system. The energy of the emitted electron at a certain distance R_c , $\varepsilon(R_c)$, is the difference between $V^*(R_c)$ and $V^+(R_c)$. At the energy axis an electron energy spectrum is shown, with at the high energy side the electrons leading to AI and at lower energies the electrons leading to PI.

spin conservation rule PI is spin-forbidden for close collisions in the $^5\Sigma_g^+$ state. The ionization probabilities for close collisions on the He $2^3S_1 - 2^3P_{0,1,2}$ potential have similar behavior.

References

- [1] P. D. Lett, P. S. Julienne, and W. D. Phillips, *Ann. Rev. Phys. Chem.* **46**, 423 (1995).
- [2] W. C. Stwalley and H. Wang, *J. Mol. Spectrosc.* **195**, 194 (1999).
- [3] G. Herzberg, *Spectra of Diatomic Molecules*, Van Nostrand, New York, (1950).
- [4] R. Zare, *Angular Momentum: Understanding Spatial Aspects in Chemistry and Physics*, Wiley, New York, (1988).
- [5] P. van der Straten, private communication.
- [6] M.E. Rose, *J. Math. Phys.* **37**, 215 (1958).
- [7] M. Movre and G. Pichler, *J. Phys. B* **10**, 2631 (1977).
- [8] W. C. Stwalley, Y.-H. Uang, and G. Pichler, *Phys. Rev. Lett.* **41**, 1164 (1978).
- [9] A. Fioretti, D. Comparat, A. Crubellier, O. Dulieu, F. Masnou-Seeuws, and P. Pillet, *Phys. Rev. Lett.* **80**, 4402 (1998).
- [10] M. J. Stephen, *J. Chem. Phys.* **40**, 669 (1964).
- [11] W.J. Meath, *J. Chem. Phys.* **48**, 227 (1968).
- [12] A. Niehaus, *Adv. Chem. Phys.* **45**, 399 (1981).

Chapter 4

Photoassociation Spectroscopy of He*

4.1 Introduction

Photoassociation spectroscopy (PAS) of cold atoms is an important tool to study long-range interactions. Numerous photoassociation experiments have been done with alkali atoms providing detailed information on ground and excited state potentials [1, 2]. From this information *e.g.* the ground state scattering length and the radiative lifetime can be determined [3–5]. Since the technique has proven to be so powerful in the study of alkali atoms, it is very interesting to apply it to metastable rare gasses as well.

PAS is done by making a free-bound transition from the ground to the excited state. This is shown schematically in Fig. 4.1. In the figure only one potential, connected to S+P asymptote, is shown, while there are several potentials in reality. The transition is made at the internuclear distance R_c where the Franck-Condon overlap between the ground state wavefunction and the excited state wavefunction is the largest. The atoms in the magneto-optical trap are ultra-cold, which means that the wavefunction of the free atoms in the S+S potential is slowly varying as a function of the internuclear distance. Therefore the overlap with vibrational states in the S+P potential is largest at the classical outer turning points. The probe laser is scanned in frequency and when its frequency is resonant with an excited bound vibrational state, population can be transferred to this state and a resonance can be observed. PAS is only possible with ultra-cold colliding atoms, since the Franck-Condon overlap needs to be the largest at the outer turning point of the excited vibrational states, which is only possible if the ground state wavefunction varies slowly enough.

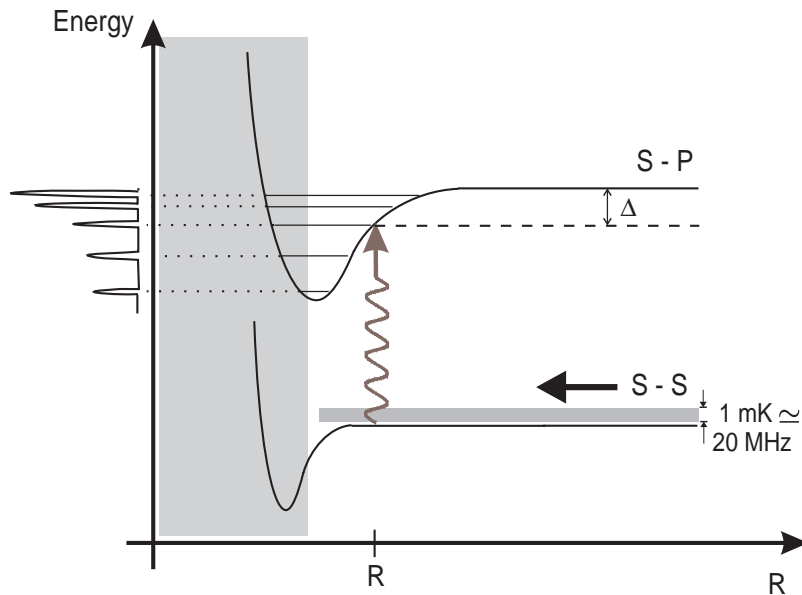


Figure 4.1 Principle of PAS. The S+P potential is scanned with a probe laser. When the laser is resonant with a vibrational state energy, population is transferred from the free system in the S+S potential to a bound state in the S+P potential. The shaded region at small internuclear distances shows the region where Penning ionization plays a role. Δ is the detuning of the probe laser with respect to the atomic resonance. The kinetic energy spread due to the temperature of the trapped atoms is indicated by the shaded region on top of the S+S potential. Note that the energy and the internuclear distance R have not been drawn at the right scale.

In PAS experiments with alkali atoms two methods are used to detect the excitation of bound states. A very straightforward method is to do a trap loss experiment as was done by McAlexander *et al.* [4]. They measured the fluorescence emitted by the trapped atoms, where the excitation to a bound state is detected as a dip in the fluorescence signal. Another method is to make an additional excitation from the excited bound state to an ionizing state and to measure the ion rate, as was done by Molenaar *et al.* [6].

One aspect in which metastable rare gas atoms differ from alkali atoms is that they ionize at small internuclear distances, of a few a_0 , by Penning ionization.

For He (2^3S_1) atoms colliding in the ground state the ionization probability for the $^1\Sigma_g^+$ and the $^3\Sigma_u^+$ states is almost unity at these small distances. Ionization is spin-forbidden for the $^5\Sigma_g^+$ state and thus suppressed with a factor of 10^5 [7]. It is expected that the ionization probabilities for a molecule in the $2^2S_1 - 2^3P_{0,1,2}$ potential have similar behavior at small internuclear distances. At long range the pure singlet, triplet and quintet states mix due to the fine structure interaction. The large ionization probabilities at short range combined with the mixing of states at long range make it not trivial to predict the effects of PAS in the He $2^2S_1 - 2^3P$ system.

Until recently [8] there had been done no PAS measurements of the He* system. In this chapter exploratory PAS measurements of ultra-cold He₂* will be discussed for potentials connected to the He $2^3S_1 - 2^3P_2$ asymptote. In Sec. 4.2 the experimental method will be described. In Sec. 4.3 we will show measured spectra and we will investigate several features of the spectra, such as the dependence on the intensity of the probe laser. In Sec. 4.4 an analysis of the measured spectra will be given. Series of peaks, observed in the spectra, will be assigned to states connected to the $2^3S_1 - 2^3P_2$ asymptote. Furthermore a description of the mechanism, which is responsible for the ion production when a bound state is excited, will be given in Sec. 4.4.4.

4.2 Experiments

The experiments have been done in a magneto-optical trap (MOT). The trap is loaded with a beam of He* atoms that is produced in a DC-discharge source which is cooled with liquid helium. The mean velocity of the atoms leaving the source is 300 m/s. Before the He* atoms are trapped in the MOT they are Zeeman slowed with a counter-propagating laser beam while the required Zeeman shift is produced by the magnetic field of the MOT coils. Typically we trap 10^6 atoms with a temperature of 1 mK and a density of a few times 10^9 cm⁻³. The atoms are cooled on the $2^3S_1 \rightarrow 2^3P_2$ transition, which has a wavelength of 1083 nm.

As is shown in Fig. 4.1 a probe laser scans the vibrational states connected to the $2^3S_1 - 2^3P_2$ asymptote. An increase in the ionization rate is a signature of a bound state. The produced ions are measured with micro-channel plates (MCPs). The mechanism for the increase in ionization rate is explained in Sec. 4.4.4.

In Fig. 4.2 a picture of the experimental setup is shown with the trapping beams and the probe beam. The laser light is generated by diode lasers. The frequency of the probe laser light is calibrated using a Fabry-Perot interferometer for

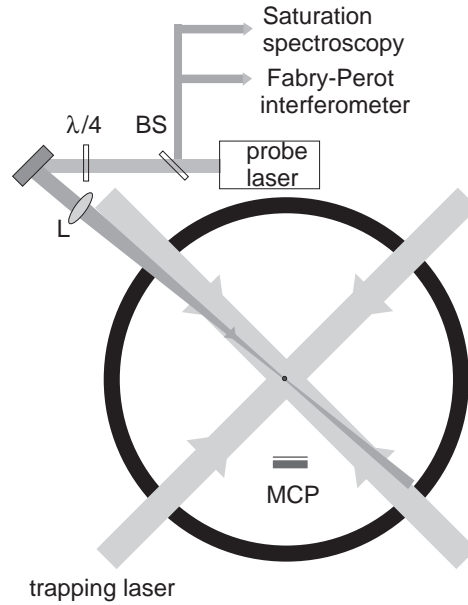


Figure 4.2 Probe laser setup. M stands for mirror, $\lambda/4$ for quarter wave retardation plate, L for lens, BS for 5% beam splitter, and MCP for micro-channel plates.

the relative frequency scale and the Lamb dip to determine the absolute frequency. The position of the Lamb dip is measured in a saturated absorption spectroscopy setup as discussed in Sec. 2.5. The uncertainty in the absolute frequency scale is 20 MHz.

The trapping laser operates close to the $2^3S_1 - 2^3P_2$ asymptote at a detuning of -12.5Γ . Since the rate constant for PI is a factor of 100 larger for collisions in the $2^3S_1 - 2^3P_2$ potential than for collisions in the $2^3S_1 - 2^3S_1$ potential, the trapping laser induces a large number of ions [9]. To avoid this huge background ionization signal the trapping laser is periodically switched off during measurements with a duty cycle of 50%, by detuning its frequency 500 MHz to the red of the $2^3S_1 \rightarrow 2^3P_2$ transition. This is far enough to ensure that the laser light does not induce many ions. The modulating frequency is chosen to be 25 KHz. This is fast enough to avoid a significant expansion of the cloud of trapped atoms in the period when the trapping laser is switched off. The ion signal is gated and can be measured both in the period when the trapping laser is far detuned, which will be called

the probing period and in the period when the trapping laser is at its operating frequency, which will be called the trapping period. In the probing period the resonances are measured, while the signal in the trapping period is used to monitor the stability of the trapped cloud. The probe laser is on continuously. A typical scan time is 100 s.

4.3 Results

In Fig. 4.3 a typical spectrum is shown. The saturation parameter of the probe laser is $s_0 = 10^4$. Several scans are added together to produce the spectrum. The noise in the spectrum is filtered out using a least-squared spline approximation, developed by Thijsse *et al.* [10]. We have made sure that no structure has been added to the spectrum by this algorithm and that only noise is filtered out. In the spectrum distinct peaks can be observed, with increasing distances between neighboring peaks when the detuning Δ from the atomic resonance increases. When the frequency of the probe laser is close to the atomic resonance the cloud of trapped atoms is disturbed by the laser, which is on continuously, and the trap can be emptied completely. In Fig. 4.3 the dashed line indicates the detuning where the probe laser starts to disturb the trap.

We have measured photoassociation spectra as a function of the probe laser intensity. In Fig. 4.4 a number of spectra is shown which have been measured with increasing probe laser intensities. The intensities range from $s_0 = 50$ to $s_0 = 10^5$. The figure shows that, when the laser intensity increases, ionization peaks start to appear at increasing detunings and that the heights of the peaks grow. Deeply bound states can only be measured with high probe laser intensities. The bound states which lie close to the dissociation limit are measured with low intensities since a high intensity probe laser would disturb the cloud of atoms in the frequency region of interest. In the experiments intensities up to $s_0 = 2 \cdot 10^5$ have been used. We have measured peaks at detunings of up to -20 GHz. Peaks corresponding to the most deeply states that are measured can only be observed with the highest laser intensities.

We have analyzed the line shapes of the peaks in order to determine the width as a function of the intensity of the probe laser, for all peaks. Since we expect the width to be mostly determined by the temperature of the atoms in the MOT, the ion peaks in the spectra have been fitted with Gaussian line shapes. The resolution of the measurements is not good enough to analyze the line shape of the peaks as was done by Napolitano *et al.* [11] who studied relative contributions of different

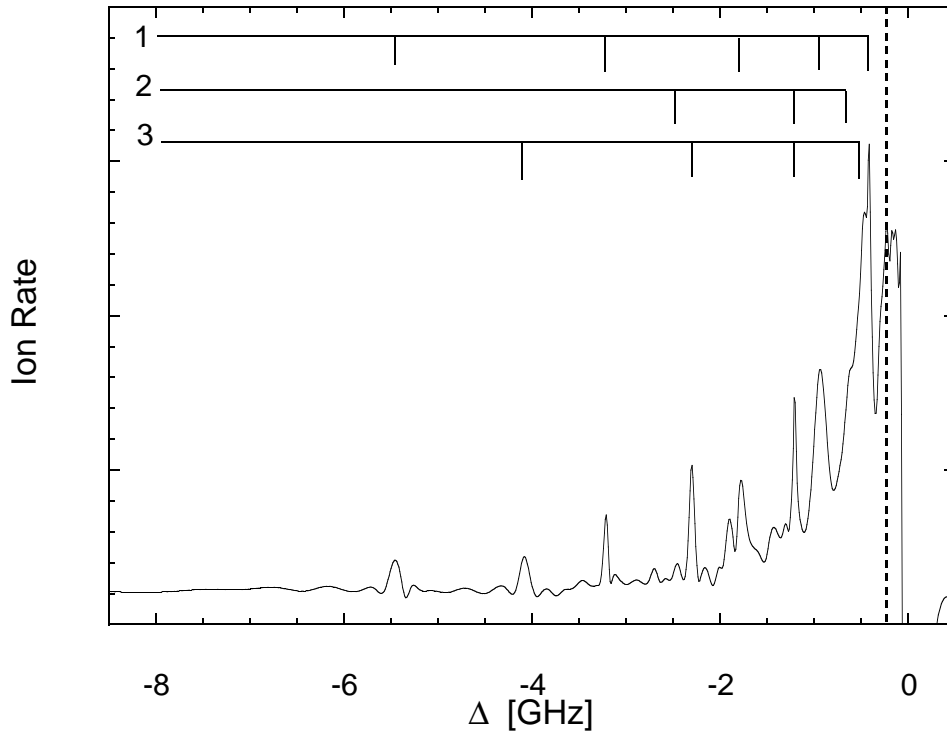


Figure 4.3 Photoassociation spectrum as a function of the detuning Δ of the probe laser. The noise in the spectrum is filtered out. The saturation parameter of the probe laser $s_0 = 10^4$. The assignment of the states to series of vibrational states is shown on top. The dashed line indicates the detuning where the probe laser starts to disturb the MOT.

partial waves and obtained detailed information on the ground state potential. We do not expect to measure contributions from different partial waves either since for states, which are more deeply bound than -2 GHz, only s-waves can penetrate the potential barrier of the He $2^3S_1 - 2^3S_1$ potential and reach the outer turning points. However, the highest lying vibrational states have extremely large outer turning points and there several partial waves can contribute. In the spectra it can be seen when the contribution of partial waves with $\ell \neq 0$ starts to be important. In this regime we observe ion peaks superposed on a continuous increase of the ionization rate, which is explained by the contribution of partial waves with angu-

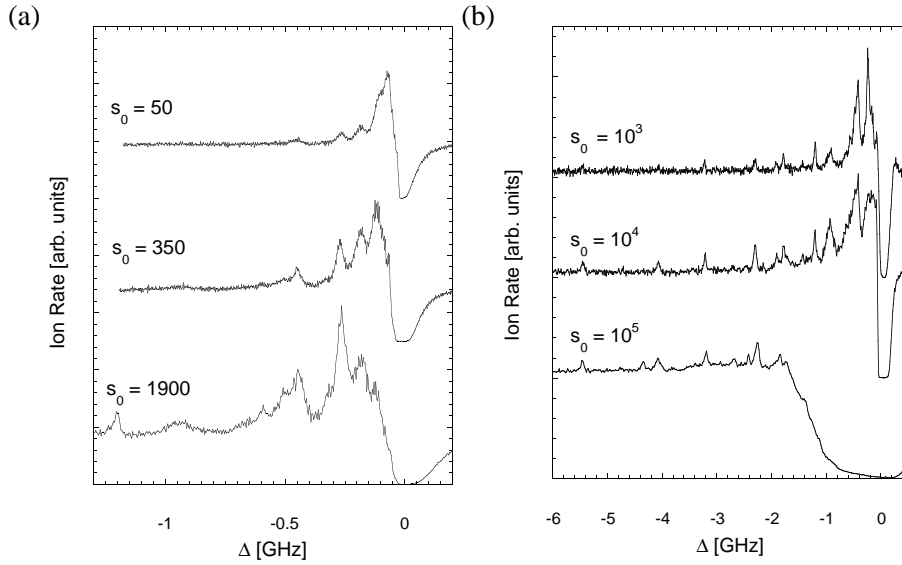


Figure 4.4 Spectra measured with increasing probe laser intensities. The saturation parameter s_0 is shown above the corresponding spectrum.

lar momenta up to $\ell = 12$ [9]. In this region the peaks are too close to each other to be able to analyze the line shapes.

We have determined the peak widths as a function of the probe laser intensity. Some of the peaks are too small to fit or have too much overlap with neighboring peaks. Therefore it is not possible to make an accurate estimate of the width for all peaks at all probe laser intensities. In Fig. 4.5 the widths of several peaks are plotted as a function of the laser intensity. It can be seen that they are slightly broadened with increasing power. The average width at low laser intensities, *i.e.* in cases where the width is least power broadened, is 30 ± 10 MHz. The temperature of the trapped atoms is 1 mK, which corresponds to a frequency of 20 MHz. So the actual width is in the order of the thermal width for low laser intensities and slightly power broadened at higher intensities. The majority of the peaks has identical widths. However, one of the measured peaks, the one at a detuning of -0.93 GHz, has a much larger width of 70 MHz. Probably two or more peaks overlap at this position and the resolution of the measurement is not good enough to separate them.

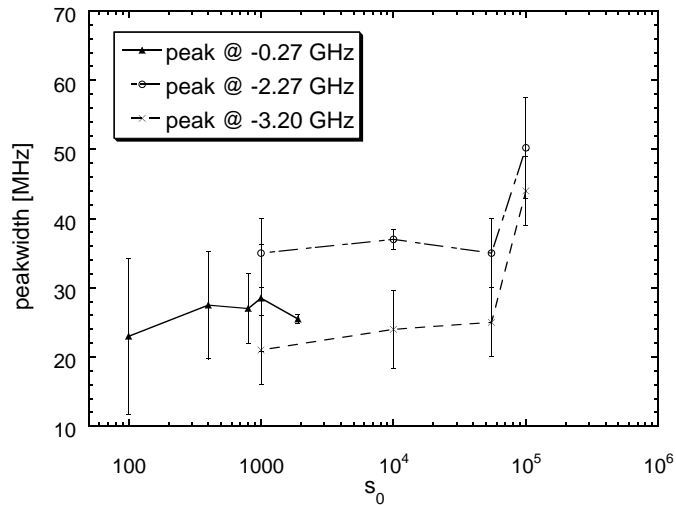


Figure 4.5 Peak widths (in MHz) as a function of the probe laser intensity. The lines have been drawn to guide the eye.

In all measurements discussed above the probe laser was circularly polarized. In Fig. 4.6 two spectra are shown that are measured under similar conditions, but with a linearly polarized probe laser beam and a circularly polarized probe laser. The dashed line shows the measurement where the laser light is circularly polarized. The measurement that is plotted with the solid line is taken with the probe laser light linearly polarized. There are no significant differences between the two spectra. The peaks appear at the same positions and their heights and widths have the same magnitude. It is not surprising that this is the case. The spins of the atoms in a MOT are randomly oriented due to the combination of the inhomogeneous magnetic field and the fact that atoms are pumped by the six trapping laser beams which have opposite circular polarizations. Therefore the polarization of the probe laser light is not in a well defined direction with respect to the collision axis and hence it should not influence the photoassociation spectrum. The atoms in the trap would have to be spin polarized in order to measure the effect of the polarization of the light.

There is no rotational structure visible in the spectra. It is not clear why this would be the case. Because of the height of the potential barrier, close collisions

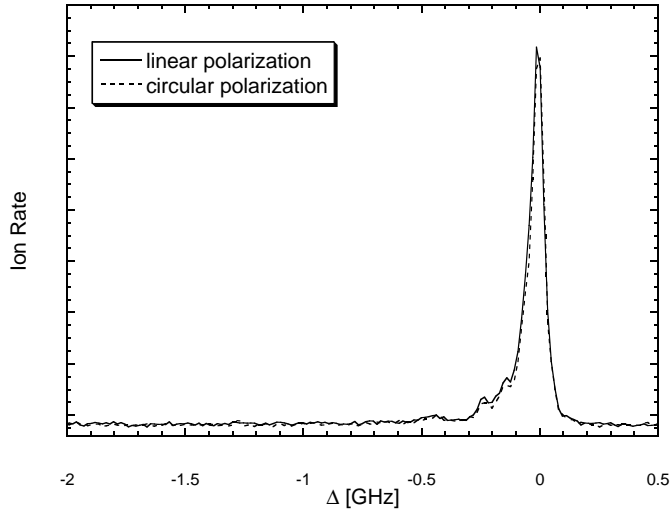


Figure 4.6 Spectrum taken with linear and circular probe laser polarizations.

in the ground state can only occur with s-waves ($\ell = 0$). However, transitions with $\Delta J = 0, \pm 1$ with $J = 0 \rightarrow J' = 0$ are allowed. In the $2^3S_1 - 2^3S_1$ state there are states which have angular momenta of $J = 0$ and $J = 2$. Therefore it should be possible to observe rotational structure with angular momenta up to $J = 3$ in the spectra.

4.4 Analysis

In Tab. 4.1 an overview is given of all measured peaks. We have analyzed the peak positions in order to assign the peaks to the long-range potentials. The long-range potentials have been calculated using the Movre-Pichler method [12], as is described in Sec. 3.4. For the He $2^3S_1 - 2^3P_{0,1,2}$ system there are in total 54 states. Some of these are degenerate, so we have to consider 34 non-degenerate states. The long-range potentials are shown in Fig. 4.7. Nine of these potentials are both attractive and connect to the He $2^3S_1 - 2^3P_2$ asymptote.

Since the spacing between the subsequent peaks in the measured spectra is not regular, it is clear that the spectrum should consist of several series of vibrational states. In alkali systems states with different symmetries have different hyperfine

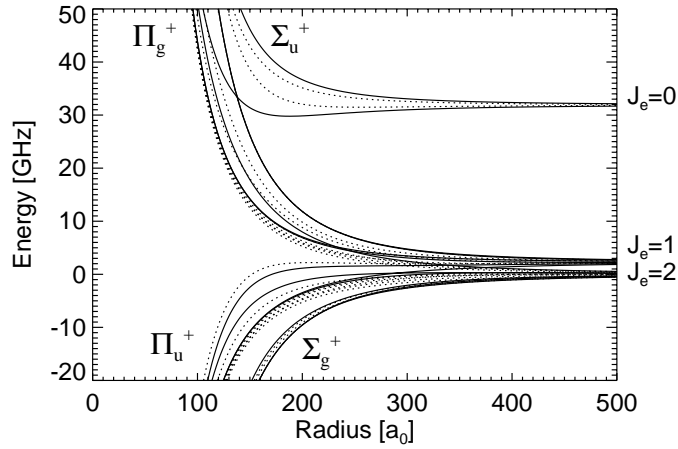


Figure 4.7 Long-range potential curves for Hund's case (c) states connected to the 2^3S_1 - $2^3P_{0,1,2}$ asymptotes.

splittings. Therefore the widths of the photoassociation resonances can be used to assign a series of resonances to a state with a particular symmetry [13]. However, in the He^* system there is no hyperfine splitting and we cannot use the widths of

Table 4.1 Detunings Δ of the probe laser from the 2^3P_2 atomic resonance at which photoassociation peaks have been observed. If possible an assignment of the peaks to a particular series has been made. The positions of the very weak peaks are given in parentheses.

n	$-\Delta$ (GHz)	ser.	n	$-\Delta$ (GHz)	ser.	n	$-\Delta$ (GHz)	ser.
1	0.11	2	9	1.77	1	17	6.85	3
2	0.19	-	10	1.91	-	18	7.26	2
3	0.27	2	11	2.27	3	19	8.80	1
4	0.45	1	12	2.43	2	(20)	10.73	3
5	0.50	3	13	3.20	1	(21)	11.43	2
6	0.59	2	14	4.07	3	22	13.67	1
7	0.93	1	15	4.32	2	(23)	20.11	-
8	1.20	2,3	16	5.45	1	(24)	21.01	-

the peaks to distinguish between levels from states with different symmetries. As was shown in Sec. 4.3 the peak widths are indeed identical for almost all peaks. This makes the assignment of the peaks to particular series more difficult. The only information that is available is the position of the peaks and the height of the peaks. It is not straightforward to use the height of the peaks to distinguish to identify different series, because the peak height depends on the ground state wavefunction.

Due to the mechanism which is responsible for the formation of ions when a bound state is excited, only peaks corresponding to states that are at most as deeply bound 20 GHz can be observed. This maximal depth limits the accuracy with which the peaks can be assigned to specific potentials.

4.4.1 Leroy-Bernstein fit

To start with the analysis we have used the Leroy-Bernstein (L-B) method [14] to find the various series of peaks present in the spectrum. In this approach it is assumed that the positions of the high-lying vibrational states are completely determined by the long-range part of the potential since most time is spent in the outer range of the potential. Therefore the approximation is only valid close to the dissociation limit. The long-range part of the potential has the shape $V(R) = D - C_n/R^n$, where D is the dissociation limit and n is the power of the long-range potential. The interaction on the S-P potential is a dipole-dipole interaction which corresponds to a C_3/R^3 interaction. Leroy and Bernstein deduced that the positions of the vibrational levels should then be given by

$$E_v - E_d = \frac{1}{C_3^2} \left(\frac{\hbar}{2} \sqrt{\frac{2\pi}{\mu}} \frac{\Gamma(4/3)}{\Gamma(5/6)} (v - v_d) \right)^6, \quad (4.1)$$

where E_v is the energy of a vibrational level, E_d is the dissociation energy, v is the vibrational quantum number, v_d is the effective vibrational quantum number of the level at the dissociation limit, and $\Gamma(n)$ is the Gamma-function. We have compared the distances between all peaks. After analyzing them with Eq. 4.1 at least 3 series of vibrational levels were found to be present in the spectra.

In Fig. 4.8 the three series are shown, together with the fits made with the L-B formula. From the fits the C_3 coefficients for the three series follow. They are found to be -8.38, -7.62, and -8.00 a.u. for the series 1, 2, and 3 respectively that are indicated in Tab. 4.1. The dispersion coefficient μ is given by

$$\mu = e \langle s | \mathbf{r} | p \rangle, \quad (4.2)$$

which is the electric dipole matrix element of the $s \rightarrow p$ transition. The dispersion coefficient μ^2 for the $2^3S - 2^3P$ potential is 19.20 a.u. The C_3 coefficients of the states are fractions of the dispersion coefficient and the fitted C_3 coefficients have realistic values. As will be shown in Sec. 4.4.2 the fitted C_3 coefficients are average values. They cannot be used to assign the three series to particular states.

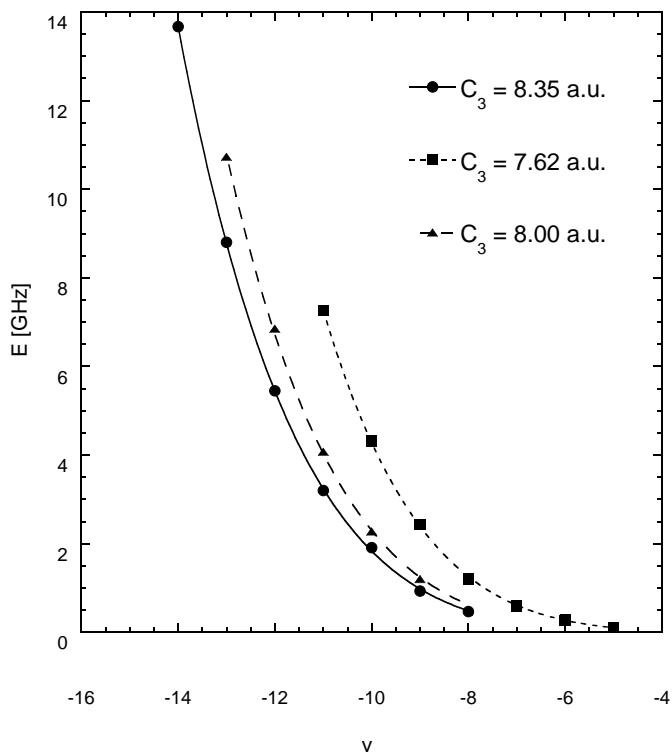


Figure 4.8 Three series of vibrational states. On the x-axis the vibrational quantum number v is plotted. The vibrational level that is closest to the dissociation limit is labeled with $v = 0$. The symbols are the measured peak positions and the lines are the Leroy-Bernstein fits, using Eq. 4.1.

4.4.2 Effective C_3 coefficient

At the long-range distances where the excitations to the bound states are made, the excited state potential does not have a pure C_3/R^3 behavior. Due to the fine structure interaction, states with identical symmetries couple at long range. At these distances the potentials are linear combinations of the Hund's case (a) states that describe the system at short range. The linear combinations vary with the internuclear distance. Therefore the potentials deviate from the C_3/R^3 behavior.

The deviation from the pure C_3/R^3 behavior of the potentials is illustrated in Fig. 4.9. In this figure the effective C_3 coefficient is plotted as a function of the internuclear distance R for all attractive curves which connect to the $2^1S_1 - 2^3P_2$ asymptote. This coefficient is found by $C_3^{eff}(R) \equiv V(R) \times R^3$. We can see

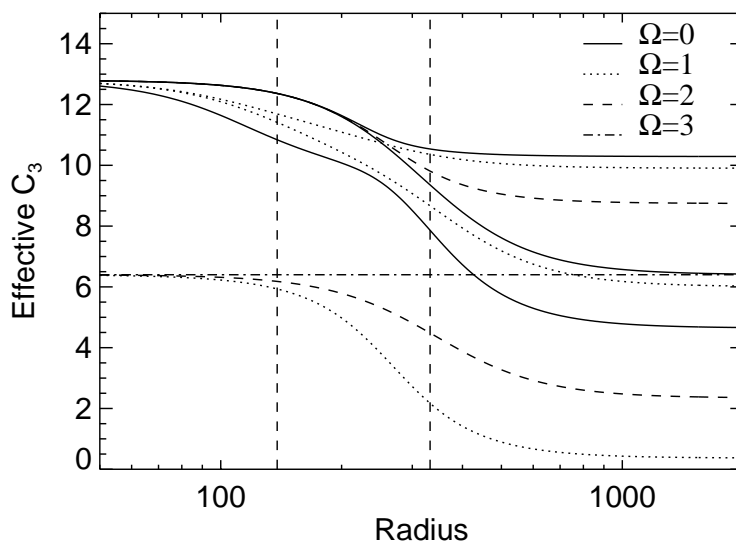


Figure 4.9 Effective C_3 coefficient plotted as a function of the internuclear distance R . The vertical dashed lines indicate the internuclear distances at which the potential energy is equal to the fine structure splittings of the $J=0$ and the $J=1$ asymptote. These distances are found by using an average C_3 coefficient of $C_3 = 10$ a.u. to calculate the potential energy.

that the C_3^{eff} coefficient is constant at distances of $R > 1000 a_0$ and at ranges of $R = (20 - 100) a_0$. In the range of $(20 - 100) a_0$ the potentials are described by Hund's case (a) states which have a pure C_3/R^3 behavior. Their C_3 coefficients are fractions of 1/3 or 2/3 of the dispersion coefficient.

The coupling between the states is expected to be largest in the region where the fine structure interaction is comparable to the depth of the potential. In Fig. 4.9 the vertical lines indicate the distances at which these energies are identical. When the coupling is strongest the variation of the C_3^{eff} coefficient should be largest. It is clear that the coupling is not only strong at the positions indicated by the vertical lines. It is substantial in the whole region between $R = (100 - 1000) a_0$. This is precisely the region where the outer turning points of the bound states lie in the frequency region where we excite the bound states. This is the reason why the C_3 coefficients that are found from the L-B fits of the three series are average values. Therefore we cannot use them to assign the series to specific states.

4.4.3 Accumulated phase analysis

We have further analyzed the spectra using the accumulated phase (AP) method which was first described by Moerdijk *et al.* [15]. It is used to assign the series of vibrational states that we found to specific states. Actually the AP method is based on the same approximation as the L-B analysis. It is assumed that the energetic position of bound states close to the dissociation limit is determined by the long-range part of the potential. The way in which this is incorporated in the model is that the phase accumulated by the wavefunction in the inner part of the potential does not depend on energetic the position of the bound state for these loosely bound states. Like the L-B analysis the AP method is only valid for bound states close to the dissociation limit.

In order to calculate energetic positions of bound states, the Schrödinger equation is numerically solved. The potentials in the outer region have been calculated as discussed in Chap. 3 and are shown in Fig. 4.7. The wavefunction is integrated in the outer region of the potential and its phase should match the phase that is accumulated in the inner region. If the position of one bound state in the potential is known the accumulated phase in the inner region can be fixed. Since this phase is identical for all bound states close to the dissociation limit, it can be used to calculate the positions of other bound states in the same potential.

In the L-B analysis a pure C_3/R^3 interaction potential was used. As is discussed in Sec. 3.5 and shown in Sec. 4.4.2 the actual potential curves do not have pure C_3/R^3 behavior in the region where the excitations to the bound states have

Table 4.2 Measured and calculated energetic peak positions. The positions have been calculated with the AP method. The positions are given as the detunings with respect to the He $2^3S_1 \rightarrow 2^3P_2$ asymptote in GHz.

measured position	<i>Series 1</i>		measured position	<i>Series 3</i>	
	calculated position 0_g^+ state	calculated position 1_g state		calculated position 0_g^+ state	calculated position 1_g state
$-\Delta$ (GHz)	$-\Delta$ (GHz)	$-\Delta$ (GHz)	$-\Delta$ (GHz)	$-\Delta$ (GHz)	$-\Delta$ (GHz)
0.45	0.19	0.27	0.50	0.43	0.51
0.93	0.76	0.84	1.20	1.10	1.18
1.77	1.67	1.72	2.27	2.26	2.29
3.20	3.16	3.18	4.07	4.07	4.07
5.45	5.44	5.43	6.85	6.79	6.78
8.80	8.80	8.80	10.73	10.77	10.76
13.67	13.68	13.65			

been made. The analysis of the peak positions can be improved by using the actual long-range potential curves. In the AP analysis that we did, the correct potential curves have been used. In Tab. 4.2 the measured peak positions are shown together with the peak positions found with the accumulated phase method for the best matching states. We can assign series 1 and 3 to both a 0_g^+ and a 1_g state. We cannot distinguish between the 0_g^+ and the 1_g state enough to determine which state belongs to which series.

We have compared the positions found with the AP method with the positions found with the L-B method. This is shown in Fig. 4.10. The L-B method is used to find the least bound vibrational state. The AP method cannot be used to determine the most loosely bound state, since such a calculation would require the potential to be calculated up to infinite distances. We have calculated the potential up to distances of $500a_0$. It can be seen that for more deeply bound states the deviation between the positions found with the L-B method and the AP method increases. Since both the L-B method and the AP analysis are based on the same approximations it is in principle hard to state which method should be most accurate. However, in this case it is clear that more information can be obtained from the AP-method, since the actual potentials can be used, while with the L-B analysis we are restricted to using a simple C_3/R^3 potential. Therefore

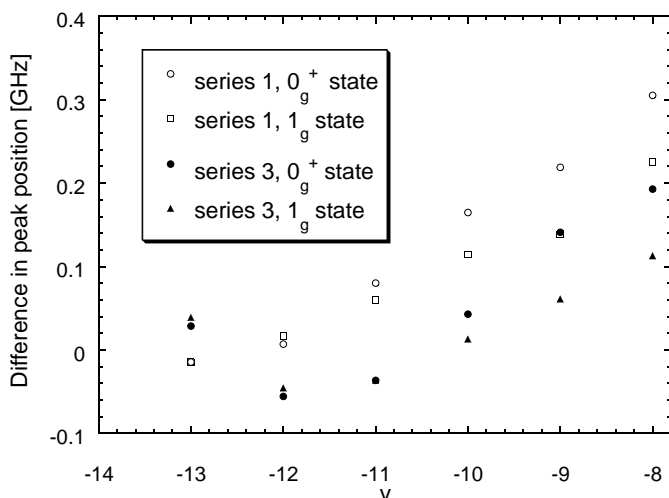


Figure 4.10 Difference in peak position between positions calculated with the L-B method and the AP method. The most loosely bound vibrational level is labeled with $v = 0$. Series 1 and series 3 are the series indicated in Tab. 4.1. The L-B fits shown in Fig. 4.8 have been used to obtain the peak positions that follow from the L-B method. The positions obtained with the AP method are shown in Tab. 4.2. Since it is not possible to state whether the 0_g^+ or the 1_g state fit best with series 1 and 3 they are both compared with the positions that are found with the L-B method.

the AP analysis provides more information that can be used to assign the series to particular states.

4.4.4 Ionization Mechanism

The bound states are detected by measuring ionization rates. It is not beforehand clear why this is possible. In this section we will describe a mechanism that explains why the ionization rate can be used as a signature of a bound state.

At short internuclear distances, where the molecular states can be described with Hund's case (a) states, the total spin S and the projection of the spin on the internuclear axis Σ are good quantum numbers. For singlet and triplet states the Penning ionization probability at short range is very large, almost unity. For quintet states Penning ionization is forbidden by the spin selection rule. This has

been verified for thermal collisions [16].

If a bound state would be excited in a singlet or triplet potential, the lifetime of this bound state would be extremely short, as a result of the efficient ionization. Therefore the width of the state would be extremely large and an ion peak would be too broad to be observed. Now, if a bound state would be excited in a quintet potential, the lifetime of this bound state would be long, since the ionization rate would be zero. However, it would not be possible to detect the excitation of such a state by an increase of the ionization rate. On the contrary, one would expect a decrease in the ionization rate when a bound state is excited in a quintet potential. The ionization probabilities at short range have been verified only for the He $2^3S_1 - 2^3S_1$ system, but we have no reason to expect that they are different for the the He $2^3S_1 - 2^3P_2$ system.

The simple picture given above is not complete. As we discussed in Sec. 3.5, at the internuclear distances where the bound state are excited, the molecular states must be described with Hund's case (c) states. At those distances a state is a superposition of Hund's case (a) states and the spin states are mixed due to the fine structure interaction. Due to this mixing of states the ionizing singlet and triplet states and the non-ionizing quintet states are coupled. The coupling of

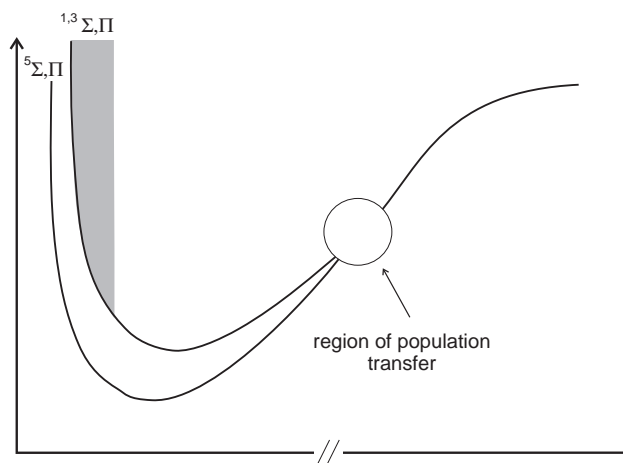


Figure 4.11 Schematic figure of the mechanism that is responsible for ion formation. The shaded region is the region where ionization takes place.

the states is strongest in the region where the dipole-dipole interaction energy is comparable to the fine-structure interaction. This can be seen in Fig. 4.9, where the variation of the C_3^{eff} coefficient due to the coupling is shown.

In Fig. 4.11 a schematic picture of the mechanism that is responsible for the increase of the ionization is shown. After a bound state is excited, part of the population is transferred to a state that ionizes at short range. The coupling to the ionizing state should not be too large, since otherwise the lifetime of the bound state is too short to detect a peak in the ionization rate. Indeed the states that have been identified, the 0_g^+ and the 1_g state both have a high quintet character.

The ionization peaks have been observed in a detuning range from 0 to 20 GHz. This is consistent with the mechanism described above, since this is precisely the range where the coupling due to the fine-structure interaction is strongest. To study more deeply bound states a different detection method should be used.

4.5 Conclusions

We have studied several features of photoassociation spectra of He*. Contrary to what is the case for the alkali systems, photoassociation of He* has not been studied in detail yet. We have measured three series of vibrational states in the range from - 20 to 0 GHz. Two of these series can be identified as either a 0_g^+ or a 1_g state. The bound states are detected through ionization via an indirect process. We can describe this process qualitatively. The mechanism allows us to detect ions as a result of excitation to a bound state only in the range where the fine structure splitting is comparable to the well depth of the potential. If we want to study deeper lying states different detection methods should be applied.

References

- [1] P. D. Lett, P. S. Julienne, and W. D. Phillips, *Ann. Rev. Phys. Chem.* **46**, 423 (1995).
- [2] W. C. Stwalley and H. Wang, *J. Mol. Spectrosc.* **195**, 194 (1999).
- [3] E. Tiesinga, C.J. Williams, P.S. Julienne, K.M. Jones, P.D. Lett, and W.D. Phillips, *J. Res. Natl. Inst. Stand. Technol.* **101**, 505 (1996).
- [4] W.I. McAlexander, E.R.I. Abraham, N.W.M. Ritchie, C.J. Williams, H.T.C. Stoof, and R.G. Hulet, *Phys. Rev. A* **51**, 871 (1995).
- [5] K.M. Jones, P.S. Julienne, P.D. Lett, W.D. Phillips, E. Tiesinga, and C.J. Williams, *Europhys. Lett.* **35**, 85 (1996).

-
- [6] P.A. Molenaar, P. van der Straten, H.G.M. Heideman, Phys. Rev. Lett. **77**, 1460 (1996).
- [7] P.O. Fedichev, M.W. Reynolds, U.M. Rahmanov, and G.V. Shlyapnikov, Phys. Rev. A **53**, 1447 (1996).
- [8] N. Herschbach, P.J.J. Tol, W. Vassen, W. Hogervorst, G. Woestenenk, J.W. Thomsen, P. van der Straten, and A. Niehaus, Phys. Rev. Lett. **84**, 1874 (2000).
- [9] H. C. Mastwijk, J. W. Thomsen, P. van der Straten, and A. Niehaus, Phys. Rev. Lett. **80**, 5516 (1998).
- [10] B.J. Thijsse, M. A. Hollanders, and J. Hendriks, Comput. in Phys. **12**, 393 (1998).
- [11] R. Napolitano, J. Weiner, C.J. Williams, and P.S. Julienne, Phys. Rev. Lett. **73**, 1352 (1994).
- [12] M. Movre and G. Pichler, J. Phys. B **10**, 2631 (1977).
- [13] C.J. Williams and P. S. Julienne, J. Chem. Phys. **101**, 2634 (1994).
- [14] R.J. Leroy and R.B. Bernstein, J. Chem. Phys. **52**, 3869 (1970)
- [15] A.J. Moerdijk, W.C. Stwalley, R.G. Hulet, and B.J. Verhaar, Phys. Rev. Lett. **72**, 40 (1994).
- [16] M. Müller, A. Merz, M.W. Ruf, H. Hotop, W. Meyer, and M. Movre, Z. Phys. D **21**, 89 (1991).

Chapter 5

Effects near the $2^3S_1 - 2^3P_1$ Asymptote

5.1 Introduction

Photoassociation spectroscopy (PAS) of cold atoms is a powerful technique to study long-range interactions [1–3]. Numerous photoassociation experiments have been performed with alkali atoms providing detailed information on ground and excited state potentials. Due to the low kinetic energy of the colliding cold atoms, the measurements can be performed with high precision. Recently for the first time PAS experiments with cold He* atoms have been reported (Chap. 4 and Ref. [4]). These measurements concerned PAS for the potentials connecting to the $2^3S_1 - 2^3P_2$ asymptote. In this chapter we study potential curves that connect to the $2^3S_1 - 2^3P_1$ asymptote, where the total angular momentum of the excited P-state is $J=1$, while it is $J=2$ for the 2^3P_2 state. The asymptotic energy of the $2^3S_1 - 2^3P_1$ system is very close to the asymptotic energy of the $2^3S_1 - 2^3P_2$ system, only 2.29 GHz above it. As a result the behavior of several potential curves connected to the $2^3S_1 - 2^3P_1$ asymptote is different from the behavior of the potentials connected to the $2^3S_1 - 2^3P_2$ asymptote. Due to avoided crossings between potentials with identical symmetries, some of the potentials connected to the $2^3S_1 - 2^3P_1$ asymptote have very large inner turning points, of the order of a few times $100 a_0$. These potentials have been described in Sec. 3.5.1 and are named purely long-range potentials.

PAS is performed by making a free-bound transition from the ground state to the excited state. This is shown schematically in Fig. 5.1, where only one attractive potential and one purely long-range potential connected to the $2^3S_1 - 2^3P_1$ asymptote are shown, while in reality there are several potential curves. The potentials connecting to the $2^3S_1 - 2^3P_2$ asymptote are not shown in the figure,

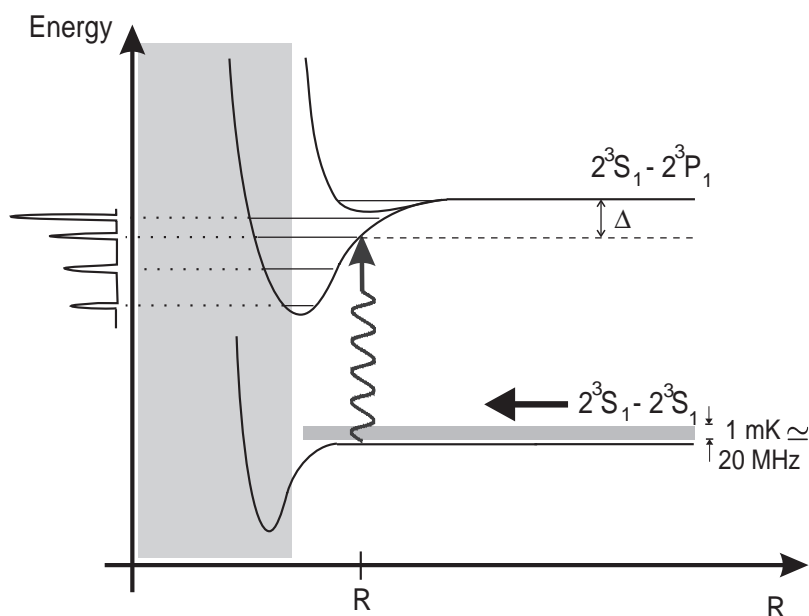


Figure 5.1 Principle of PAS. In this case the $2^3S_1 - 2^3P_1$ potential is scanned with a probe laser. When the laser is resonant with a vibrational state energy, population is transferred from the free system in the $2^3S_1 - 2^3S_1$ potential to a bound state in the $2^3S_1 - 2^3P_1$ potential. Both an attractive potential curve and a purely long-range potential curve have been drawn. The shaded region at small internuclear distances shows the region where Penning ionization plays a role. Δ is the detuning of the probe laser with respect to the atomic resonance. The kinetic energy spread due to the temperature of the trapped atoms is indicated by the shaded region on top of the $2^3S_1 - 2^3S_1$ potential. Note that the energy and the internuclear distance R have not been drawn at the right scale.

although the asymptotic energy lies only 2.29 GHz below the asymptotic energy of the $2^3S_1 - 2^3P_1$ asymptote. The transition in the PAS process is made at the internuclear distance R_c where the Franck-Condon overlap between the ground state wavefunction and the excited state wavefunction is the largest. The atoms in the magneto-optical trap are ultra-cold, which means that the wavefunction of the free atoms in the S - S potential varies slowly with the internuclear distance. Therefore the overlap with vibrational states in the S - P potential is largest at the

classical outer turning points of bound states in the excited potential. The probe laser is scanned in frequency and when its frequency is resonant with an excited bound vibrational state, population can be transferred to this state and a resonance can be observed.

In this chapter photoassociation experiments close to the $2^3S_1 - 2^3P_1$ asymptote will be described. In these experiments we have been able to identify three different effects, which will be discussed separately. Only a qualitative analysis will be given. The experimental methods used will be described in Sec. 5.2. In Sec. 5.3 the excitation of vibrational states will be discussed. In Sec. 5.4 the observation of a dip in the ionization rate will be analyzed, which we attribute to the excitation of a bound state in a purely long-range potential. Finally in Sec. 5.5 we will show peaks in the ionization rate at positive detunings, which we interpret as the observation of shape resonances.

5.2 Experiments

The experiments have been done in a magneto-optical trap (MOT). The trap is loaded with a beam of He* atoms that is produced in a DC-discharge source, cooled with liquid helium. The mean velocity of the atoms leaving the source is 300 m/s. Before the He* atoms are trapped in the MOT they are Zeeman slowed with a counter-propagating laser beam while the position dependent Zeeman shift is realised by the magnetic field of the MOT coils. Typically we trap 10^6 atoms with a temperature of 1 mK and a density of a few times 10^9 cm⁻³. The atoms are cooled on the $2^3S_1 \rightarrow 2^3P_2$ transition, which has a wavelength of 1083 nm.

A probe laser scans the potential curves connected to the $2^3S_1 - 2^3P_1$ asymptote. The ion rate is measured as a function of the probe laser frequency, using micro-channel plates (MCPs). In Fig. 5.2 a picture of the experimental setup is shown, with the trapping laser beams and the probe beam. The laser light is generated by diode lasers. The frequency of the probe laser light is calibrated using a Fabry-Perot interferometer for the relative frequency scale and the Lamb dip to determine the absolute frequency. The position of the Lamb dip is measured in a saturated absorption spectroscopy setup as discussed in Sec. 2.5.

The trapping laser operates close to the $2^3S_1 - 2^3P_2$ asymptote at a detuning of -12.5 Γ . Since the rate constant for PI is a factor of 100 larger for collisions in the $2^3S_1 - 2^3P_2$ potential than for collisions in the $2^3S_1 - 2^3S_1$ potential, the trapping laser induces a large number of ions [5]. To avoid this huge background ionization signal the trapping laser is periodically switched on and off during the

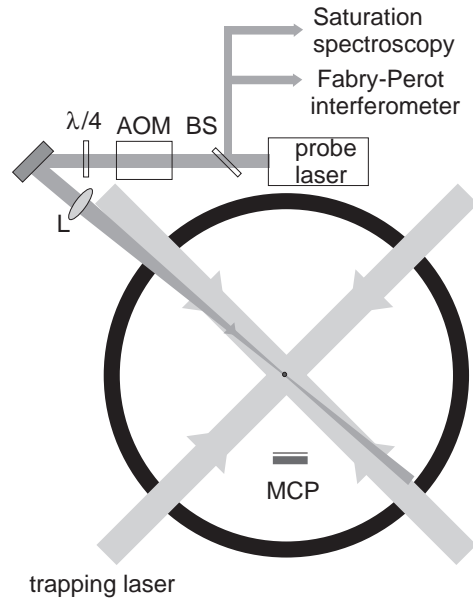


Figure 5.2 Probe laser setup. M stands for mirror, $\lambda/4$ for quarter wave retardation plate, L for lens, BS for 5% beam splitter, AOM for acousto-optical modulator, and MCP for micro-channel plates.

measurements, by detuning its frequency 500 MHz to the red of the $2^3S_1 \rightarrow 2^3P_2$ transition. This is far enough to ensure that the laser light does not induce many ions. The period when the trapping laser is switched on will be called the trapping period, while the period where the trapping laser is switched off will be called the probing period. The probing period is fixed at $20 \mu s$, regardless of the duty cycle of the switching of the laser. This period is short enough to avoid any significant expansion of the cloud of trapped atoms in the probing period. The duty cycle for the probing period is varied between 10% and 25%, depending on the intensity of the probe laser. The probe laser beam can be switched off in the trapping period using an acousto-optical modulator (AOM). The first order diffraction beam is then used as a probe laser. In this way we can make sure that the cloud of trapped atoms is not perturbed by the probe laser beam. The ion signal is gated and can be measured both in the probing period and in the trapping period. In the probing period the dependence of the ion rate on the probe laser frequency

is measured, while the signal in the trapping period is used to monitor the stability of the trapped cloud. A typical scan time is 100 s. In the experiments described below the probe laser was either on continuously or periodically switched off using the AOM.

5.3 PAS near the $2^3S_1 - 2^3P_1$ asymptote

In this experiment vibrational states in potentials connecting to the $2^3S_1 - 2^3P_1$ asymptote are probed. The measurements are similar to the photoassociation spectroscopy measurements for the $2^3S_1 - 2^3P_2$ asymptote, which are described in Chap. 4. First the results will be shown and then a short analysis will be given.

5.3.1 Results

We have measured the ion rate as a function of the probe laser frequency, while the probe laser was on continuously. A typical spectrum is shown in Fig. 5.3. The

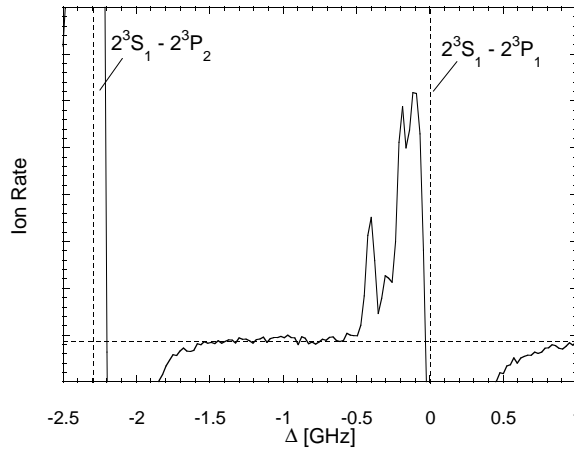


Figure 5.3 Photoassociation spectrum measured as a function of the probe laser frequency. The frequency is given as the detuning Δ with respect to the $2^3S_1 - 2^3P_1$ asymptote. The saturation parameter of the probe laser was $s_0 = 10^3$. The background ion signal is indicated by the horizontal dashed line. The asymptotic energies for the $2^3S_1 - 2^3P_2$ and the $2^3S_1 - 2^3P_1$ system are given by the vertical dashed lines.

saturation parameter of the probe laser was $s_0 = 10^3$. Several scans were added to produce the spectrum. Distinct peaks can be observed, which have similar properties as the ones detected in the spectra discussed in Chap. 4 and therefore they can also be identified as excited bound states. Since the probe laser is on continuously, it affects the cloud of trapped atoms when the laser is tuned close to the atomic resonance. This effect can be observed at frequencies around the $2^1S_1 - 2^3P_1$ asymptote and around the $2^3S_1 - 2^3P_2$ asymptote.

The spectra have been measured as a function of the probe laser intensity. When the intensity is increased, the height of the peaks increases and more deeply bound states can be excited. However, the region where the trap is perturbed by the probe laser also increases with increasing intensity and hence the frequency range in which bound states can be observed decreases. The positions of all excited bound states that are measured between the $2^3S_1 - 2^3P_2$ and the $2^3S_1 - 2^3P_1$ asymptote are listed in Tab. 5.1.

The widths of the ion peaks in the spectra have been determined as a function of the probe laser intensity, for intensities ranging from $s_0 = 10^2$ to $s_0 = 10^5$. They have been fitted with Gaussian line shapes, since it is expected that their

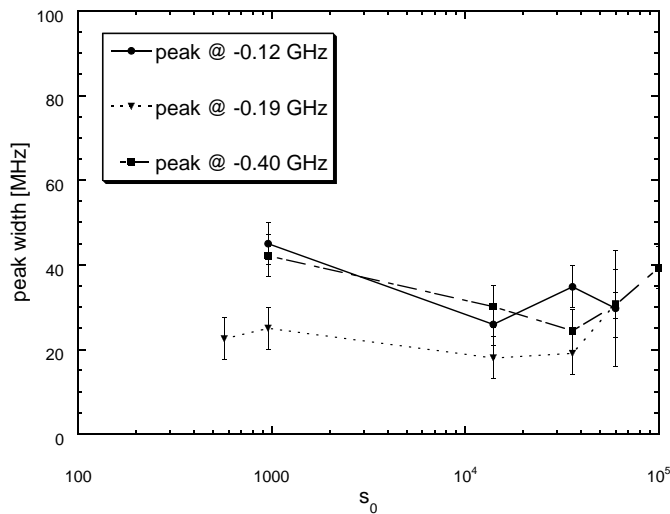


Figure 5.4 Peak widths as a function of the probe laser intensity. The lines are drawn to guide the eye.

Table 5.1 List of the positions of the photoassociation peaks measured between the $2^3S_1 - 2^3P_2$ and the $2^3S_1 - 2^3P_1$ asymptote. The detuning Δ is given with respect to the $2^3S_1 - 2^3P_1$ asymptote. The position of a very weak peak is given in parentheses.

n	$-\Delta$ (GHz)
1	0.05
2	0.12
3	0.19
4	0.29
5	0.40
6	0.57
7	(1.17)

widths are mostly determined by the temperature of the trapped atoms. In Fig. 5.4 the widths of three peaks have been plotted as a function of ν_0 . The width does not increase significantly when the probe laser intensity increases. It is not possible to determine the widths of the small peaks and of the ones that overlap with neighboring peaks. The mean width, that is found when low probe laser intensities are used, is (34 ± 13) MHz. The temperature of the atoms in the MOT is 1 mK, which corresponds to an energy of 20 MHz. Therefore it can be concluded that the width is mostly determined by the temperature of the trapped atoms.

5.3.2 Analysis

The PAS measurements shown here probe bound states in potentials connecting to the $2^3S_1 - 2^3P_1$ asymptote. They have similar properties as the PAS measurements probing bound states in potentials connected to the $2^3S_1 - 2^3P_2$ asymptote, discussed in Chap. 4. In principle the analysis that was done in Chap. 4, can also be applied here.

First of all an analysis is made of the positions of the peaks that are measured. The only states that can be uniquely attributed to potentials connecting to the $2^3S_1 - 2^3P_1$ asymptote are the states that are probed at energies between the $2^3S_1 - 2^3P_2$ and the $2^3S_1 - 2^3P_1$ asymptotic energies. This energy range is only 2.29 GHz wide and therefore strongly limits the number of peaks that can be detected. We can use the Leroy-Bernstein analysis (L-B) to find a series of vibrational states [6]. In this approach it is assumed that the positions of the high-lying vibrational states

are completely determined by the long-range part of the potential, since most time is spent in the outer range of the potential. Therefore the approximation is only valid close to the dissociation limit. The long-range part of the S-P potential has the shape $V(R) = D - C_3/R^3$, where D is the dissociation limit and the C_3/R^3 term originates from the dipole-dipole interaction. Leroy and Bernstein deduced that the positions of the vibrational levels should then be given by:

$$E_v - E_d = \frac{1}{C_3^2} \left(\frac{\hbar}{2} \sqrt{\frac{2\pi}{\mu}} \frac{\Gamma(4/3)}{\Gamma(5/6)} (v - v_d) \right)^6, \quad (5.1)$$

where E_v is the energy of a vibrational level, E_d is the dissociation energy, v is the vibrational quantum number, v_d is the effective vibrational quantum number of the level at the dissociation limit, and $\Gamma(n)$ is the Gamma-function. It is possible to make a L-B fit, including all peaks listed in Tab. 5.1. However, from this fit we obtain a C_3 coefficient which is equal to 80 a.u. The dispersion coefficient μ for the S-P potential is 19.20 a.u. and the C_3 coefficient must be a fraction of μ (see Sec. 3.4 and Sec. 4.4.1). Therefore the value of 80 a.u. for the C_3 coefficient cannot be physical. The L-B fit is rather insensitive if only a small number of vibrational levels is included in the fit, especially if the distance between the levels is small. From the fact that the value of the obtained C_3 coefficient is not physical, we can conclude that there must be more than one series of vibrational states present in the spectra. Unfortunately, the available information is too limited to find the series of vibrational states and to assign these series to specific potentials. The mechanism, which is responsible for the formation of ions when a bound state is excited, is identical to the mechanism described in Sec. 4.4.4 and will therefore not be discussed here.

5.4 Purely long-range states

In this section we study effects very close to the atomic resonance. To be able to observe effects at these frequencies, we must take care not to perturb the trap with the probe laser. Therefore the probe laser is switched off with an AOM in the trapping period. We will discuss the effects that are observed at negative detunings, close to the atomic resonance.

5.4.1 Results

We have used various probe laser intensities to investigate the region around the atomic resonance, varying the saturation parameter from $s_0 = 40$ to $s_0 = 600$. Two typical spectra are shown in Fig. 5.5. In the spectrum measured with the probe laser intensity of $s_0 = 100$ a dip in the ionization rate is found at a negative detuning, $\Delta \sim -30$ MHz. The ion rate has simultaneously been measured in the trapping period, to check whether the trap is not partially emptied by the probe at the position of the dip. This is not the case. Furthermore we have found that the shape and the size of the dip do not depend on the direction in which the probe laser is scanned. If the trap would be partially emptied by the probe laser, it would load again when the frequency of the probe laser was tuned away from the atomic resonance. In that case the shape of the loading curve of the MOT should be distinguishable in the rising flank of the dip, where the probe laser was tuned away from the atomic resonance. Therefore the shape of the dip should depend on the direction in which the probe laser is scanned. The fact that the scanning

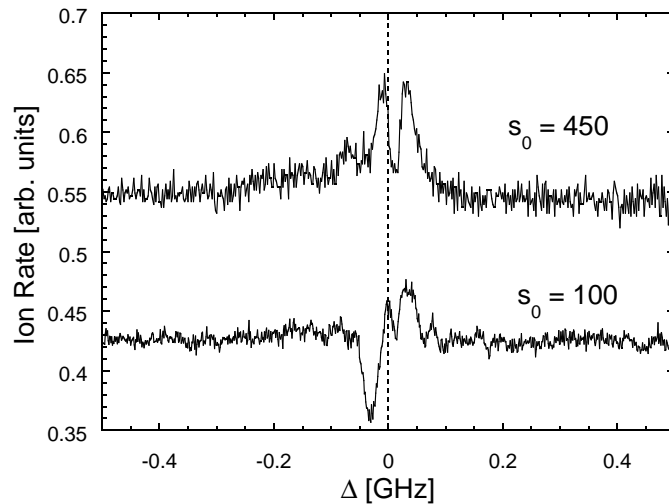


Figure 5.5 Two spectra taken when the probe laser does not perturb the cloud of trapped atoms. The spectra are taken with two different probe laser intensities, namely $s_0 = 100$ and $s_0 = 450$. The ion rate is expressed in arbitrary units and an offset is added to the upper spectrum for clarity. The dashed vertical line indicates the atomic resonance.

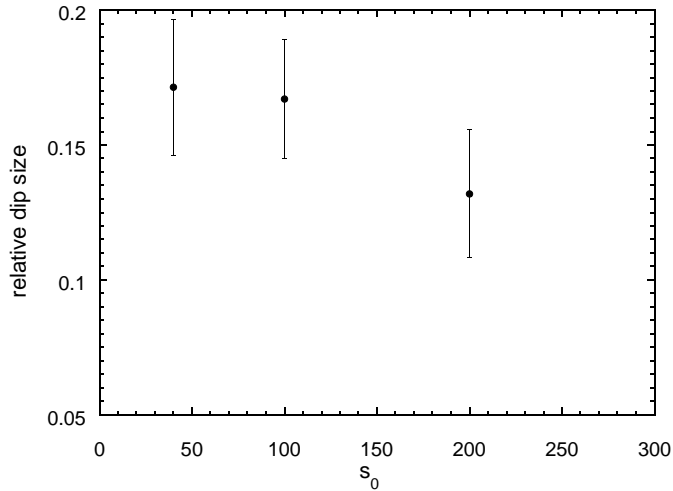


Figure 5.6 Size of the dip at the detuning $\Delta = -26$ MHz. The relative dip size, *i.e.* the size of the dip compared with the constant ion rate, is plotted as a function of the saturation parameter s_0 .

direction does not influence the shape of the dip is another argument that shows that the dip is not caused by the probe laser emptying the trap.

In Fig. 5.5 it can be seen that the dip disappears when the intensity of the probe laser is increased to $s_0 = 450$. We have determined the size of the dip as a function of the saturation parameter s_0 . The relative size, compared with the constant background ion signal is plotted in Fig. 5.6. It is constant for $s_0 = 40$ and $s_0 = 100$ and then decreases when the saturation parameter increases. When the intensity increases not only the dip disappears, but also peaks start to appear at negative detunings (see Fig. 5.5). These peaks result from excitations to the bound states that were probed in the PAS measurements discussed in Sec. 5.3. A list of the positions of the dip and the peak at negative detunings for various probe laser intensities is given in Tab. 5.3.

5.4.2 Analysis

Some of the potentials, that are connected to the $2^3S_1 - 2^3P_1$ asymptote, have a purely long-range behavior. They are attractive at long range and become re-

pulsive at internuclear distances in the order of a few $100 a_0$. These potentials result from avoided crossings between potential curves. We have calculated these potentials using the Movre-Pichler analysis [7], as is described in Chap. 3. The purely long-range potentials, which connect to the $2^3S_1 - 2^3P_1$ asymptote, are shown in Fig. 5.7. They are very shallow, namely their depths range from 0.05 to 2.1 GHz. Because of their small depths they can support only a small number of bound states, compared to the number of bound states that can be supported in the attractive potentials for the $2^3S_1 - 2^3P_{0,1,2}$ system. Only atomic parameters are used in the calculation of the positions of the bound states in the purely long-range potentials and therefore the calculation is very accurate. Hence very precise information can be extracted from the observation of these bound states. In a PAS experiment with sodium the measured positions of bound states in a purely long-range potential have been used to determine the excited state lifetime and to measure retardation effects with great precision [8]. A similar experiment is done for potassium, by Wang *et al.* [9, 10].

The excitation of a bound state in a purely long-range potential should for He^* be observed as a decrease of the ionization rate. This can be understood by looking at the inner turning points of bound states in the purely long-range potentials. These inner turning points are at very large distances, of the order

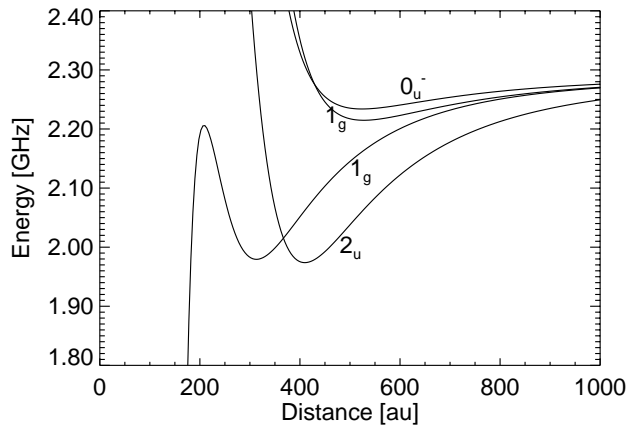


Figure 5.7 Purely long-range potentials connected to the $2^3S_1 - 2^3P_1$ asymptote.

of a few $100 a_0$. Therefore the system cannot reach the region where Penning ionization (PI) takes place, which is at internuclear distances of a few a_0 . Hence the excitation of a purely long-range bound state can be observed as a suppression of the ionization rate. The dip that is observed at the detuning of -26 MHz can be attributed to the excitation of such a state.

We have calculated the positions of the bound states in the purely long-range potentials, to verify whether we can find a bound state at the position where the dip in the ionization rate is observed. The positions of the bound states are listed in Tab. 5.2. The bound states for the 1_g potential with the double well structure have not been calculated. The maximum of the barrier located around $200 a_0$, that determines the inner turning point of the purely long-range bound states, lies below the asymptotic energy. Therefore the bound states lying above this barrier must also exist at short range and their position cannot be calculated using just atomic parameters. When rotation of the molecule is added to the potential the maximum of the barrier lies above the asymptotic energy and this argument is not valid anymore. However, we are interested in the most loosely bound states and

Table 5.2 Bound states in the purely long-range potentials connected to the $2^3S_1 - 2^3P_1$ asymptote. The bold printed states lie at the detuning where the dip in the ionization rate is observed, within experimental error.

State	v	J	$-\Delta$ (MHz)	r_{inner} (a_0)	r_{outer} (a_0)	r_{aver} (a_0)
0_u^-	0	0	20.6	444	856	720
	0	1	16.6	449	883	743
	0	2	9.32	461	954	804
	0	3	0.33	487	1201	952
1_g	0	1	30.2	451	819	693
	1	1	3.09	432	1755	1189
	0	2	21.9	459	856	724
	0	3	10.7	474	934	791
2_u	0	2	192	352	554	474
	1	2	70.9	330	805	657
	2	2	19.9	323	1232	997
	0	3	166	357	565	483
	1	3	55.6	335	837	684
	2	3	12.4	329	1337	1073

for these states the wavefunction can probably tunnel rather efficiently through the barrier, because the height of the barrier is small. For these two reasons it is complicated to calculate positions of bound states in this potential. If we just consider the calculated bound states in the other three potentials, we find four states which are at the measured position within the accuracy of the measurement, namely the 0_u^- potential with $v = 0$ and $J = 0$, the 1_g potential with $v = 0$ and $J = 1$ or $J = 2$, and the 2_u potential with $v = 2$ and $J = 2$. Note that the rotation of the molecule is included in the calculation of these states [11], while rotation was not included in the calculation of the potentials described in Chap. 3. We cannot determine which of these four ro-vibrational states is probed in the spectra. It is possible that we probed more than one state. If it is the bound state in the 2_u potential that we have excited, it is surprising that only one dip is observed, since there are a number of states relatively far from the atomic resonance.

In the analysis given above we have not discussed the dependence of the observed dip on the saturation parameter, s_0 , of the laser, although the size of the dip is strongly dependent on s_0 . As was shown in Sec. 5.4.1, the dip in the ionization rate disappeared, when the saturation parameter of the probe laser was increased to $s_0 = 450$. Furthermore, peaks started to appear at negative detunings and we observed an increase of the ionization rate due to optical collisions. The positions of the peaks are identical to the positions of the peaks discussed in Sec. 5.3 and are attributed to the excitation of bound states in attractive potentials. Optical collisions are binary collisions in the presence of nearly-resonant light. They are discussed in Chap. 6 for light with frequencies close to the $2^3S_1 - 2^3P_2$ asymptote. In principle the discussion in Chap. 6 also applies here. However, the states connected to the $2^3S_1 - 2^3P_1$ asymptote are strongly coupled, so it is more difficult here to predict the increase of the ionization rate due to optical collisions.

In order to explain the laser intensity dependence of the measured signal, we must conclude that there are competing excitation processes, where either a non-ionizing purely long-range bound state, an ionizing bound state or an optical collision can be excited, as is illustrated in Fig. 5.8. Depending on the saturation parameter of the laser, one of these excitation processes is favored. We investigate this behavior by considering the probability for excitation for the atoms colliding in the $2^3S_1 - 2^3S_1$ potential to the potentials connected the $2^3S_1 - 2^3P_1$ asymptote. To calculate the excitation rate we use the semi-classical Landau-Zener transition probability [14] at the distance where the excitation is made:

$$P_{exc} = 1 - \exp(-\pi \Lambda), \quad (5.2)$$

with

$$\Lambda = \frac{\hbar\Omega^2}{2\alpha v_{rad}}, \quad (5.3)$$

where Ω is the Rabi frequency, α is the gradient of the potential at R_c , and v_{rad} is the radial velocity of the atoms. The Rabi frequency Ω is given by $\Omega^2 = s_0\Gamma^2/2$. First we examine the situation for low saturation parameters of the laser. As will be explained in Sec. 6.4, the excitation rates are not identical for all excited potentials. We have calculated the excitation rates for all potentials and have found that one of the purely long-range potentials is a dominant channel. However, if the saturation parameter is increased the Rabi frequency Ω is also increased, and

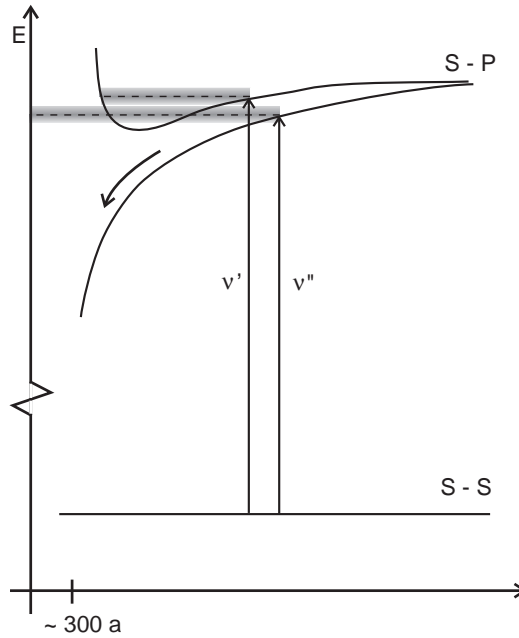


Figure 5.8 Schematic picture of a purely long-range potential and an attractive potential connected to S-P asymptote. In both potentials a bound state is shown, indicated with the dashed line. The bound states lie at different detunings from the S-P asymptote and therefore are probed with different laser frequencies ν . The shaded region around the bound states indicates the frequency width, in which population can be transferred to the bound state.

the excitation probabilities increase to unity for all allowed transitions. The attractive potential shown in Fig. 5.8 is steeper than the purely long-range potential. Therefore, if the intensity is high enough, all population can be transferred to the bound state in the attractive potential, before the outer turning point of the bound state in the purely long-range potential has been reached. Furthermore, close to the atomic resonance the system can ionize in an optical collision, preventing the bound state in the purely long-range potential to be populated. In the discussion above we did not take into account that the excitation to a bound state should be a resonant excitation and thus can only be made at discrete resonant energies. If the width of the transition would be infinitely small, it would not be possible that the excitation of one bound state would be dominant over the excitation of another bound state, that is bound with a different energy. In reality the linewidth is broadened due to the temperature of the atoms and the intensity of the probe laser, as is indicated in Fig 5.8 by the shaded region around the bound states. Thus we can explain why a dip is observed in the spectra when low saturation parameters are used and why a peak appears instead of a dip when the saturation parameter is increased.

5.5 Shape resonances

In this section we also study effects close to the atomic resonance. Here we are interested in a different aspect of the spectra discussed in Sec. 5.4, namely the effects at positive detunings, while in Sec. 5.4 we studied the effects at negative detunings.

5.5.1 Results

In the spectra shown in Fig. 5.5 there is, besides the dip in the spectrum at a negative detuning which was discussed above, also a peak in the spectrum at a positive detuning. Two peaks have been observed, one at a detuning of $\Delta = (+14 \pm 6)$ MHz, and one at a detuning of $\Delta = (+33 \pm 6)$ MHz. The peak at $\Delta = +14$ MHz is only observed for the lowest saturation parameter used, namely when $s_0 = 40$. The peak at $\Delta = +33$ MHz is observed for larger saturation parameters. In Tab. 5.3 a list is given of all dips and peaks that are measured at the various saturation parameters. Since the peaks at positive detunings are observed at very small detunings, they were not observed in experiments where the probe laser was on continuously. In those experiments the probe laser perturbed the trap in the frequency region where these peaks were measured.

Table 5.3 A list of the positions of the peaks and dips measured when the probe laser does not perturb the cloud of trapped atoms. The uncertainty in the positions is 6 MHz.

s_0	dip	peaks		
	Δ (MHz)	Δ (MHz)	Δ (MHz)	Δ (MHz)
40	-26	-	+14	-
100	-26	-	-	+33
200	-26	-50	-	+33
450	-	-50	-	+33
600	-	-50	-	+33

5.5.2 Analysis

The observation of a peak at a positive detuning with respect to the atomic resonance, cannot be attributed to photoassociation to a bound state as that was discussed in Chap. 4 and Sec. 5.3.1. The reason for this is that a bound state which is probed at a positive detuning would have to be lying in the continuum of the potential and therefore could not exist. However, if the rotational barrier is included in the potential, one can see that there can exist a bound state at a positive detuning, if the maximum of the barrier lies above the asymptotic energy (see Fig. 5.9). Such a bound state is called a shape resonance. The wavefunction can tunnel through the rotational barrier. A shape resonance in the ground state has been observed for colliding Rb atoms by Boesten *et al.* [12, 13].

We calculate the potentials connected to the $2^3S_1 - 2^3P_1$ asymptote, including rotation of the molecule, to find a potential in which a shape resonance can be excited. We can exclude most potentials, using arguments discussed in Sec. 3.6. There we saw that the S-P potential goes as C_3/R^3 , while the S-S potential goes as C_6/R^6 . As is shown in Fig. 3.9, for the S-P potential partial waves up to $\ell = 12$ can penetrate the rotational barrier, while for the S-S potential only partial waves with $\ell = 0$ can reach small internuclear distances. A shape resonance at a positive detuning can only exist in a potential, if there exists a local maximum in the potential, which is larger than the asymptotic energy. This means that there can only exist shape resonances in the excited state potentials for $\ell > 12$. It would not be possible to excite such a shape resonance from the S-S potential because of the rotational barrier. The internuclear distance, where the shape resonance should be excited, could never be reached on the S-S potential for $\ell > 12$, only for $\ell = 0$, since it should be excited at its outer turning point.

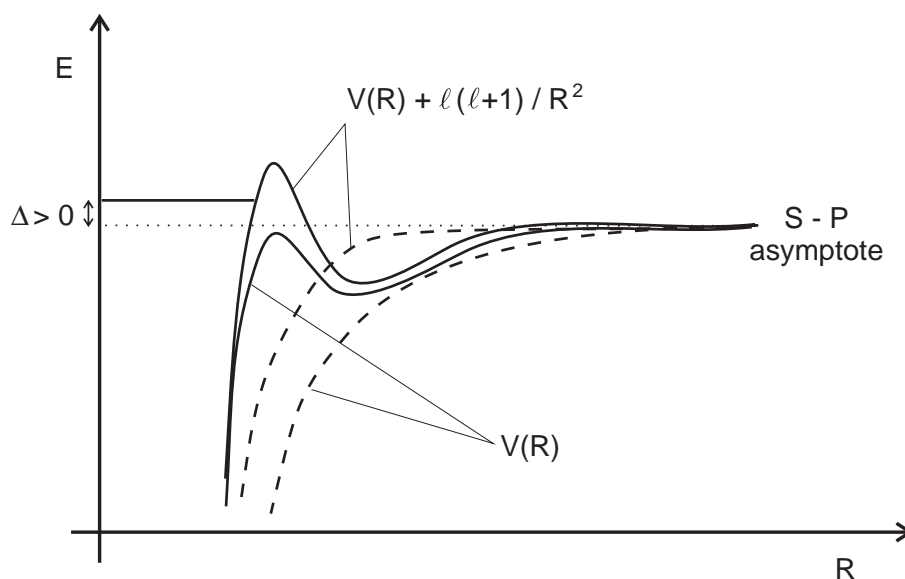


Figure 5.9 Schematic picture of a shape resonance. Four potential curves are drawn. The dashed lines represent the attractive potentials and the solid lines represent the 1_g state with the double well structure. The ones labeled with $V(R)$ are the potentials without rotation of the molecule and for the ones labeled with $V(R) + \ell(\ell + 1)/R^2$ the rotational barrier is included. The dotted line is the asymptotic energy. There can exist a bound state above the asymptotic energy in the double well potential, if rotation of the molecule is included.

There is one potential connected to the $2^3S_1 - 2^3P_1$ asymptote, that is a suitable candidate to support a shape resonance. This is the 1_g potential with the double well structure, as is illustrated in Fig. 5.9 and Fig. 5.10. If rotation of the molecule is not included in the calculation of the potential the maximum of the potential barrier lies below the asymptotic energy of the system. This is not physical, since there cannot exist a molecule without rotation. If rotation of the molecule is included we find that the maximum of the potential barrier increases to values above the asymptotic energy. In Fig. 5.10 the calculated 1_g potential is shown, including rotation of the molecule, for $J = 1, 2, 3$.

The excitation to the shape resonance should be made at the inner side of the potential barrier. On the ground state only partial waves with $\ell = 0$ can reach this

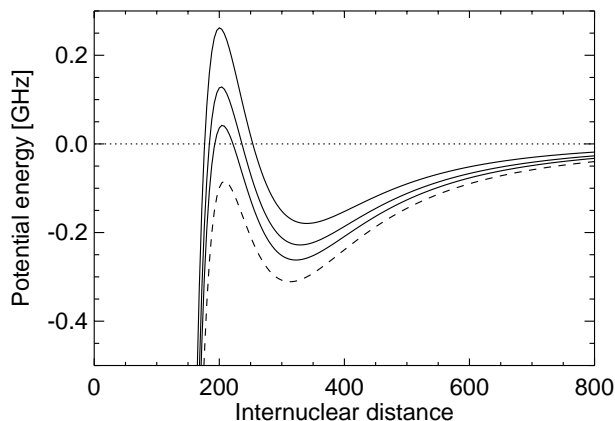


Figure 5.10 Calculation of the double well 1_g potential with rotation of the molecule included. The dashed line is the potential without rotation. The higher lying potentials have a total angular momentum of $J=1,2,3$ where the highest lying potential has the highest value of J . The dotted horizontal line represents the asymptotic energy of the $2^3S_1 - 2^3P_1$ system.

distance. The overlap between the wavefunctions is largest near the maximum of the barrier (at R_{max}), where the derivative of the 1_g potential is zero. Since the ground state wavefunction is varying slowly with the internuclear distance the overlap is largest if the derivative of the potential is small. The overlap with a potential with a steep slope is small, as can be seen in the expression for the Landau-Zener excitation probability given in Eq. 5.2 and Eq. 5.3. Since the slope of the potential increases rapidly at internuclear distances smaller than R_{max} , it is not probable that the excitation takes place far from the maximum of the barrier. The two different peaks could originate from resonances in the 1_g potential with different total angular momentum J .

5.6 Conclusions

We have observed remarkable effects near the $2^3S_1 - 2^3P_1$ asymptote, doing photoassociation experiments. Bound states in attractive potentials have been ob-

served. Due to the limited number of observed bound states it is not possible to assign these states to specific potentials. However, we are sure that more than one series of vibrational states has been probed. At very small detunings, in the range of 10 - 30 MHz around the atomic resonance, we have observed two special states. The first one is identified as a bound state in a purely long-range potential. The other is interpreted as a shape resonance in an excited state potential. The position of both these states can yield high-precision information on the lifetime of the He*(2P) state. A more detailed analysis in combination with more precise experiments will need to be done to extract this kind of information from the spectra.

References

- [1] J. Weiner, V.S. Bagnato, S. Zilio, and P.S. Julienne, *Rev. Mod. Phys.* **71**, 1 (1999).
- [2] P. D. Lett, P. S. Julienne, and W. D. Phillips, *Ann. Rev. Phys. Chem.* **46**, 423 (1995).
- [3] W. C. Stwalley and H. Wang, *J. Mol. Spectrosc.* **195**, 194 (1999).
- [4] N. Herschbach, P.J.J. Tol, W. Vassen, W. Hogervorst, G. Woestenenk, J.W. Thomsen, P. van der Straten, and A. Niehaus, *Phys. Rev. Lett.* **84**, 1874 (2000).
- [5] H. C. Mastwijk, J. W. Thomsen, P. van der Straten, and A. Niehaus, *Phys. Rev. Lett.* **80**, 5516 (1998).
- [6] R.J. Leroy and R.B. Bernstein, *J. Chem. Phys.* **52**, 3869 (1970).
- [7] M. Movre and G. Pichler, *J. Phys. B* **10**, 2631 (1977).
- [8] K.M. Jones, P.S. Julienne, P. D. Lett, W.D. Phillips, E. Tiesinga, and C.J. Williams, *Europhys. Lett.* **35**, 85 (1996).
- [9] H. Wang, P.L. Gould, and W.C. Stwalley, *Phys. Rev. A* **53**, R1216 (1996).
- [10] H. Wang, P.L. Gould, and W.C. Stwalley, *Z. Phys. D* **36**, 317 (1996).
- [11] P. van der Straten, private communication.
- [12] H.M.J.M. Boesten, C.C. Tsai, B.J. Verhaar, and D.J. Heinzen, *Phys. Rev. Lett.* **77**, 5194 (1996).
- [13] H.M.J.M. Boesten, C.C. Tsai, J.R. Gardner, D.J. Heinzen, and B.J. Verhaar, *Phys. Rev. A* **55**, 636 (1997).
- [14] K.-A. Suominen, *J. Phys. B* **29**, 5981 (1996).

Chapter 6

Penning Ionization in Optical Collisions

6.1 Introduction

Since the development of laser cooling and trapping techniques [1], it has become possible to study collisions between ultra-cold atoms. As was discussed in previous chapters, interactions at long range play an important role for cold atoms. An important method to study long-range interactions is photoassociation spectroscopy, as is described in Chap. 4 and Chap. 5. In this chapter we study optical collisions of cold He* atoms, which we define as binary collisions in the presence of nearly-resonant light. Since the light is nearly resonant with the atomic transition frequency, the number of ro-vibrational states in the diatomic molecule is large and thus can be treated as a quasi-continuum. While photoassociation spectroscopy provides detailed information on vibrational states in potentials, with the optical collisions we study the dynamics of the collisions and the role of the Penning ionization process. In Fig. 6.1 a schematic picture of an optical collision is shown.

In the present work we discuss collisions between cold He (2^3S_1) atoms in a magneto-optical trap (MOT), which are excited by light with frequencies close to the $2^3S_1 \rightarrow 2^3P_2$ transition. The modification of these collisions can be monitored by the process of Penning ionization (PI). When the light is detuned to the red of the $2^3S_1 \rightarrow 2^3P_2$ transition, one can observe a strong increase of the ion rate with respect to the ion rate for collisions between two 2^3S_1 atoms. [2–6]. This strong increase is due to the fact that on the $2^3S_1 - 2^3S_1$ potential, which varies as R^{-6} only partial waves with $\ell = 0$ can penetrate the rotational barrier, while on the $2^3S_1 - 2^3P_2$ potential, which varies as R^{-3} partial waves up to $\ell = 12$ can penetrate

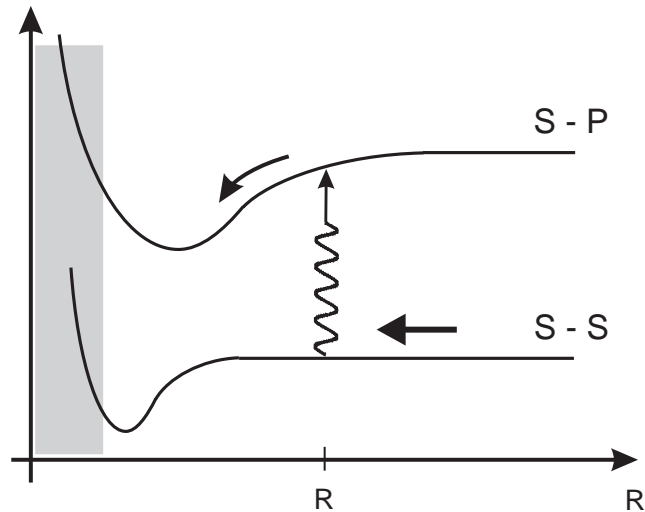


Figure 6.1 Schematic picture of an optical collision. An excitation is made from the S+S curve to the S+P curve at the distance R_c . The shaded region at small internuclear distances shows the region where Penning ionization plays a role.

the rotational barrier, as is shown in Sec. 3.6. Hence more close collisions are induced on the $2^3S_1 - 2^3P_2$ potential than on the $2^3S_1 - 2^3S_1$ potential.

For each ion that is created in a close collision, two atoms vanish from the trap and hence the ionization rate is part of the decay rate. In a MOT, loss can also be caused by radiative escape (RE), where the colliding atoms are accelerated on the attractive S-P potential and thus can gain enough kinetic energy to escape the trap after spontaneous emission to the S-S potential. The magnitude of the RE process depends on the relation between the lifetime for spontaneous emission and the collision time. Since the lifetime of the $2^3S_1 \rightarrow 2^3P_2$ transition is relatively long, the effect of RE is expected to be small compared to the losses due to ionization and the decay rate should be dominated by the ionization rate. This has been the basis for the evaluation of measured trap decay curves in terms of ionization rates [3,4,6].

Up until present, no rigorous theoretical description has been developed of the ion rate and trap decay for an ensemble of He (2^3S_1) atoms in the presence of nearly-resonant light. Such a description would require the calculation of all

ground and excited state molecular potentials and the coupling of these potentials by the light. Furthermore, a dynamical description should be given of the collision under the influence of the light. For the general case of one molecular ground and one molecular excited state models have been developed which provide a qualitative description of the increase of the collision rate constant in the presence of nearly-resonant light [7–9]. We have developed a semi-classical version of such a two-state model, described in recent publications [2, 10], that is able to reproduce the ionization rate constant for optical collisions of He* atoms.

In this chapter we present a semi-classical model, which we use to calculate the ionization rate constant and compare with measurements. In Sec. 6.2 the experimental method will be described. A partial wave formulation of our semi-classical two-state model will be given in Sec. 6.3. We will make an attempt to calculate the absolute ion rate constant in Sec. 6.4 by calculating the couplings between the various ground state potentials connected to the $2^3S_1 - 2^3S_1$ asymptote and the excited state potentials, connected to the $2^2S_1 - 2^3P_2$ asymptote. Subsequently we will apply the two-state model and compare the calculated ion rate constant with new measurements of improved quality. Finally in Sec. 6.5, the absolute ion rate constant will be compared with values that have appeared in the literature.

6.2 Experimental

The experiments are performed in a magneto-optical trap (MOT). The trap is loaded with a beam of He* atoms produced in a DC-discharge source, which is cooled with liquid helium. The mean velocity of the atoms leaving the source is 300 m/s. Before the He* atoms are trapped in the MOT, they are Zeeman slowed with a counter-propagating laser beam while the required Zeeman shift is produced by the magnetic field of the MOT coils. Typically we trap 10^6 atoms with a temperature of 1 mK and a density of a few times 10^9 cm^{-3} . The atoms are cooled on the $2^3S_1 \rightarrow 2^3P_2$ transition, which has a wavelength of 1083 nm.

A probe laser is scanned in frequency around the $2^2S_1 - 2^3P_2$ asymptote and the ion rate is measured as a function of the probe laser frequency. The produced ions are measured with micro-channel plates. The laser light is generated by diode lasers. The frequency of the probe laser light is calibrated using a Fabry-Perot interferometer for the relative frequency scale and the Lamb dip to determine the absolute frequency. The uncertainty in the absolute frequency scale is 20 MHz.

The trapping laser is periodically switched off, since we are only interested

in ionization induced by the probe laser. The laser is switched off for 25% of the period, by detuning its frequency 500 MHz to the red of the $2^3S_1 \rightarrow 2^3P_2$ transition. This is far enough to ensure that the trapping laser does not induce many ions. The period when the trapping laser is switched off is defined as the probing period, while the period when the trapping laser is switched on is defined as the trapping period. The probing period is $20 \mu\text{s}$, which is short enough to avoid significant expansion of the cloud of trapped atoms. The probe laser is switched off in the trapping period using an acousto-optical modulator, from which the first order diffraction beam is used as the probe laser. In this way we make sure that the cloud of trapped atoms is not perturbed by the probe laser. The ion signal is gated and can be measured both in the probing period and in the trapping period. In the probing period the detuning-dependent ion rate is measured, while the signal in the trapping period is used to monitor the stability of the trapped cloud. A typical scan time is 100 s. A typical measurement is shown in Fig. 6.2.

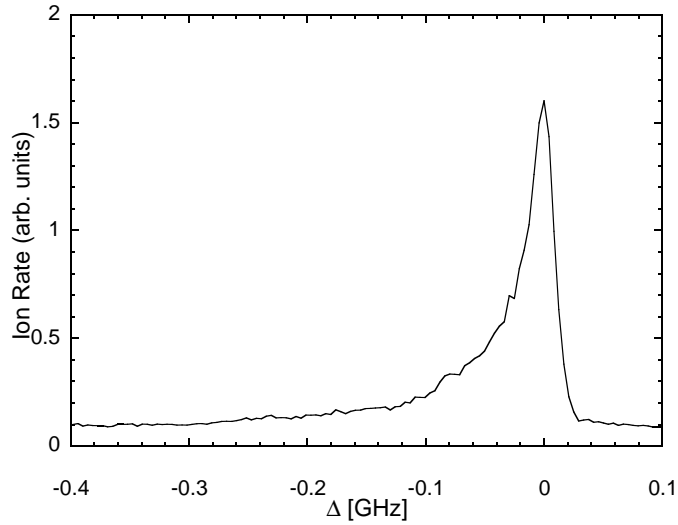


Figure 6.2 Ion rate as a function of the probe laser frequency. The probe laser frequency is expressed as the detuning Δ with respect to the $2^3S_1 - 2^3P_2$ asymptote. The saturation parameter of the probe laser was $s_0 = 450$.

6.3 The two state model

In Fig. 6.3 a schematic representation of the two-state system is shown. The laser light is detuned to the red of the $2^3S_1 - 2^3P_2$ asymptote with a detuning Δ . For a large detuning of $\Delta \gg \Gamma$, where Γ is the linewidth of the transition, the excitation can only take place around the Condon point R_c , where a transition can occur without appreciable change of the relative kinetic energy of the atoms.

We describe the system in terms of a dressed-state picture to obtain an insightful and quantitative description, where the ground and the excited state potential are coupled by the light field. The electronic coupling is given by the Rabi fre-

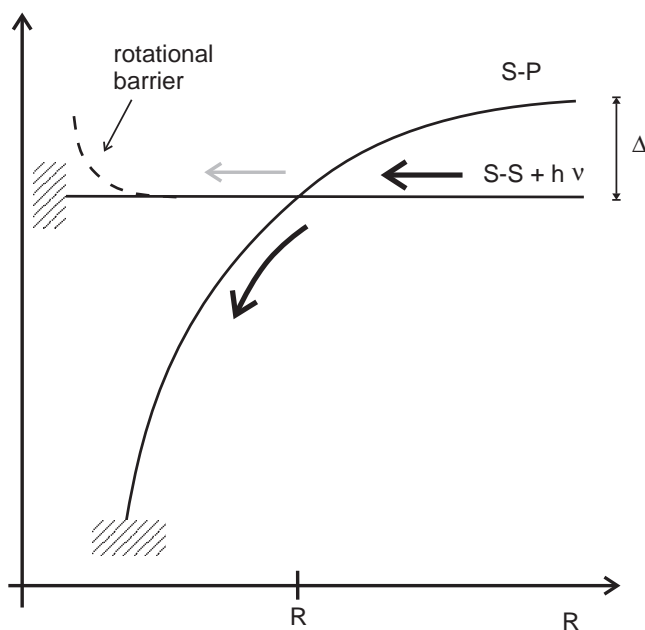


Figure 6.3 Schematic representation of the two-state system, where energy of the ground state S+S potential is shifted by the energy of a photon. The light is detuned with Δ to the red of the S+P asymptote. A transition can occur at the crossing at R_c and the grey arrow indicates the population that is not excited. The shaded regions indicate the regions where PI can take place. The potential barrier on the S+S potential (for $\ell \neq 0$) is shown with the dashed line.

quency Ω , which can be found from the atomic Rabi frequency $\Omega_{at}^2 = s_0/2\Gamma_{at}^2$, and is responsible for an avoided crossing of the adiabatic potentials, which can be seen in Fig. 6.4. The transition from the ground to the excited state is described in terms of the electronic coupling. Collisions in the ensemble of 2S atoms occur on the ground state potential, with velocities determined by the temperature of the MOT. After having passed the region around the Condon distance, a system can be either on the lower adiabatic potential, or on the upper adiabatic potential. Being on the lower one at $R < R_c$ means to be in the excited state. The probability for this is given by the Landau-Zener expression [9]:

$$P = 1 - \exp\left(-\frac{\pi \hbar \Omega^2}{2\alpha v_{rad}}\right), \quad (6.1)$$

where α is the gradient of the difference between the diabatic potentials at the crossing point R_c , and v_{rad} is the radial velocity. We have used the relation $|H_{12}|^2 = (\Omega/2)^2$ to express the electronic coupling in terms of the Rabi frequency. The detuning Δ is used to determine R_c via the relation $\Delta = C_3/R_c^3$. The Condon distances relevant for the present discussion are found to be in the order

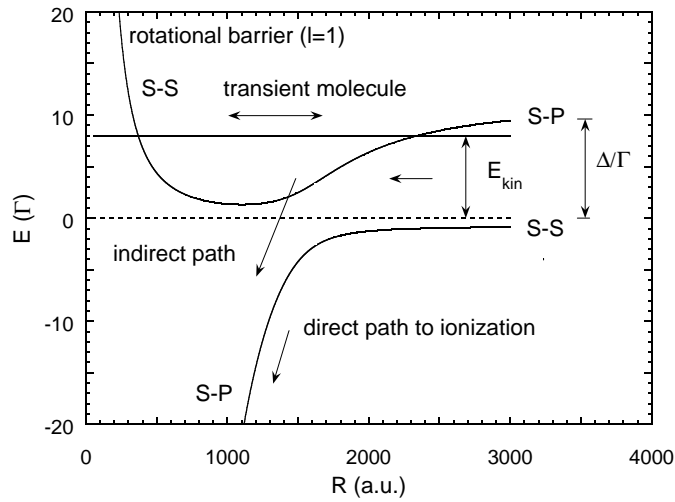


Figure 6.4 Molecular dressed state picture, where the adiabatic potentials are shown. The system can ionize directly or indirectly. For $\ell \neq 0$ the rotational barrier on the S-S potential prevents the transient molecule to reach small internuclear distances.

of 100 - 1000 atomic units. At these large distances α is given by $\alpha = 3C_3/R_c^4$ and the local Ω is approximately constant and can be calculated from Ω_{ut} .

We use Eq. 6.1 to formulate an expression for the ionization rate constant. The model assumes that close collisions lead to PI with 100% probability, except if this is forbidden by the spin selection rule. This is a valid assumption, which has been verified even for thermal collisions [12]. The expression is given in terms of the partial wave expansion of an inelastic scattering cross section described by Q , which is the angular momentum dependent ionization probability. The ionization rate constant K depends on the detuning Δ , the laser intensity s_0 , and the velocity v , and is written as [8]

$$K(\Delta, s_0, v) = \frac{\pi \hbar^2 v}{\mu^2} \sum_{\ell=0}^{\ell_{max}} (2\ell + 1) \Theta_{\ell} O_{\ell}, \quad (6.2)$$

where μ is the reduced mass, and Θ_{ℓ} is a step function. The step function Θ_{ℓ} is introduced, because the collision system has a well defined *gerade* (g) or *ungerade* (u) symmetry, which restricts the allowed partial waves. Since the collision system is symmetric the weight of the allowed partial waves is doubled. Thus:

	even ℓ	odd ℓ
<i>gerade</i> ground state:	$\Theta_{\ell} = 2$	$\Theta_{\ell} = 0$
<i>ungerade</i> ground state:	$\Theta_{\ell} = 0$	$\Theta_{\ell} = 2$

The summation in Eq. 6.2 has to be carried out until a certain maximum angular momentum ℓ_{max} . The maximum angular momentum is limited by the rotational barrier in the ground state and the kinetic energy of the collision system. The system needs to reach the Condon point R_c in order to make the transition, reach small internuclear distances on the excited state potential, and contribute to the ionization. Hence ℓ_{max} is determined by the relation:

$$\frac{\hbar^2}{2\mu} \frac{\ell_{max}(\ell_{max} + 1)}{R_c^2} - \frac{C_6}{R_c^6} > \frac{1}{2} \mu v^2. \quad (6.3)$$

In order to find an expression for O_{ℓ} , we have to distinguish the different possible paths leading to ionization. Below we make a distinction between direct and indirect paths of ionization, either in the excited state (SP) or in the ground state (SS):

- The direct SP contribution is possible for all allowed values of ℓ . The system is excited on the way in at the avoided crossing, then approaches small

distances on the excited state potential without decaying spontaneously by photon emission and Penning ionizes on the excited state potential. The corresponding probability is given by $P_\ell S_\ell$, where P_ℓ is defined in Eq. 6.1 and $S_\ell = \exp(-\Gamma t_\ell)$ is the survival probability in the excited state during the approach time t_ℓ . This time is obtained from integration along the ℓ -dependent trajectory, using $t_\ell = \int dR/v_\ell(R)$, with $v_\ell(R)$ the ℓ -dependent radial velocity on the excited state potential curve.

- The indirect SP contribution has not been considered in earlier models [2, 10]. In this case the system is not excited on the way in. If $\ell \neq 0$ and $E_{kin} < \Delta$, the system is partly captured and forms a transient molecule in the upper adiabatic potential (see Fig. 6.4). This molecule can either dissociate by diabatic crossing on the way out, or ionize after a diabatic crossing on the way in. While a correct calculation should use amplitudes and phases to calculate this contribution, we content ourselves here with a calculation using probabilities. The total contribution can then be calculated by summation of the successive contributions, *i.e.*, the contributions after 1,2,3, .. oscillations. The infinite sum can be carried out and leads to the ionization probability $P_\ell S_\ell(1 - P_\ell)/(1 + P_\ell)$.
- For the direct SS contribution the system is not excited on the way in at the avoided crossing, then approaches small distances on the ground state potential and Penning ionizes on the ground state potential. The corresponding probability is $(1 - P_\ell)$. As is shown in Sec. 3.6, at the low collision energies in the MOT only partial waves with $\ell = 0$ can penetrate the rotational barrier on the ground state and reach the small internuclear distances, where PI occurs, *i.e.* only $\ell = 0$ contributes to the ionization.
- For the indirect SS contribution the system is excited on the way in, then spontaneously decays to the ground state, and Penning ionizes in the ground state, which is only possible for $\ell = 0$. The corresponding probability is $P_\ell(1 - S_\ell)$.

The ionization probability to be used in Eq. 6.2 thus becomes the sum of those four terms:

$$\begin{aligned} O_\ell &= P_\ell S_\ell + P_\ell S_\ell(1 - P_\ell)/(1 + P_\ell) = 2P_\ell S_\ell/(1 + P_\ell) & \text{for } \ell \neq 0 \\ O_\ell &= P_\ell S_\ell + (1 - P_\ell) + P_\ell(1 - S_\ell) = 1 & \text{for } \ell = 0. \end{aligned} \tag{6.4}$$

In a numerical program, the evaluation of expression Eq. 6.4 for the ionization

rate constant is easily carried out. In Fig. 6.5 the total calculated ionization rate constant and the direct and indirect contributions to it are shown. It can be seen that the direct SP contribution is the dominant contribution. The crucial quantity that determines the quality of the result is the excitation probability function, which is approximated using the Landau-Zener formula in Eq. 6.1. While this approximation is expected to be valid for large detunings ($\Delta \gg \Gamma$), when the region of distances where transitions induced by the radiation occur is rather narrow [11], its validity for small detunings is questionable. To check whether the approximation is good enough, we have calculated the excitation probability with a quantum-mechanical model and find the agreement with the semi-classical Landau-Zener excitation probability to be good.

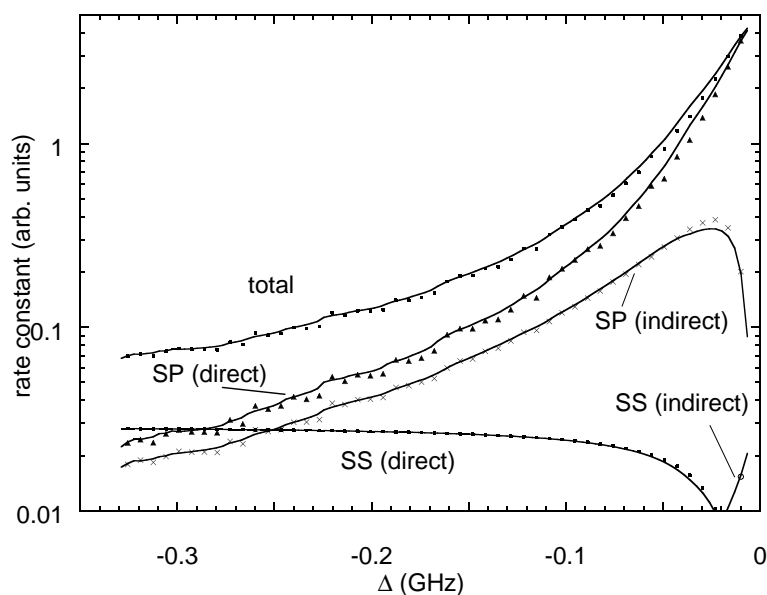


Figure 6.5 Calculated ionization rate constant as a function of Δ . The direct and the indirect contributions, as discussed in the text, are shown. The symbols represent the calculation. A smoothed line is drawn to correct for structure that arises, due to the finite steps in the velocity distribution that have been used in the calculation.

6.4 Calculation of the absolute ionization rate constant

In this section we describe the procedure we followed to calculate the absolute ionization rate constant for the $2^3S_1 - 2^3P_2$ system, using the semi-classical two-state model described above.

We have used the actual potential curves connected to the $2^3S_1 - 2^3P_2$ asymptote, which were discussed in Chap 3. We only consider the attractive potentials, since they can be populated at negative detunings from the atomic resonance. We have found nine such potentials, which all behave as C_3/R^3 at the large distances that are relevant for the calculation of the ionization rate constant. For all potentials we have calculated the C_3 coefficients, the linewidths for spontaneous emission Γ , and the Penning ionization probability p . The PI probability is deduced from the spin character of the state at large internuclear distances, where the spin states are mixed. We have assumed that at short range, where S is a good quantum number, the singlet and triplet spin states ionize with unity probability and the quintet states ionize with zero probability. A list of the properties of the potentials connected to the $2^3S_1 - 2^3P_2$ asymptote is given in Tab. 6.1.

The excited state potentials can be populated from various potentials connected to the $2^3S_1 - 2^3S_1$ potentials. These potentials are degenerate at the distances where the excitations are made, but we characterize them by the total spin quantum number and its projection on the internuclear axis. Since the potentials are degenerate we can choose any axis. We found that when the system is excited to the $2^3S_1 - 2^3P_2$ system, every ground state potential is mainly coupled to one excited state potential and that the coupling to other excited states is an order of magnitude weaker. In principle, allowed contributions from all ground to all excited states should be taken into account, but we have used an approximation where only the dominant contribution has been included in the calculation. We find that all dominant transitions are π transitions. For the excited states the spin states are mixed and the Hund's case (a) ground states couple only with a fraction of the excited Hund's case (c) states. This fraction is given by w , where w is the population probability of the fraction of the excited state coupling with the ground state. We use w to obtain the Rabi frequency for each ground to excited state transition, since we need the Rabi frequency to evaluate the Landau-Zener expression. The characteristic Rabi frequency Ω_{mol} for each pair is given by $\Omega_{mol} = (\Omega_{at} / \Gamma_{at}) \Gamma_{mol} \sqrt{w}$.

We use the nine values of Ω_{mol} to calculate the total ionization rate constant. The rate constant for each of the nine contributions is calculated using the two-state model. The total ionization rate constant is obtained by summing over the

Table 6.1 Properties of the excited state potentials connected to the $2^3S_1 - 2^3P_1$ asymptote. The C_3 coefficient is expressed in terms of the dispersion coefficient μ , as discussed in Sec. 3.4. The excited fraction is the fraction of the state that can be excited from the ground state. The polarization is the polarization of the light required to make the excitation. The ground state potentials where they are excited from are also shown.

Ground state		Excited state					
Symm.	Σ	Symm.	Γ	C_3	w	p	pol.
			(Γ_{at})	(μ)			
$1^1\Sigma_g^+$	0	0_u^+	1.271	-0.536	0.509	0.89	π
$5^1\Sigma_g^+$	-2	2_u	1.016	-0.455	0.394	0.59	π
$5^1\Sigma_g^+$	-1	1_u	1.582	-0.313	0.522	0.27	π
$5^1\Sigma_g^+$	0	0_u^+	1.984	-0.242	0.505	0.08	π
$5^1\Sigma_g^+$	1	1_u	1.582	-0.313	0.522	0.275	π
$5^1\Sigma_g^+$	2	2_u	1.016	-0.455	0.394	0.59	π
$3^1\Sigma_u^+$	-1	1_g	1.217	-0.516	0.557	0.86	π
$3^1\Sigma_u^+$	0	0_g^-	1.538	-0.333	0.500	0.75	π
$3^1\Sigma_u^+$	1	1_g	1.217	-0.516	0.557	0.86	π

nine contributions and weighing each contribution with a statistical factor of 1/9, where each rate constant is multiplied by its own Penning ionization probability p .

The result of such a calculation, averaged over the thermal velocity distribution, corresponding to a temperature of 1 mK, is shown in Fig. 6.6. In the calculation we take into account that only a third of the light has the π -polarization required to make the transitions shown in Tab. 6.1. Since for the measured curve neither a reliable absolute calibration was possible, nor a reliable determination of the background, we adapted the measured curve to the calculated one by choosing the background and the normalization to obtain best agreement. Therefore the comparison between the measurement and the calculation yields only information on the accuracy of the predicted shape of the curve. In Fig. 6.6 we can see that the shape of the ionization rate constant is very accurately predicted by the calculation. The slightly higher values in certain detuning ranges can be attributed to the photoassociation resonances discussed in Chap. 4. The excitation of these bound states is not included in the semi-classical two-state model, so we expect to see these deviations. Therefore we can state that there is agreement within experi-

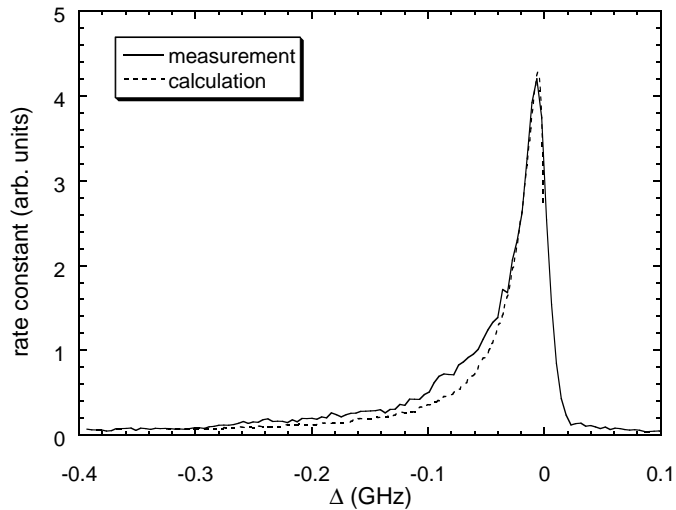


Figure 6.6 The scaled measured ionization curve and the calculated ionization curve as a function of the detuning of the probe laser. The ion rate constant is expressed in arbitrary units.

mental error. This is a remarkable result considering the complexity of the system and the simplification that we made.

6.5 Comparison of calculated and measured absolute ionization rate constants

Since the agreement of the calculated behavior of the ionization rate constant with the measured behavior is so good, we are confident that the calculated absolute ionization rate constant should also be reasonably accurate. This is especially interesting, because existing experimentally determined absolute ionization rates are uncertain by factors of 2 to 100 [2–6]. In this section we will compare our calculated absolute ionization rate constant with the experimental ionization rate constants. All of these values have been determined at the detuning where the ionization rate constant is maximal, but under different experimental circumstances. Especially, different laser intensities have been used and slightly different MOT conditions and correspondingly slightly different temperatures. Our model allows

us to judge the possible influence of these different conditions. As an example, we show the ionization rate constant in Fig. 6.7 calculated at a temperature of 1 mK for different saturation parameters, namely $s_0 = 50$ and $s_0 = 200$. We notice that the maximum value of the ionization rate constant, K_{max}^{ion} , is rather insensitive to the varied parameter. Since the uncertainties of the available experimental values are much larger than the variation of the calculated maximum rate constant for different experimental conditions, it is not necessary to account for these differences. It is sufficient to compare the calculated K_{max}^{ion} with the maximum values reported in the literature.

To be able to compare the measured and calculated rate constants, we must take care to use identical definitions for the rate constant. Therefore it is necessary to briefly outline the procedures that have been applied to obtain experimental ionization rate constants for optical collisions. In most experiments the ionization rate constant K^{ion} or the collision rate constant K was obtained from a measurement of the decay rate β of the MOT, when stopping the loading of the MOT. Note, that the collision rate constant K is a measure for all collisions resulting in trap loss, while the ionization rate constant K^{ion} only takes into account the colli-

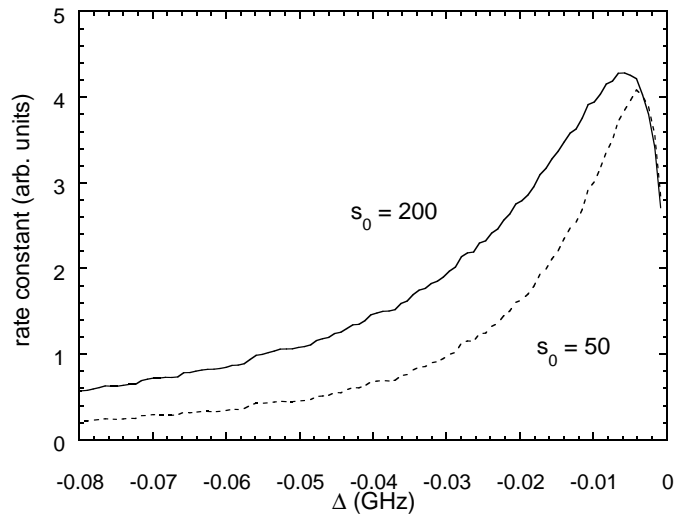


Figure 6.7 Ionization rate constant calculated for $s_0 = 50$ (dashed line) and $s_0 = 200$ (solid line).

sions where an ion is formed. The ion rate or fluorescence rate is used to monitor the decrease of the density n . The valid assumption is made, that the decay is mainly due to collisions between trapped atoms. Hence a loss rate constant β is defined by $dn/dt = -\beta n^2$, where $\beta = 2K$. The factor 2 stems from the fact, that in one trap loss collision two atoms escape from the trap. We use the same definition in the semi-classical two-state model, *i.e.* $dn_{ion}/dt = Kn^2$, where n_{ion} is the ion density.

In order to experimentally determine the value of K , one needs to know n on an absolute scale. This poses severe problems and is the reason for the rather large uncertainties of the experimentally determined rate constants. Furthermore, some confusion has arisen because the experimentally determined rate constants have not been defined in the consistent way described above. Instead, one has argued that the ionization rate constant should be defined as the rate constant for ionization in collisions of excited 2^3P_2 atoms with ground state 2^3S_1 atoms. Hence the decay is given by $dn_{ion}/dt = 2K'n_p n_s = 2K'\pi_p(1 - \pi_p)n^2$, where π_p is the population of the excited state [3]. The factor of 2 comes from the fact that we cannot distinguish between a collision of a S with a P atom and a P with a S atom. The rate constant at the detuning where the ion rate constant is maximal, K'_{max} is then found by assuming that the ensemble is saturated, *i.e.* that $\pi_p = 1/2$. For a given measured ion rate constant this leads to the relation $K'_{max} = 2K_{max}$, where K_{max} is our maximum rate constant.

This definition of K'_{max} is unphysical, which can be seen as follows. The rate constant is the product of the collision velocity and the cross section for ionization. This cross section is limited by the number of partial waves that can contribute. For $\Delta \gg \Gamma$, π_p goes to zero, while K still has a value of the order of K_{max} , as can be seen in Fig. 6.6. In that case the definition $dn_{ion}/dt = 2K'\pi_p(1 - \pi_p)n^2$ would lead to unphysically large values of K' , which would require ionization cross sections exceeding the maximum cross section, given the total number of partial waves. In Tab. 6.2 an overview is given of the measured values of β and K'_{max} , that are found in the literature. These values have been corrected to agree with our definition of K_{max} as defined above. In some of the experiments the collision rate constant K_{max} is determined and in other experiments the ionization rate constant K'_{max} is determined. Since we cannot estimate for each experiment the fraction of collisions that do lead to losses from the trap, but do not lead to ionization, we cannot compare every value with the calculation.

We notice that the experimentally determined ionization rate constant of Kumakura *et al.* [5] agrees within given limits of error with the value predicted by

our calculation. However, the value of Mastwijk *et al.* [2] does not agree with the calculated ionization rate, which is due to an error made in determining the transmission through the mass spectrometer used to measure the ion rate. It is difficult to estimate the accuracy of the calculated value, as a result of the approximations that have been made. However, the K_{max}^{ion} is virtually independent of the experimental conditions used in the experiment. We therefore estimate that if our assumptions are correct, the calculated cross section is accurate to within 20%. We cannot calculate the collision loss rate K_{max} from K_{max}^{ion} , but it is clear that the K_{max}^{ion} should be a fraction of K_{max} .

Table 6.2 Comparison of experimental values of K_{max} and K_{max}^{ion} with the theoretical value predicted by our two-state model and with each other. The corrected values are based on the definitions given in the text.

Reference	Published β_{max} (cm ³ /s)	Corrected K_{max} (cm ³ /s)	Published K_{max}^{ion} (cm ³ /s)	Corrected K_{max}^{ion} (cm ³ /s)
Bardou <i>et al.</i> [3]	7×10^{-8} uncertainty: factor 4	3.4×10^{-8}	-	-
Tol <i>et al.</i> [4]	$(1.3 \pm 0.3) \times 10^{-8}$	$(6.5 \pm 0.3) \times 10^{-9}$	-	-
Browaeyns <i>et al.</i> [6]	3×10^{-8} uncertainty: factor 2	1.5×10^{-8}	-	-
Kumakura <i>et al.</i> [5]	-	-	$(8.3 \pm 2.5) \times 10^{-8}$	$(2.1 \pm 0.6) \times 10^{-8}$
Mastwijk <i>et al.</i> [2]	-	-	$(1.9 \pm 0.8) \times 10^{-9}$	$(1.3 \pm 0.6) \times 10^{-9}$
This work	-	-	-	2.5×10^{-8}

6.6 Conclusion

We have developed a semi-classical model to describe Penning ionization in optical collisions. The model is a two-state model, using a partial wave expansion and the Landau-Zener approximation to calculate the excitation rate. The predicted ionization rate constant as a function of the detuning of the light agrees well with measurements that we have done. Furthermore we have calculated the absolute ionization rate constant and compared it with measured absolute rate coefficients that have appeared in the literature. We have calculated an absolute ionization rate constant $K_{max} = 2.5 \times 10^{-8} \text{ cm}^3/\text{s}$. If we use a consistent definition of K_{max} we find good agreement with most quoted experimentally determined values.

References

- [1] H.J. Metcalf and P. van der Straten, *Laser Cooling and Trapping*, Springer-Verlag, New York (1999).
- [2] H. C. Mastwijk, J. W. Thomsen, P. van der Straten, and A. Niehaus, *Phys. Rev. Lett.* **80**, 5516 (1998).
- [3] F. Bardou, O. Emile, J.-M. Courty, C.I. Westbrook, A. Aspect, *Europhys. Lett.* **20**, 681 (1992).
- [4] P. J. J. Tol, N. Herschbach, E. A. Hessels, W. Hogervorst, and W. Vassen, *Phys. Rev. A* **60**, R761 (1999).
- [5] M. Kumakura, and N. Morita, *Phys. Rev. Lett.* **82**, 2848 (1999).
- [6] A. Browaeys, J. Poupard, A. Robert, S. Nowak, W. Rooijackers, E. Arimondo, L. Marcassa, D. Boiron, C. Westbrook, and A. Aspect, *Eur.Phys.J.D* **8**, 199 (2000).
- [7] A. Gallagher and D.E. Pritchard, *Phys. Rev. Lett.* **63**, 957 (1989)
- [8] P.S. Julienne and J. Vigué, *Phys. Rev. A* **44**, 4464 (1991).
- [9] K.-A. Suominen, *J. Phys. B* **29**, 5981 (1996)
- [10] G. Woestenenk, H.C. Mastwijk, J.W. Thomsen, P. van der Straten, M. Pieksma, M. van Rijnbach, and A. Niehaus, *Nucl. Instr. Meth. B* **154**, 194 (1999).
- [11] P.S. Julienne, A.M. Smith, and K. Burnett, *Adv. At. Mol. Opt. Phys.* **30**, 141 (1992).
- [12] M. Müller, A. Merz, M.W. Ruf, H. Hotop, W. Meyer, and M. Movre, *Z. Phys. D* **21**, 89 (1991)

Samenvatting

De experimenten die in dit proefschrift besproken worden, zijn uitgevoerd met ultra-koude atomen. In de jaren '80 is een methode ontwikkeld om atomen af te koelen tot ultra-lage temperaturen. Deze methode wordt laserkoeling genoemd. Met deze koude atomen kunnen allerlei experimenten worden gedaan, die niet mogelijk zijn met thermische atomen. Voordat daar op ingegaan wordt, zal kort besproken worden wat laserkoeling is.

Met behulp van laserlicht kan een atoom aangeslagen worden naar een hogere energietoestand, een aangeslagen toestand, als het laserlicht de energie heeft die overeen komt met de energie die nodig is om het atoom in die aangeslagen toestand te brengen. Met het aanslaan van het atoom wordt er impuls overgedragen op het atoom door het foton, dat afkomstig is uit de laserbundel, in de richting waar het licht vandaan komt. Omdat de aangeslagen toestand geen stabiele toestand is, valt het atoom na een korte tijd terug naar zijn oorspronkelijke toestand. Het moet de overtollige energie kwijt en zendt daarom een foton uit, in een willekeurige richting. Met het uitzenden van het foton ervaart het atoom een terugslag van het foton. De snelheidsverandering van het atoom per geabsorbeerd foton is klein, maar als een atoom vaak genoeg door een laser aangeslagen wordt en vervolgens vervalt, kan een grote snelheidsverandering bereikt worden. Omdat het atoom als het terugvalt een kracht in een willekeurige richting ervaart, is de netto kracht als gevolg van de terugslag na een groot aantal keer terugvallen gelijk aan nul. Op deze manier wordt er een kracht op het atoom in een wel bepaalde richting uitgeoefend, namelijk in de richting van het laserlicht, en kan de snelheid van het atoom in deze richting verkleind worden.

Om de snelheid van de atomen in drie dimensies af te remmen gebruiken we laserlicht uit zes richtingen, namelijk twee tegenovergesteld gerichte bundels per richting. We bestuderen interacties tussen de koude atomen en daarom is het belangrijk om de atomen zo dicht mogelijk bij elkaar te houden. Daarvoor is alleen laserlicht niet voldoende, maar moeten we ook een speciaal magneetveld

gebruiken. De combinatie van het laserlicht en dit magneetveld (dit heet een magneto-optische val) remt de atomen af en vangt ze in het midden van de opstelling. In het experiment gebruiken we helium atomen, die we koelen tot een temperatuur van ongeveer 1 mK, dat is $\frac{1}{1000}$ graad boven het absolute nulpunt. We vangen ongeveer 1 miljoen atomen in onze magneto-optische val met een dichtheid van 1 miljard atomen/cm³. Deze dichtheid is groot genoeg om interacties tussen koude gevangen atomen te bestuderen. In hoofdstuk 2 worden de principes van laserkoeling kort besproken. Verder wordt in dit hoofdstuk de experimentele opstelling beschreven, waarmee de experimenten die besproken worden in dit proefschrift gedaan zijn. Ook wordt er uitgelegd hoe de eigenschappen van het wolkje koude atomen, gevangen in de magneto-optische val, bepaald zijn.

Het atoom dat in dit proefschrift bestudeerd wordt is metastabiel helium. Het helium atoom bestaat uit een kern en twee elektronen. Metastabiel helium (He*) bevindt zich in een aangeslagen toestand, waarbij één van de elektronen is aangeslagen naar een hogere energietoestand. Het woord metastabiel geeft aan dat de levensduur van de aangeslagen toestand heel lang is. De levensduur van He* is ongeveer twee uur, wat oneindig is op de tijdschaal die relevant is voor onze experimenten. Doordat het atoom in de metastabiele toestand is, is de interne energie van het atoom heel groot. Als twee atomen dicht bij elkaar komen (in de orde van een paar tiende nm, waarbij een nm een miljoenste mm is), wordt de metastabiele toestand instabiel en wordt er een ion gevormd.

Met behulp van koude atomen kunnen hoge precisie experimenten worden uitgevoerd, omdat hun kinetische energie zo laag is. Een veelgebruikte methode om interacties tussen koude atomen te bestuderen is foto-associatie spectroscopie. Deze methode is ook in dit proefschrift toegepast. Tot nu toe zijn vooral de alkali-metaal atomen met foto-associatie spectroscopie bestudeerd. Wij hebben foto-associatie gebruikt om He* atomen te bestuderen.

In een foto-associatie experiment worden twee botsende atomen aangeslagen naar een geëxciteerde toestand met behulp van laserlicht. In deze geëxciteerde toestand is de aantrekkingskracht tussen de atomen al op grote afstanden (~ 100 nm) groot genoeg om een molecuul te vormen. In zo'n molecuul kunnen de atomen alleen in discrete vibratiemodes ten opzichte van elkaar bewegen, die elk een eigen energieniveau hebben. Het molecuul kan ook alleen in deze vibratiemodes worden aangeslagen. Daarom kan er alleen met de laser een overgang gemaakt worden naar een vibrationele toestand in een molecuul, als het licht precies de energie heeft die overeenkomt met het energieniveau van die vibratiemode.

De moleculen die gevormd worden met foto-associatie zijn heel bijzonder.

De atomen in deze moleculen bevinden zich het grootste gedeelte van de tijd op grote afstanden van elkaar, die in de orde liggen van ongeveer 100 nm. Normaal is de gemiddelde afstand tussen de atomen in een molecuul ongeveer 0.1 nm. Doordat de afstand tussen de atomen zo groot is, levert foto-associatie ook informatie over atomaire eigenschappen op. De alkali-metaal atomen zijn uitgebreid bestudeerd met foto-associatie spectroscopie, met veel resultaat. De methode was daarentegen nog niet toegepast op de metastabiele edelgas atomen. Over koude He* atomen is weinig bekend. In dit proefschrift worden de eerste resultaten van foto-associatie spectroscopie voor He* besproken. Er wordt een eerste verkenning gemaakt van interessante processen die een rol spelen voor He*.

Om de experimentele resultaten te kunnen analyseren is het belangrijk om de interacties in het molecuul te kennen. We hebben deze interacties berekend. De berekeningen worden besproken in hoofdstuk 3. Aangezien de gemiddelde afstand tussen de atoomkernen in het molecuul zo groot is, zijn de parameters die gebruikt worden in de berekeningen atomaire eigenschappen.

In hoofdstuk 4 worden foto-associatie experimenten besproken. In het experiment worden ionen gemeten, terwijl de golflengte van de foto-associatie-laser gevarieerd wordt. Als de golflengte overeen komt met het energieniveau van een gebonden toestand, wordt een verhoging van het aantal ionen gemeten en op die manier wordt de energie van de gebonden toestanden gemeten. De energie van de toestanden wordt bepaald door de interacties in het molecuul. De berekeningen uit hoofdstuk 3 zijn gebruikt om de energieniveaus van de toestanden te berekenen. Vervolgens zijn de berekende energieniveaus vergeleken met de gemeten energieniveaus.

In hoofdstuk 5 meten we een aantal bijzondere effecten, waarvoor we een kwalitatieve verklaring hebben gevonden. Eén van die effecten is, dat we een vermindering van het ionensignaal waarnemen, als er een gebonden toestand wordt aangeslagen. In dat geval wordt er waarschijnlijk een vibratiemode in een “puur lange-drachts” molecuul aangeslagen. In zo’n molecuul kunnen de atoomkernen niet dicht bij elkaar komen. De kleinste afstand die ze bereiken is ongeveer 50 nm. Dat betekent dat ze niet dicht genoeg bij elkaar kunnen komen om te ioniseren en dat is de reden waarom ze waargenomen worden als een afname van het ionensignaal.

In hoofdstuk 6 tenslotte wordt het dynamische gedrag van de botsende atomen bestudeerd. Ook in dit geval worden de atomen aangeslagen met laserlicht. In de aangeslagen toestand maken de botsende atomen meer kans om het gebied te bereiken waar ionisatie plaatsvindt. We hebben een model opgesteld om de

ionisatie-waarschijnlijkheid te berekenen als functie van de kleur van het licht. De uitkomsten van dit model worden vergeleken met gemeten waarden.

Samenvattend bestuderen we koude botsende He* atomen onder invloed van licht. Daarbij worden verschillende processen bekeken, variërend van het aanslaan van moleculaire toestanden tot het dynamische gedrag van botsende atomen. Alle experimenten en bijbehorende analyses beschreven in dit proefschrift leveren informatie op over de interacties tussen de koude He* atomen.

Curriculum Vitae

Naam	Geraldine Woestenenk
Geboren	13 juli 1973 te Amsterdam
Onderwijs	1985-1991 VWO, Stedelijk Gymnasium Apeldoorn
Studie	1991-1996 Experimentele Natuurkunde, RU Groningen Afstudeeronderzoek: "Single electron capture in $N^{4+} + H$ collisions" o.l.v. Drs. F.W. Blik en Prof. Dr. R. Morgenstern.
Promotieonderzoek	1996-2001 Atoomfysica, Debye Insituut, Universiteit Utrecht Proefschrift : " Photoassociation of Cold Metastable Helium Atoms" o.l.v. Prof. Dr. P. van der Straten en Prof. Dr. A. Hiehaus.
Conferenties	Human Capital and Mobility Workshop: "Lasers, Atoms and Molecules: Dynamical Interactions" Vulcano, Italie, 21-27 september 1996 Euroconference on Slow Collisions between Laser Manipulated Systems (ESCOLAR) '98 Rust, Oostenrijk, 1-5 april 1998

Workshop “ Cold Atomic Collisions:
Formation of Cold Molecules”
Les Houches, Frankrijk, 1-5 maart 1999

Euroconference on Slow Collisions between
Laser Manipulated Systems (ESCOLAR) ‘99
Elounda Bay, Kreta, Griekenland, 1-4 mei 1999

Workshop “ Prospects of Cold Molecules”
Heidelberg, Duitsland, 8 - 10 november 1999

Zomerschool

Zomerschool “Trends in Molecular Physics”
Ecole de Physique
Les Houches, Frankrijk, 21-27 juni 1997

Publications

- *Collisions between ultracold metastable He atoms*
G. Woestenenk, H.C. Mastwijk, J.W. Thomsen, P. van der Straten,
M. Pieksma, M. van Rijnbach, and A. Niehaus,
Nucl. Instr. and Meth. in Phys. B **154** 194, (1999)
- *Photoassociation Spectroscopy of Cold He (2^3S) Atoms*
N. Herschbach, P.J.J. Tol, W. Vassen, and W. Hogervorst,
G. Woestenenk, J.W. Thomsen, P. van der Straten, and A. Niehaus,
Phys. Rev. Lett. **84**, 1874 (2000)
- *Construction of an Intense Low Velocity Metastable Helium Atomic Beam*
G. R. Woestenenk, J.W. Thomsen, M. van Rijnbach,
P. van der Straten, and A. Niehaus,
Submitted to Rev. Sci. Instrum.
(similar to Sec. 2.4)
- *Penning Ionization in Optical Collisions*
in preparation
(similar to Chap. 6)

Dankwoord

Tijdens de afgelopen jaren heb ik me regelmatig verheugd op het moment waarop ik mijn dankwoord zou schrijven. Het zou namelijk een misverstand zijn om te denken dat dit proefschrift het resultaat is van het werk van één persoon. Op deze plek wil ik dan ook graag een aantal mensen bedanken, die me in de afgelopen periode op verschillende manieren hebben bijgestaan.

Allereerst wil ik mijn promotoren bedanken, Peter van der Straten en Arend Niehaus. Ik heb veel van jullie grote kennis op het gebied van atoomfysica geleerd. Peter, dank je voor je stimulerende begeleiding. Zowel je enthousiasme als er resultaten waren, als je optimisme en steun in moeilijker tijden heb ik altijd erg gewaardeerd. Je deur stond altijd open en zelfs als je het heel druk had, maakte je tijd om met me mee te denken. Arend, bedankt voor je enthousiaste inbreng bij de interpretatie van de resultaten. Ik ben blij dat ik van je kennis en ervaring heb mogen profiteren.

Ik had het geluk om in een voortvarend team terecht te komen toen ik begon aan mijn onderzoek en ik heb me altijd prettig gevoeld tussen de “heliummannen”. In de eerste week dat ik in de groep was, werd er gevierd dat het gelukt was om een MOT te maken. Toen kon ik nog niet goed overzien wat voor een prestatie dat was. Inmiddels weet ik hoe moeilijk het was om die opstelling te bouwen en ik wil Hennie Mastwijk dan ook bedanken voor de mooie “erfenis” die hij heeft achtergelaten. Marc Pieksma wil ik bedanken voor de fijne samenwerking. Het was altijd erg gezellig om samen met jou ergens aan te werken. I learnt a lot from Jan Thomsen. Thank you very much for that. You taught me all the ins and outs of the setup and I enjoyed working with you. You always knew how to make everyone as excited about the research as you were yourself. I am only disappointed that I was not allowed to hear your jokes. Michiel van Rijnbach was een leuke kamergenoot, zowel in de experimenteerkamer als in de studeerkamer. Bedankt voor het kritisch lezen van een paar van mijn hoofdstukken en heel veel succes de komende tijd. Dries van Oosten heeft eerst als student onze

lasers gestabiliseerd en in de jaren daarna over van alles en nog wat mee gedacht. Edward Vliegen wil ik bedanken voor het werk dat hij als student gedaan heeft. Jammer dat we geen trap loss hebben gemeten, dat lag in elk geval niet aan de samenwerking.

Frits Ditewig en Hans Wisman wil ik bedanken voor hun hulp op elektronisch gebied. Gelukkig weten jullie een hele hoop meer van elektronica af dan ik en kon ik altijd bij jullie terecht. Voor de ondersteuning op het gebied van vacuüm was Jitse van der Weg er. Het was altijd een klein feestje om bij Gerard Höchner en Willem Tijben in de werkplaats langs te gaan. Zelfs als jullie zeiden dat het lang zou gaan duren, waren mijn klusjes razendsnel af. Ook Mari Hanegraaf van de IGF en Piet Engels, die de glas cellen heeft gemaakt, wil ik bedanken. De ochtend is niet mijn favoriete moment van de dag. Het was maar goed dat de dag begon met een vaatje helium halen bij Nico Kuipers en Jan van Eijk. Bedankt voor het grote aantal vaatjes dat jullie voor mij gevuld hebben. Met de collega-promovendi zijn er heel wat gezellige lunches, theepauzes, spelletjesavonden en conferenties geweest. Hennie Mastwijk, Bob van Someren, Arjen Amelink, Tycho Sonnemans, Wilco Planje, Michael Benndorf, Arnaud Kok, Tonnis Nuver, Michiel van Rijnbach, Dries van Oosten, Erik van Ooijen en Marijn van Veghel, bedankt voor de goede sfeer, het uitlenen van apparatuur en voor jullie belangstelling. Ik wil ook Herman Beijerinck, Pedro Zeijlmans van Emmichoven, Henrik Rudolph, Hanneke de Vries, Cees Andriessen en Henk Heideman bedanken voor hun interesse.

Het leven bestond gelukkig niet alleen maar uit onderzoek de afgelopen tijd. Met Monique, Stine, Quinten, Leo, Annegien en Margreet waren er veel leuke weekendjes en goede gesprekken. En dan waren er leuke avondjes en goede adviezen van Rosalind, gezelligheid en promotie-praat met Clara, goede buurvrouw Mariëlle, muziekadvies van Derk-Jan, ouderwets leuke tijd met Esther, Rosalie en Jetteke, veel plezier met de spray-blond, grappige verhalen van Clare, theateradvies van Ellen en lieve kaartjes van Graddie en Jan. Ik wil ook graag iedereen van “Totdat de Dom valt” bedanken voor de leuke maandagavonden, altijd een goed begin van de week.

Lieve papa en mama, bedankt voor jullie steun en liefde, mijn hele leven lang al. Lieve Doets, gelukkig heb ik jou als zusje is Zweden niet zo ver weg als het lijkt. En thuis was jij er, mijn lieve Marcel. Je bent mijn grote steun en toeverlaat geweest de afgelopen jaren. Dankjewel voor je liefde, je vermogen om me op te vrolijken als dat nodig was en alle grote en kleine dingen die je voor me gedaan hebt. Ik weet niet hoe ik het zonder jou had moeten doen en ik hoop dat dat ook nooit zal hoeven.